Spring 2015

Wireless tools for neuromodulation

Steven T Lee
Purdue University

Graduate School Form 30
Updated 1/15/2015

PURDUE UNIVERSITY
GRADUATE SCHOOL
Thesis/Dissertation Acceptance

This is to certify that the thesis/dissertation prepared

By Steven T. Lee

Entitled
WIRELESS TOOLS FOR NEUROMODULATION

For the degree of Doctor of Philosophy

Is approved by the final examining committee:

Pedro Irazoqui
Chair

Robert Worth

Young Kim

Amy Brewster

To the best of my knowledge and as understood by the student in the Thesis/Dissertation Agreement, Publication Delay, and Certification Disclaimer (Graduate School Form 32), this thesis/dissertation adheres to the provisions of Purdue University's "Policy of Integrity in Research" and the use of copyright material.

Approved by Major Professor(s): Pedro Irazoqui

Approved by: George R. Wodicka 4/22/2015

Head of the Departmental Graduate Program Date

WIRELESS TOOLS FOR NEUROMODULATION

A Dissertation

Submitted to the Faculty

of

Purdue University

by

Steven T Lee

In Partial Fulfillment of the

Requirements for the Degree

of

Doctor of Philosophy

May 2015

Purdue University

West Lafayette, Indiana

This dissertation is dedicated to my parents and brothers.

ACKNOWLEDGEMENTS

This dissertation is a reflection of the training and support from the incredible community of academics and friends that has surrounded me throughout graduate school. I am truly grateful to everyone who has influenced me. Several individuals deserve mentioning. My advisor, Professor Pedro Irazoqui, has always supported me personally and academically. The opportunities he continually created for me laid the foundations of my professional training. I thank him for all he has done. I would like to acknowledge my committee members, Dr. Robert Worth, Dr. Young Kim, and Dr. Amy Brewster for their support, and helpful discussions on neuroscience, epilepsy, optics, and other research topics. They have helped shape my perspective of the field. I would like to thank my collaborators at the Jackson Laboratory, Dr. Simon John, Dr. Da-Ting Lin, Dr. Pete Williams, and the entire John Lab. The optogenetic experiments were a success because of their contributions, and we experienced several incredible rock climbing sessions along the way. I would like to thank my collaborators at the University of Oxford, Professor John Jefferys and his student, Alex Lumsden. Professor Jefferys is a wealth of knowledge and taught me electrophysiology of the brain. While at Oxford, I also worked with Dr. Thelma Lovick at the University of Bristol to begin work in urinary incontinence. Dr. Lovick furthered my knowledge of physiology and ensured that my experiments were well thought out and prepared. During my time at Purdue, I have been lucky enough to be

surrounded by gifted, humble, fun and hardworking graduate students. I would like to thank the entire Center for Implantable Devices, and especially acknowledge those that I have had the privilege to work closely with: Dr. Matthew Ward, Dr. Shriram Raghunathan, Dr. Art Chlebowski, Becky Bercich, Henry Mei, Kurt Qing, Grant Wang, Arafat Muhammed, Jack Williams, and Dan Pederson. Additionally, I would like to acknowledge the lab staff, Gabriel Albors and Henry Zhang. They spent many hours fabricating devices and ensuring that I had the resources to run experiments. The IUSM-Purdue medical scientist training program (MSTP) deserves acknowledgement for their support and belief in me as a future physician-engineer/scientist. Finally, I would like to thank my Mom, Dad, and brothers, Lawrence and Anthony. All of them have always been there for me and tried to provide me with the best opportunities.

TABLE OF CONTENTS

Page

Page

LIST OF TABLES

LIST OF FIGURES

Figure Page

Figure Page

Figure Page

Figure Page

Figure Page

Figure Page

Figure Page

Figure Page

Figure Page

ABSTRACT

Lee, Steven T. Ph.D., Purdue University, May 2015. Wireless Tools for Neuromodulation. Major Professor: Pedro Irazoqui.

Epilepsy is a spectrum of diseases characterized by recurrent seizures. It is estimated that 50 million individuals worldwide are affected and 30% of cases are medically refractory or drug resistant. Vagus nerve stimulation (VNS) and deep brain stimulation (DBS) are the only FDA approved device based therapies. Neither therapy offers complete seizure freedom in a majority of users. Novel methodologies are needed to better understand mechanisms and chronic nature of epilepsy. Most tools for neuromodulation in rodents are tethered. The few wireless devices use batteries or are inductively powered. The tether restricts movement, limits behavioral tests, and increases the risk of infection. Batteries are large and heavy with a limited lifetime. Inductive powering suffers from rapid efficiency drops due to alignment mismatches and increased distances. Miniature wireless tools that offer behavioral freedom, data acquisition, and stimulation are needed.

This dissertation presents a platform of electrical, optical and radiofrequency (RF) technologies for device based neuromodulation. The platform can be configured with features including: two channels differential recording, one channel electrical stimulation, and one channel optical stimulation. Typical device operation consumes less than 4 mW. The analog front end has a bandwidth of 0.7 Hz – 1 kHz and a gain of 60 dB, and the

constant current driver provides biphasic electrical stimulation. For use with optogenetics, the deep brain optical stimulation module provides 27 mW/mm^2 of blue light (473 nm) with 21.01 mA. Pairing of stimulating and recording technologies allows closed-loop operation. A wireless powering cage is designed using the resonantly coupled filter energy transfer (RCFET) methodology. RF energy is coupled through magnetic resonance. The cage has a PTE ranging from 1.8-6.28% for a volume of 11 x 11 x 11 in^3. This is sufficient to chronically house subjects. The technologies are validated through various *in vivo* preparations. The tools are designed to study epilepsy, SUDEP, and urinary incontinence but can be configured for other studies. The broad application of these technologies can enable the scientific community to better study chronic diseases and closed-loop therapies.

CHAPTER 1. INTRODUCTION

The brain is exquisite, dynamic and complex. The hundreds of billions of neurons and glial cells coordinate and control our behavior. Since the classic experiments of Berger, Hodgkin and Huxley (1-5), and Benabid (6), the neuroscience research community has been in constant pursuit of better tools to study the spatial, temporal, electrical, and chemical attributes of normal and pathological neural systems. As a zealous proponent of systematic deconstruction of the central nervous system, Francis Crick wrote (7):

> A major first step, then, is to identify the many different types of neuron existing in the cerebral cortex and other parts of the brain. One of the next requirements (as discussed above) is to be able to turn the firing of one or more types of neuron on and off in the alert animal in a rapid manner. The ideal signal would be light, probably at an infrared wavelength to allow the light to penetrate far enough. This seems rather farfetched but it is conceivable that molecular biologists could engineer a particular cell type to be sensitive to light in this way.

In 2005, Boyden et al., followed with the first optogenetic demonstration of channelrhodopsin-2 (8). Since then, the neuroscience community has seen a tremendous push for integrated technologies that can match the physical properties of the brain, capture the resolution and scale of information being acquired and delivered, correlate multiple data streams to an event, and avoid the immune response. These technologies

can enable medical researchers to systematically deconstruct circuits and better understand the mechanism of neurological diseases. The end objective is to develop cost-effective, optimized, personalized treatments. Diseases such as epilepsy are complex, etiologically non-homogenous, and poorly understood. Epilepsy affects ~1% of the world's population (9). Approximately 20-30% of all cases are refractory to medication and the patients may be viable for surgical procedures including vagus nerve stimulation (VNS), deep brain stimulation (DBS), and focal brain resection. Temporal lobe epilepsy (TLE) is the largest category of intractable partial epilepsy with seizures predominantly initiating in the limbic circuitry. Owing to the success of DBS treatment in Parkinson's disease (10-12), DBS has been used in hopes of seizure freedom for severely epileptic patients (13). Two recent major clinical trials have investigated targeting DBS therapy at a clinically defined focus (14) or the anterior nucleus of the thalamus (ANT)—a site within the classical Papez circuit (15). A Cochrane meta-analysis showed that both strategies were effective at reducing seizure rates, but do not have significant responder rates (at least 50% seizure reduction) within 3 months of the trial (16). DBS may have longer working mechanisms and has great promise in neuromodulation. It is clear, though, that much progress is needed to reach seizure freedom for epileptic patients. Further, severe epileptic patients are at higher risk for sudden unexpected death in epilepsy (SUDEP). There are currently no effective treatments. Better tools are needed to enable the research community. This work presents a platform of wireless technologies for use in rodents to study epilepsy and SUDEP, but the platform can be extended to other disorders such as urinary incontinence. Sections 1.5-1.7 briefly overview aspects of epilepsy, SUDEP, and urinary incontinence. The devices presented in each of the

remaining chapters are standalone and can be integrated as a technology platform for chronic animal experiments. Chapter 2 focuses on an implantable closed loop device with biopotential acquisition and electrical stimulation. Chapter 3 presents published work on a miniature, deep brain optical stimulator for use in optogenetics, and Chapter 4 details a three-axis omnidirectional wireless powering system to house rodents.

1.1 Wireless Devices

Major goals in developing wireless neural prostheses involve moving towards more clinically relevant products, observing chronic behavior, and developing high throughput experimental protocols. A large portion of current rodent neural prostheses are based upon wired technologies which are disadvantageous due to the restrictive environment required by the tether, increased risk of infection from the percutaneous connector, and impractical implementation of large-group, longitudinal monitoring protocols. Wireless microsystems obviate the tethered disadvantages and transmit biopotentials with greater fidelity by measuring and processing the signal close to the source. Devices should contain circuitry for signal acquisition and conditioning, stimulation, telemetry, and power management. The ideal device would be miniscule, dissipate extremely low powers to prevent tissue heating, have noise floors below all signals of interest, and deliver any number of recording and stimulation channels with continuous operation. There are two primary modalities in neuromodulation: electrical stimulation and optical stimulation in optogenetics. Electrical stimulation methods are clinically approved and have been used for decades. It has consumer confidence and has been used in several clinical devices. Optogenetic modulation is a younger technology

that has seen tremendous growth in the last 10 years. Optogenetics allows cell type specific modulation of neurons through genetic techniques and spatial selectivity of tissue through optical delivery systems. This is a distinct advantage over electrical stimulation, which can only create transient electric fields in a given volume of tissue. Recording technologies have been extensively developed in both academia and industry and are more widely available to researchers. These devices are used to monitor the time varying electrical potentials in tissue. Tying the recording and stimulation technologies together to create closed-loop systems is required to further stimulation strategies. Optimized, controlled, smart personalized therapy is the next frontier in neuromodulation.

The probe tissue interface is the greatest challenge facing neuroprosthetics (17,18). High-density microelectrode arrays (MEA) provide high spatial resolution data revealing valuable insights into seizure (19-21). The most prominent probes currently used in research are microwire arrays, Michigan electrodes, and the Utah array. The chronic stability of these interfaces, though, is not robust and signals of interest degrade over time with large variation (22,23). The insertion of electrodes injures the brain, and a persistent, dynamic immune response results in poor electrode performance (23-26). Using MEA, it is currently difficult to achieve stable recordings of a specific neuron over a chronic time period (22,27). These conditions set serious limitations to experimental protocols. Current seizure detection algorithms use lower frequency content (< 100 Hz) that is chronically robust (28-31). Several strategies to stabilize microelectrode recordings are currently under investigation and include: insertion mechanisms for sub 25 micron diameter electrodes (32), conductive polymers with tissue friendly chemical and mechanical properties (33), coating flexible electrodes to be stiff during insertion and

flexible after (34), and coating electrodes with antiinflammatory nanoparticle agents (35). There is no clear solution and more studies are needed to overcome the probe-tissue interface. The current limitations should be carefully considered during design of experimental procedures and associated devices.

Heating of neurons have led to behavioral changes (36) and temperature rises in tissue can cause cell injury and death (37). Device heating is proportional to power dissipation, and the physical transfer of heat to tissue is dependent on the heat source location, heat sinks, and device-tissue interface. As en example, an LED used for optical stimulation in optogenetics typically generates a significant amount of heat, and the LED can be mounted on the skull (38-40) or implanted within the brain (41,42). Heating should be addressed in both methods; however, the latter strategy demands more stringent constraints and detailed analysis. The intent of this work is not to advance the understanding of the device-tissue interface, but careful consideration is given to design and methods that allow observation of chronic biopotentials and minimize tissue damage.

1.2 Electrical Closed-Loop Deep Brain Stimulation Technologies

Wireless biopotential acquisition requires amplification, signal conditioning, digitization, and telemetry. In epilepsy and SUDEP, the critical signals of interest are seizures, the electrocardiogram (ECG), and respiration biomarkers. Acquisition units are capturing the time and frequency content of the signals for analysis (43-45). Electroencephalogram is the clinical gold standard. EEG is recorded on the scalp, and the signal is a summation of all extracellular current sinks and sources under the site of interest (46). A disadvantage of scalp EEG, though, is the low amplitude, spatial

resolution, and reduced frequency bandwidth (47). The data is typically low pass filtered with a cutoff of 100 Hz. With animal models, depth electrodes (intracranial EEG) are implanted, and the resulting signal reflects the activity of a smaller population of neurons than the EEG with greater amplitudes, spatial resolution, and bandwidth (46,47). The cumulative response can be filtered to produce two signals: multiple unit spiking activity (MUA, highpass 300-500 Hz) and local field potentials (LFPs, lowpass 300-500 Hz) (48). If the electrode tip is sufficiently close to a neuronal body, single unit activity may be detected. LFP contributions are mainly derived from synaptic activity (46) and is an important band in seizure detection. The ECG reflects the electrical potential changes within the heart and can be measured with several lead configurations. The frequency content ranges up to 100 Hz. Respiration rate can be measured by a variety of techniques, but of particular interest to this work is external intercostal electromyography (EIC EMG). In rats, EIC muscles T2-T5 reflect inspiration activity, and the EMG activity has power in the 100-624 Hz frequency band (49). As more channels and data are required, an increased emphasis is placed on power consumption per amplifier data reduction techniques. To reduce demands on telemetry, feature extraction, such as seizure detection, has been used to only transmit relevant data information (50,51), which can offer significant (14:1) power reduction (51). Feature extraction also enables asynchronous telemetry to only transmit after detection (52). To quantitatively assess integrated circuit topologies during design, a comparison of algorithms and hardware-associated costs can be of great value (53-55). The size of small rodents place limits on the scale and architecture of implantable systems. As a result, the wireless technology specifications are highly dependent on the intended experimental procedure.

Integrated circuits (IC) are often used for proof of concept demonstrations in academia (28,51,56,57). Scaling these analog ICs to large animal experiments is challenging, as it requires a detailed analysis of the fabrication process to limit variability and maximize yield. Furthermore, IC fabrication, testing, and distribution are costly. It should be noted, though, that there are successful product contributions from academia to the medical research community. After many years, Reid Harrison has commercialized his biopotential ICs into the 16-64 channel amplifiers offered by InTan Technologies (58-61). Additionally, Fan et al. presented a 32 channel full system IC with a 50 kHz sampling (62), and Szuts et al. successfully designed a 64 channel IC with a 20 kHz sampling rate (63). While full system ICs will always have the most impressive specifications, the use of commercial off the shelf components (COTS) in device design can provide the needed reliability in large-scale animal experiments. Microprocessors are continually optimized for lower power and smaller applications. Perhaps the greatest advantage is that the time between iterations for COTS devices is rapid. Currently, two companies provide fully implantable systems: Millar Telemetry Systems (also known as Telemetry Research, TR) and Data Sciences International (DSI). TR systems provide up to two channels of biopotential acquisition with a battery and wireless inductive powering (64). The product is robust but large for rats often requiring intraabdominal implantation. Inductive powering provides severe limitations in range and coil alignment. DSI has smaller telemeters with up to two channels of biopotential measurements, but the battery life of the devices under operation is limited (65). Both devices lack stimulation circuitry and cannot be modified by labs for closed-loop protocols. One academic COTS device is capable of closed-loop DBS experiments; however, the device requires a large battery

backpack, is not implantable, and consumes 31.8 to 53.4 mA of current (66). Another COTS device has an impressive number of acquisition channels (up to 16 at 20 kHz sampling) and could be mated to a stimulator for closed-loop DBS; however, it is prohibitively large (35 x 35 x 35 mm), non-implantable, and only has 6 hrs of battery life (67). The power consumption and size are not suitable for chronic, continuous experiments. Table 1.1 compares the current biopotential acquisition devices. It shows the range of specifications between IC and COTS design, and demonstrates the lack of suitable closed-loop devices for use in epilepsy.

Electrical deep brain stimulation (DBS) has been FDA approved for use in Parkinson's disease, movement disorders, and recently epilepsy. DBS electrodes can be implanted in the focus for responsive stimulation or bilaterally at the anterior nucleus of the thalamus (ANT) for open loop stimulation in Canada and Europe. Neither location offers complete seizure freedom for all patients (68). Typical output waveforms are high frequency (130-200 Hz), constant voltage or current, and charge balanced. The charge balanced biphasic waveform is needed to reverse electrochemical processes occurring at the electrode site (69). In rodent models, it has been observed that high frequency stimulation (>100 Hz) reduces neuronal excitability in the focus when compared to low frequency stimulation (5 Hz) (70). A study evaluating the effectiveness of DBS at the ANT for suppression of acute seizures observed that 100 Hz stimulation raised the threshold for pharmacologically induced seizures, while 8 Hz could lead to seizures (71). Interestingly, low frequency 1 Hz stimulation of the ventral hippocampal commissural white matter tract was able to reduce seizure rates from nearly 4 seizures a day to less than 1 in a rodent epilepsy model (72).

Table 1.1 Current Full System Devices for Rodent Biopotential Recordings

Device	(64) (TR50BB)	(65) (HD-S21)	(66)	(67)	(62)	(63)
Number of recording channels	2	1 biopotential, up to 2 pressure	1	7-8 or 14-16	32	64
HP cutoff, Hz	Not reported	0.1	0.32	4-300	0.8	10-100
LP cutoff, Hz	Not reported	145	80	3000	7000	50-4500
Bandwidth, Hz	Not reported	0.1-145	0.32-80	4-3000	0.8-7000	10-4500
Sampling Rate	Up to 2 kHz	Not reported	200 Hz	20 kHz: 14-16 channels 40 kHz: 7-8 channels	50 kHz	20 kHz
Gain, dB20	Not reported		60	54-90	58	65
Input referred noise	Not reported	Not reported	Not reported	2.2 μV	10 μV	<4 μV
Telemetry	Yes; digital	Yes; digital	Yes; digital	Yes; digital	Yes; analog	Yes; analog
Electrical Stimulation channels	None	None	Yes	None	None	None
Device components	COTS	COTS	COTS	COTS	IC	IC
Implantable?	Yes	Yes	No	No	No	No
Power consumption	Not reported	Not reported	31.8-54 mA	Not reported	Not reported	645 mW
Powering Source	Rechargeable battery; inductive powering	Battery	Battery	Battery	Battery	Battery
Battery Life, hrs	4-7	2 months	Not reported	1.5	6	6
Size (L x W x H)	28.5 x 24 x 10.5 mm	5.9 cm^3	Neural interface board: 37 x 26 x 6 mm MCU board: 27 x 24 x 6 mm	35 x 35 x 35 mm	2.2 cm^3	Head board: 3.5 x 2.5 cm Transmitter: 5 x 1.5 x 0.3 cm Power and harness: 5 x 4 x 3 cm
Weight, g	13	8	4.44 (not including battery pack)	22	4.5	52

Two chronic DBS studies in two different rodent models of epilepsy actually showed that stimulation caused an increase in seizures (73,74). The variance in efficacy with respect to stimulation parameters across rodent studies show that successful DBS is heavily dependent on the seizure dynamics and location of modulation (75,76). A single set of stimulation parameters may not be sufficient to provide seizure freedom and combinatorial treatments may be needed (77). Programmable stimulation parameters are thus crucial in a DBS device. Importantly, none of the aforementioned rodent studies used a wireless, rodent implantable stimulator. As epilepsy is a chronic disease and human DBS patients are not tethered, animal studies should reflect the clinical scenario. Several wireless DBS devices have been made for rodent research (78-84). While these devices offer biphasic stimulation (78,80-82,84) and programmable parameters (78,80-84), these solutions are not suitable for use in chronic epilepsy experiments due to the size (78,80,84), range of wireless telemetry (83), requirement of inductive powering pulses to shape stimulus waveform (82), and limited battery life (78-81,83,84). Additionally, the previous stimulators were not designed for feedback-based, responsive stimulation experiments. To the author's knowledge, there is no implantable wireless device with the capacity to record biopotentials and stimulate responsively. Such a device would be of great use to the scientific community, especially in the space of epilepsy for on-demand treatment of seizures (85). This is a significant engineering challenge as the size of rodents limits the space for extensive circuitry. The devices in Tables 1.1 and 1.2 are all too large for implantable applications and still do not include complementary stimulation or recording circuitry. Innovations in miniaturization are required. Incorporation of such a device with wireless technology could address chronic behavioral

and disease experiments. Microcontroller (MCU) platforms support the implementation of closed loop architectures and investigation of a new space of experimental paradigms. This technology begins a small, but necessary step to close the larger gap between basic neuroscience research, neural engineering, and ultimate clinical application. Chapter 2 of this work presents a microcontroller centered implantable biopotential acquisition system and electrical stimulator. The stimulator is wirelessly programmable, miniature (for use in rodent experiments), and integrated into a closed-loop platform device. The device is validated *in vivo* through acute ECG, EIC EMG, and evoked potential measurements. Additionally, chronic measurements of ECG, Electrocorticogram (ECoG), and LFP are demonstrated.

Table 1.2 Current Full System Devices for Rodent Deep Brain Stimulation

Device	(79)	(81)	(82)	(84)	(83)	(78,80)
Number of stimulating channels	1	2	1	1	1	2
Biphasic stimulation?	Yes	Yes	Yes	Yes	No	Yes
Power Supply, V	3	4.65	5 V compliance	3	3	3.6
Programmable?	No	Yes; not wireless	Yes; inductive powering rectification	Yes; wireless	Yes; wireless	Yes; tethered
Stimulation current, µA	50-120	20-100	100-500	50-600	200-500	13-1000
Stimulation frequency, Hz	0-130	131	Not reported; stimulation current rise time is 10 **µs**	131	1-200	2-500
Pulse width duration, µs	0-80	60	50-250	52	30-1400	0-100% of period
Telemetry	No	No	No	Yes; inductive near field communication	Yes; radio	No
Electrical recording channels	None	None	None	None	None	None
On / Off switch	No	Yes; magnet	Yes; inductive powering	Yes; inductive near field communication	Yes; radio	No
Device components	COTS	COTS	COTS	COTS	COTS	COTS
Implantable?	No	Yes	Yes	Yes	No	Yes
Power consumption	Not reported	Not reported	Not reported	Not reported	Not reported	Not reported
Powering Source	Battery	Battery	Inductive powering	Battery	Battery	Rechargeable Battery
Battery Life	7 days	2 months	-	3-5 weeks	Not reported	10 days
Size (L x W x H)	28 x 15 x 7 mm	8 mm diameter, 30 mm length	14 x 22 x 6 mm	20 x 38.5 x 13.5 mm	20 mm diameter, 7.2 mm thick	33 x 20 x 8 mm
Weight, g	6.5	2.1	2.5	~13	14-16	11.5

1.3 Optical Deep Brain Stimulation Technologies

Optogenetics utilizes molecular tools that possess millisecond temporal resolution, high fidelity (robust response to each input), high precision (repeatable response), and a lack of immunogenicity (86). The characterization of channelrhodopsins (ChR1 and ChR2) from the algae *Chlamydomonas reinhardtii* has opened a window to genetically encode, tag, and express the protein in mammalian neurons *in vitro (87,88)* and *in vivo* (89,90). ChR2 functions as a single entity and is a non-selective cationic channel activated by blue light (87). In a mammalian physiological environment, ChR2 can effectively elicit action potentials within milliseconds of the light stimulus. Halorhodophsin (NpHR), a microbial silencer that hyperpolarize neurons through the pumping of Cl^-, has also been introduced into mammalian cells (91-93). Since the introduction of ChR2 and NpHR, rapid optimization and diversification for specific neuronal functions have emerged (94-97). The potential to control specific neurons, determine their anatomical connections, and deem them necessary and/or sufficient for a particular behavior—physiological or diseased—could have serious implications in our understanding of the brain.

Optogenetic studies fundamentally rely on the delivery of light to the neurons. Most optogenetic studies to this point have used ultra high power (UHP) lamps or lasers. Some have used LEDs. Anatomically, the two main classes of structures of interest are cortical and deep brain. To reach the targets using an UHP lamp or laser, an optical fiber can be coupled and implanted stereotactically with or without a guide cannula (98). LEDs can either be placed against a thinned skull or craniotomy to reach cortical structures. The LED can also be used similar to a laser or lamp with a coupled fiber (99). For deeper

brain structures, an optical fiber is typically used due to the limits of light transmission from scattering of photons in the parenchyma (100). LEDs are advantageous because of the low power requirements (low forward voltage compared to lasers), long operational life time, narrow band spectrum (compared to UHP lamps), and lack of extraneous components (i.e. filters) (101). LEDs can also be pulsed at nanoseconds (102), thereby easily surpassing the kinetics of opsins. UHP are more advantageous due to their high density of optical power (103) while lasers provide highly directional and coherent beams of light and have thus been used in most fiber-coupled applications (41,98,104). Others have attempted to use two-photon systems to selectively stimulate spatially distinct regions, and holography (105) with digital mirrors have been tried as well. As wirelessly powered devices must be inherently energy efficient and lightweight, UHP lamps cannot be used as a light source. Laser diodes, especially vertical cavity surface emitting lasers (VCSEL) are attractive; however, the products are sparse in academia and industry. The LED is ideal because of its low profile and dimensions, low forward voltage, and low threshold current (106).

The current molecular optogenetic systems have a high variance in performance due to several confounding factors (low conductance, trafficking, expression levels, delivery technique), and this makes specifications for optogenetic stimulators (OGS) ambiguous. It is generally agreed upon, though, that an irradiance of 1 mW/mm^2 at the plane of the targeted neuron is required for minimal activation and 10 mW/mm^2 for maximal activation (λ = 473 nm) (107). The optical spectrum of ChR2 peaks from 460-470 nm (87). In attempts to quantify the amount of radiance required from the fiber tip to activate a given volume of tissue, a Monte Carlo scheme (41,108) and Kubelka Munk

model (107) from empirical rodent brain slice data have been widely used. According to the Kubelka Munk model, a 200 μm core diameter fiber (0.37 NA) with 3 mW total power output (λ = 473 nm) can reach a depth of ~0.8 mm before falling below 1 mW/mm^2 (109). Because the models are inexact, *in vivo* brain tissue properties are difficult to acquire, and it is unknown how many of a specific neuron type needs to be recruited for specific behaviors, it may be best to derive the required optical radiance from empirical studies with behavioral outputs. Due to the variability and many unknowns, a wide range of programmable stimulation parameters is needed. This would allow psychometric curves to be determined for a given optogenetic system (110).

An optical stimulator for optogenetics should provide enough optical power for cortical and deep brain structures and offer programmable stimulation parameters. There have been a few previously published wireless stimulators that use light emitting diode (LED) as a light source. The LEDs are either implanted in the brain (42) or mounted on the skull on top of a cranial window (39,40,111). Programmable stimulation parameters are critical for consistent optical output, and behavioral modifications require specific firing patterns (112). Further, exposure at 10 – 100 mW/mm^2 (1-10 W/cm^2) of optical irradiance for a 1 second pulse can induce phototoxicity (113,114). In other reports, the Deisseroth group suggest that stimulating at 75 mW/mm^2 for 50 ms pulses is the upper limit to prevent tissue damage (104). Without optical control, tissue damage could occur. Two published devices cannot precisely control the optical power emitted (39,42). Deep brain targeting is essential for epilepsy research. The two closed-loop optogenetic studies targeted neurons within the thalamus or hippocampus (85,115). This is a challenge as coupling light from an LED to a 200 μm diameter optical fiber is inherently inefficient.

While previous devices have claimed the ability for deep brain targeting, demonstration is lacking (39,40,111). The most promising technology, a custom fabricated flexible and implantable LED interface, is not widely accessible (42). The miniaturization and design of a LED-based device with programmable stimulation parameters to better control and systematically perturb neural circuits in chronic epilepsy animal models is needed. Chapter 3 presents a microcontroller based deep brain optical stimulator for use in optogenetics. The most innovative contribution is the coupling technique as it allows the miniaturization of the optical power source. The device is validated *in vivo* with mice performing a conditioned place preference (CPP) behavioral paradigm. It is shown that conditioned place preference increases in a dose-dependent manner.

Table 1.3 Current Optical Stimulation Devices for use in Optogenetics

Device	(39)	(40)	(42)	(111)
Light Source	LED	CREE chip LED	Custom inorganic LED	Multiple LEDs
Programmable features	300 us – 300 ms (TTL)	Radio Telemetry; Millisecond resolution for y for pulse width, duration, and period of stimulation	Pulse Powering and passive rectification shapes stimulation output.	Infrared telemetry: Duration of stimulation (> 1 ms) Pulse width (> 1 ms) Frequency (< 500 Hz)
Fiber?	No	No	No	No
Deep brain capability	No	No	Yes; injectible LEDs	Yes; Fiber diameter: 0.5 mm Implant LED:
Demonstrated DBS	No	No	Yes	No
Power consumption	> 60 mW	100s of mW to >4 W	3-40 mW	Not reported
Powering source	Lithium batteries	Inductive powering	RF scavenging	Rechargeable battery (10 mAh)
Size (L x W x H)	Body: 24mm×9mm×9mm; Battery holder: 5mmOD×9mm	< 1 cm^3 without supercapacitor	Rectifier board: ~1.2 cm x 1.2 cm Probe: 0.5 mm wide 0.25 mm thick	14 mm x 14 mm x 10 mm
Weight	3.1 g	2-3 g	Not reported	2.4 g
Behavioral output	Rotations from motor cortex stimulation in mice	Rotations from motor cortex stimulation in mice	Conditioned place preference (CPP) in mice	Rotations from motor cortex stimulation in mice

1.4 Wireless Power Transfer Systems

Wireless power transfer (WPT) has a storied history and has captured the imagination of researchers since Hertz and Tesla (116). Application of WPT to implantable devices is an inherent challenge and necessary technology. Powering on demand eliminates the need for a tether and allows devices to have lifetimes far exceeding the length of chronic experiments. Radiofrequency (RF) powering is the most prevalent strategy used since it can safely deliver the power required by devices (see

Tables 1.1-3). RF powering strategies can be classified into near field, mid-field, and far-field. Power transfer occurs when a source generates alternating magnetic and electrical fields to induce currents in the receiver. Great attention must be given to requirements of the application as that dictates the appropriate WPT strategy and system architecture. Full system biomedical implants for rodents typically consume milliwatts of power, and the small size of the animals limits the size of the power receiver. As power transfer efficiencies (PTE) are typically low (< 5%), maintaining the proper impedance match conditions for optimal power delivery over a wide range of space and antenna orientations is crucial. Additionally, the WPT system must be safe. The Federal Communications Commissions limits the radiation and human exposure levels of radio waves from RF devices (117). Tissue heating and interactions are due to radiation and electric field components of the electromagnetic waves (118,119). Devices that use radiated electromagnetic fields as a powering source must be cautious of the exposure limits (120). One such previous device exceeded the FCC guidelines (42), and end users should be given proper warning. At frequencies below 10 MHz, the magnetic fields have little known direct interactions with biological tissues (118,121). WPT systems should operate below 10 MHz with primarily magnetic induction or have an extensive analysis showing that the exposure is safe for use (122).

The dominant method in the near field powering is inductive powering. Energy is coupled through magnetic induction, and this technique is widely used in commercial applications. Yet with many years of development and optimization, there are few clinical and research products. The inherent limitation is true omnidirectional powering in free space. Between the transmit and receive coils there is only a limited operating range

and coil orientation in which strong induction is achieved (123,124). Transcutaneous energy transfer systems (TETS) have been proposed for decades (125) and clinically implemented with little success (124,126,127). Inductive powering has been implemented in many implantable devices, but the range is typically limited to less than 10 cm for receive coils 6 cm in diameter or less (128-131). The most extensive research product developed is the Enercage inductive powering platform (132). The Enercage is an array of overlapping transmit spiral planar coils with multiple controllers to optimize power transfer to the receive unit. The power transfer efficiency at a 15 cm vertical distance is approximately 2-3%, and the system can deliver 20 mW to a 500 Ω load at 12 cm (132). While this is an impressive engineering solution, the platform is incredibly sophisticated; difficult to reproduce; limited in vertical powering range; and has two coils (40 and 25 mm diameters), a monopole antenna (48 mm) and a large supercapacitor as an energy buffer on the power receive board (132). Such a powering system is not suitable for chronic epilepsy experiments.

Mid-field RF powering is a novel technique using both magnetic induction and electrical radiation (122,133). Potential applications include those where the source and receiver are approximately a wavelength apart. At this distance, efficiencies are higher than using inductive near field; however, the current physical setup is rigid to the optimized distance (122). A major advantage is the miniaturization of the receive coil. Recently, a ~3 mm diameter receive coil and a custom IC LED driver was implanted in a freely behaving mouse (134). At a distance of 15 cm and 500 mW output power (1.6 GHz), 50 μW is received when embedded 0.75 cm deep in porcine tissue (134). While this method is promising, especially for coil miniaturization, it is also confined to a

limited vertical range and not currently amenable for design. Designers must wait for simplified mathematical methods and further characterization. The far-field couples energy through electrical radiation and operates in the 100's of MHz to low GHz. This method can power at distances much greater than the wavelength and offers more freedom with orientation mismatches, but the efficiencies are low (135) and not suitable or safe for implantable applications requiring milliwatts of power. Tissue penetration is shallow, and safe exposure levels set a ceiling for radiated power from the source (120).

Strongly coupled magnetic resonance (SCMR) for wireless power transfer is a non-radiative, mid range powering method (136). Energy is coupled by a resonant magnetic field, and the physical principles are the same as inductive powering (123). The primary differences from inductive powering are the use of high quality factor components and system architectures that allow optimization of the impedance match condition (123,137,138). These two factors increase the range of power transfer. As demonstrated by Kurs et al., high power transfer efficiencies can be achieved at distances several times the diameter of the powering coils (136). Even with large mismatches coils sizes power transfer efficiencies can reach 9.1% across multiple receivers (138). This feature is critical as implantable devices necessitate miniaturization. SCMR power transfer has been quickly adopted and already seen prototypes for clinical use (139,140). Application of SCMR power transfer to rodent implantable devices, though, has been lacking. Xu et al. presented a mat-based WPT system similar to the Enercage; however, this was only realized through simulation for a specific distance as the interactions between an array of resonant coils is quite complex (141). Table 1.4 compares a selection of inductive, midfield, and SCMR power methods. A powering system for chronic

epilepsy experiments would require continuous powering within the volume of a housing unit. According to the NIH Guide for the Care and Use of Laboratory Animals, group housing rats weighing 400-500 g require 60 in^2/rat of floor space and 7 inches of height. Often rats induced with seizures are singly housed and would require more floor space. An 11 x 11 x 11 in^3 (L x W x H) volume sufficiently house a large rat with seizures**.** None of the solutions in Table 1.4 adequately address this volume with a miniature, implantable receive coil. Recently, the design of SCMR powering systems has been greatly simplified through microwave filter synthesis techniques (142-145). By simply modeling a SCMR WPT system as a bandpass filter, optimal impedance match conditions for maximum power transfer can be met with simple and miniature circuit topologies (143,144,146). In particular, the resonantly coupled filter energy transfer (RCFET) method optimizes power transfer simply through measurement of the physical coil parameters (147). Using the RCFET method, Chapter 4 of this work presents an omnidirectional powering cage to support the technologies detailed in chapters 2 and 3. The powering strategy is designed and characterized with filter synthesis theory and validated *in vivo* with freely behaving rats.

Table 1.4 Wireless Power Transfer Systems

WPT system	(131)	(130)	(132)	(134)	(141)	(138)	(140)
Method	Inductive	Inductive	Inductive	Midfield	SCMR	SCMR	SCMR
Powering frequency	6.78 MHz	3.18 MHz	13.56 MHz	1.6 GHz	26.6 MHz	8.3 MHz	13.56 MHz
Powering Range	1.5 cm	4 cm	15 cm	15 cm	8 cm	17 cm	< 50% PTE: 120 cm <10% PTE: 160 cm
Powering Area	Not reported	Not reported	3538 cm^2 or larger	8 cm diameter	16 x 16 cm	Not reported	Dependent on Tx coil size
Source Coil	5.2 cm	4.8 cm	unit tile: 515 x 450 mm can add tiles to create larger area	Cross slot source 5 cm below a tank: powers a tank with 8 cm diameter	Seven 13.2 cm spiral coils arranged in a hexagon	30 cm	Source coil: 31 cm Relay coil: 59 cm
Receive Coil diameter	1 cm	0.6 cm	25 mm	~3 mm	Diameter: 25 mm Height: 7 mm	1.3 cm	9.5 cm
Receive board size	Not reported	4.5 x 7.5 x 1 mm	40 mm diameter; 20 mm height	~3 x 3 mm	Inside receive coil	Not reported	Not reported
Power output	259 mW	Not reported	0.5 - 4 W	500 mW	Not reported	~310 mW	8.1 W
Power received	50 mW	341 μW	20 mW	50 μW	1.19 – 1.44 V; no load specified	3.3 mW	~4.5 W
Notes			Demonstrated *in vivo* with rats	Demonstrated *in vivo* with mice		Powered LEDs in demonstration	Can use relay coils to extend range. Powering distance and area are coil size dependent.

1.5 Epilepsy

It is estimated that over 50 million individuals across the globe suffer from epilepsy (9). Epidemiological studies reveal that 20-30% of patients suffer from refractory or drug-resistant seizures (148). As defined by the ILAE, epilepsy is "a condition characterized by recurrent (two or more) epileptic seizures, unprovoked by any immediate identified cause" (149). Importantly, the pathological state can cause severe insults in cognitive development, autonomic function, and motor control, which lead to a dramatic decrease in the quality of life and possibly death. Often, drug-resistant individuals will develop anxiety, depression, and other psychiatric disorders (148). Furthermore, epilepsy can be socially polarizing. Strong stigmas exist in certain cultures which lead to under diagnosis of the condition in surveillance studies and negative societal attitudes towards those affected (150). The CURE Epilepsy foundation estimates the United States spends approximately $15.5 billion annually and the cost will continue to rise, especially with soldiers returning from overseas conflicts with traumatic brain injury (151). With the profound personal, social, and economic burden of epilepsy, new tools are under development to better understand and treat the disease.

Since epilepsy is a complex and diverse disease, it is important to characterize seizures carefully. As described by the ILAE, epileptic seizures are categorized into two distinct types: generalized and partial (149). Generalized seizures are thought to affect the entire brain from the onset. Partial seizures are believed to manifest from a local focus, recruit other neurons, and can possibly generalize. Partial seizures are further classified into simple and complex. Individuals with simple seizures do not lose consciousness while those with complex do. The etiologies of epilepsy are idiopathic (mainly genetic),

generalized (identifiable prior insult), and cryptogenic (unknown) and the temporal progression towards epilepsy is known as epileptogensis (152). Interventional strategies may be dependent on the stage of epileptogensis (Figure 1.1).

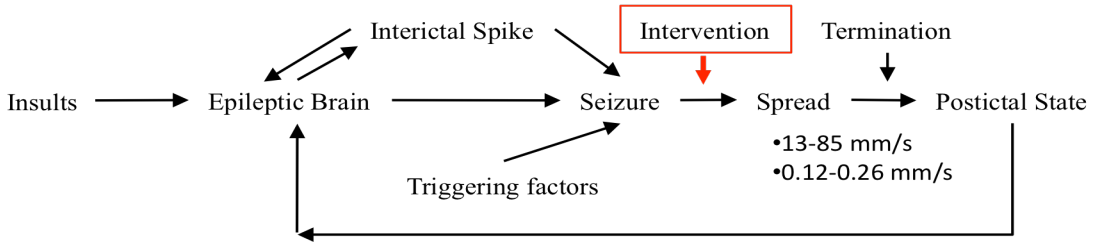

Figure 1.1 Epileptogenesis. A normal brain undergoes a genetic, known, or unknown insult and develops into an epileptic brain. Interictal spikes are seen on EEG and normally do not progress to seizures. If underlying triggering factors are present, neurons begin recruitment and seizures result. The ictal wavefront propagates at speeds of 13-85 mm/s in cortical rat slices (153) and 0.12 – 0.26 mm/s in human cortical tissue (21).

Current therapies in drug-resistant epilepsy are surgical resections or lesions, ketogenic diet, the vagal nerve stimulator, and deep brain stimulation. Trigeminal nerve stimulation (TNS) is currently under investigation in the United States. The responder rates of the devices for a ≥50% reduction in seizures are widely variable, and most patients do not become seizure free (154,155). Closed-loop stimulation is an old concept, though, only recently has a product been under clinical investigation (156). Responsive stimulation aims to prevent the spread of seizures (Figure 1.1) before it recruits more neurons. Closed-loop stimulation may be more advantageous from a biological perspective as neurons can be hyper-stimulated into a refractory state termed stimulation-induced depression of neuronal excitation (SIDNE) (157). Additionally, from a device perspective, by stimulating only when required, battery-life of devices can be extended. In

NeuroPace's RNS clinical trial, only 46% of the patients met the 50% reduction responder rate (156). These results do not out perform previous open loop strategies. The reasons are unclear, but recent studies have shown promise. While all of the aforementioned treatments are beneficial to many patients, it is clear that new and optimized treatments are needed for complete seizure freedom. Two landmark studies using optogenetics demonstrated seizures could be stopped immediately upon detection with optical stimulation (85,115). Translating and optimizing the molecular and electrical based closed-loop strategies into clinical efficacy will require device-based tools for chronic neuromodulation. Chapters 2-4 present a platform of technologies developed specifically for chronic neuromodulation in rodent epilepsy models.

1.6 Sudden Unexpected Death in Epilepsy

Sudden unexpected death in epilepsy (SUDEP) is a category of death afflicting patients with epilepsy. Persons with epilepsy are greater than 20 times more likely to die unexpectedly than the general population (158), and refractory epilepsy patients are at even greater risks. By definition, definite SUDEP meets the following criteria (159): 1) sudden 2) unexpected 3) witnessed or unwitnessed 4) if witnessed, no non-epilepsy related identifiable cause such as drowning 5) seizure or no seizure observed 6) if a seizure is observed, it cannot be status epilepticus (seizure duration ≥ 30 minutes) 7) no causal evidence of death during autopsy. The mechanisms of SUDEP are poorly understood but are thought to include seizure related cardiac and respiratory arrest, and severe dysfunction of autonomic regulation through limbic, sympathetic, and parasympathetic pathways (160-162). Nei et al., observed cardiac repolarization

abnormalities and that the heart rate increased more in SUDEP patients (149 beats/min) when compared to intractable epilepsy patients (126 beats/min) during the ictal period of a seizure (163). Cardiac arrhythmias are common in intractable epilepsy patients as well (164), and pinpointing what leads to SUDEP will require further studies. A Lack of respiratory drive due to seizures leads to postictal apnea, which then causes hypoxia, hypoxemia, and acidosis (162,165,166). A dysfunctional cardiorespiratory feedback system can prevent recovery and result in death (165). In a study with audiogenic seizures, on oxygen rich environment provided after a seizure was able to prevent postictal sudden death (166). Known risk factors include: poorly controlled seizures, using several antiepileptic drugs (AED) with little therapeutic effect, 3-12 generalized tonic clonic seizures (GTCS) per year, frequent long seizures, and young males (160). Additionally, those with genetic susceptibility to cardiac arrhythmias are more likely to experience SUDEP (167). Currently, there are no effective prevention measures. Physicians can identify those most at risk and offer precautions (161). The vagus nerve stimulator (VNS) could prevent cardiac instability but this is still unclear (168). It has been observed that SUDEP often occurs during sleep at night (163,169), so tools for continuous monitoring are needed. To provide more efficacious prevention and treatment measures, a better understanding of SUDEP is required. A key challenge is to relate epileptogenesis and seizure activity in specific brain regions with cardiac and respiratory signals in animal models. Autonomic regulation can be studied by observing heart rate variability with respect to other physiological measures such as breathing and blood pressure (170,171). As SUDEP is currently unpredictable, chronic monitoring is needed to observe the trajectory of the pathology. Animal models are needed that reflect the

human phenotypes and mechanisms. Critically, miniature wireless technology provides an essential toolset for SUDEP researchers. Chapter 2 demonstrates a recording platform that allows 4 channels of biopotential acquisition to observe a combination of ECoG, LFP, respiratory EMG and ECG activity.

1.7 Urinary Urge Incontinence

Urinary incontinence (UI) is the inability to control the mictruition. Greater than 25% of women (172) and greater than 11% of men (173) 60 or older report UI. UI is divided into stress incontinence (external urethral sphincter dysreguation) and urge incontinence (bladder control dysregulation). Urge incontinence is typically more severe and requires medical treatment. The etiologies are wide ranging from aging to neurological disorders, and the symptom can cause great physical, psychological, and social discomfort. Central nervous system control of bladder function is regulated through the periaqueductal grey (PAG). The PAG is under tonic GABAergic inhibition, and when the bladder is full, stretch receptors in the bladder send ascending signals through the spinal cord to the midbrain. The PAG is disinhibited, and an efferent voiding signal is sent back down to the bladder for mictruition. Previously, it has been established that deep brain stimulation of the PAG in both rats and humans can prevent voiding in a full bladder (174). This has large implications for patients with urge incontinence, but before human clinic trials can begin, chronic device based animal studies should be pursued. Closed-loop technologies can be used to measure the bladder pressure and stimulate the PAG accordingly to offer control over the urge to void. Chapter 2 details a pressure sensing device prototype and validates the technology in an acute *in vivo* bladder pressure experiment.

CHAPTER 2. BUILDING BLOCKS FOR A CLOSED LOOP SYSTEM

2.1 Introduction

Wireless closed-loop devices for epilepsy are designed to gather and input information responsively with minimal to no side effects. The system architecture determines the functional capabilities, and seamless integration of hardware blocks is necessary for robust full system performance. The key hardware blocks include the physical probes, analog front-end acquisition (AFE), analog-to-digital converter (ADC), stimulation circuit (electrical or optical), telemetry, and power management (Figure 2.1) Biocompatible, metal electrodes will be used to acquire information from a subject, and the electrode tissue interface must be considered during design of the input analog front end (AFE) (175). Delivering information or a stimulus can occur electrically or optically with electrodes or LEDs, respectively. Control of the stimulation parameters is critical. It is well known that specific stimulation protocols can provide relief in Parkinson's disease (176), affect behavior (112), and selectively activate neurons (177). End users must have a simple way to communicate to the device, and this is executed through a graphical user interface (GUI) and basestation. While less glamorous in the research realm, seamless operation of the GUI and basestation is required for adoption by external end users. Wireless powering for continuous powering is an active area of research and will be discussed in chapter 4.

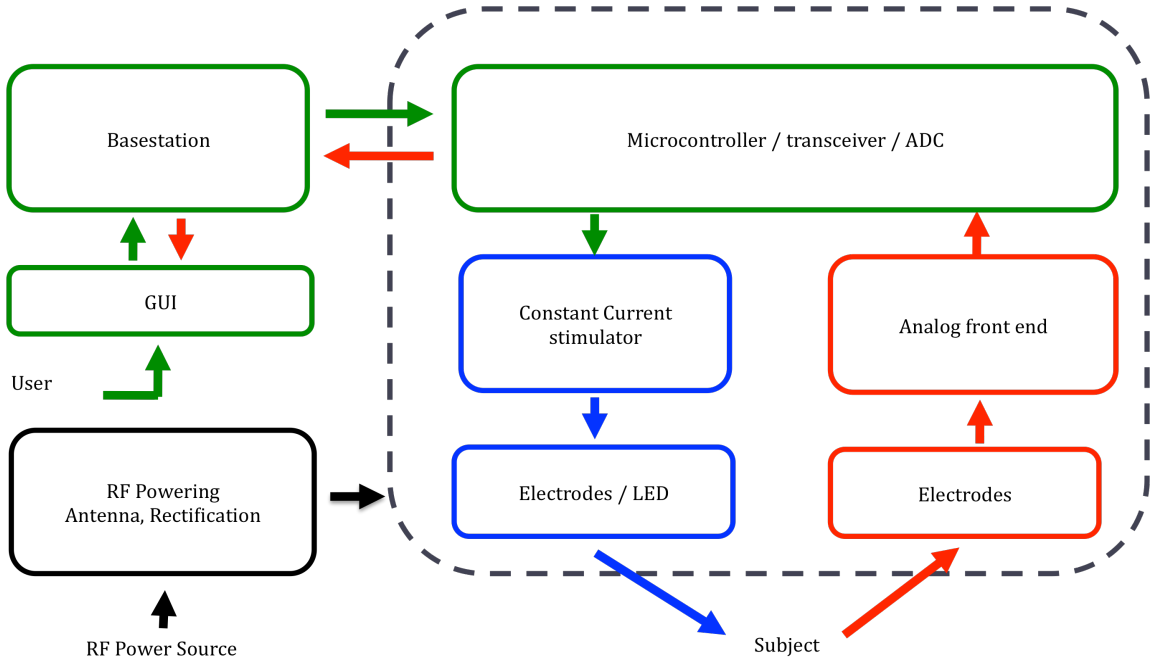

Figure 2.1 Closed-loop system blocks for complete wireless operation. Red arrows show the path of information delivery to the user. Green arrows show the path of user controllability and blue arrows show the delivery of information to the subject. Black arrows show the powering path. The dotted line outlines the physical components on the device.

A designer must always consider how all blocks of the system interact. This chapter will specifically focus on the device platform and the design considerations. The GUI and basestation are contributions of other individuals and will not be discussed. Section 2.2 provides a brief overview of the device for closed-loop modulation. The device has 1 channel for biopotential acquisition and 1 for channel stimulation. Sections 2.3 and 2.4 detail the biopotential acquisition and stimulator design, respectively. Section 2.5 briefly describes the MCU operation and telemetry. Section 2.6 details the *in vivo* validation of ECG, EMG, ECoG and LFP. Section 2.7 then applies the platform for pressure monitoring in urinary incontinence. The novel intellectual contributions to this work are:

1) The design and characterization of a miniature, implantable closed-loop device for biopotential acquisiton and electrical stimulation
2) *In vivo* application of the wireless platform in preliminary studies of SUDEP and urinary urge incontinence.

2.2 A Miniature Closed-Loop Device for Neuromodulation

The device platform consist of subsystems to detect and amplify biological signals, input a stimulus, communicate through telemetry, make logical decisions, and receive power. This section presents a miniature closed-loop device with 1 channel of biopotential acquisition and 1 channel electrical stimulation. The device block diagram is depicted in Figure 2.2a. The analog front end (AFE) signal chain consists an instrumentation amplifier (INA) cascaded with an operational amplifier (OPA). An 8-10 bit analog to digital converter (ADC) internal to the microcontroller (MCU) digitizes the amplified biopotential. The MCU packages the data for telemetry through an onboard radio at 2.4 GHz. The constant current stimulator consists of a current sink topology with dual pole, dual throw switches at the output to flip the polarity of delivered current. The miniature device is pictured in Figure 2.2b,c with the AFE on the top side and the stimulator circuitry on the bottom side. The device is 7 x 14 x 3 mm (L x W x H) and weighs less than 0.7 g (powering circuitry not included). Detailed descriptions of the circuit topologies are provided in Sections 2.3-2.5. As commercial off the shelf (COTS) components are used for fast iterations and widespread accessibility, the internal structures of the electrical systems are not focused upon. Instead, emphasis is placed on functional performance and design tradeoffs. The building blocks presented are the first

generation technologies for this platform. The individual subsystems used for acquisition and stimulation can be combined to design devices at a small size for specific experiments. For instance, a 4 channel recording system is used in Section 2.7 for preliminary experiments to study SUDEP. 1 channel stimulation device can be combined with biopotential acquisition blocks for closed-loop protocols.

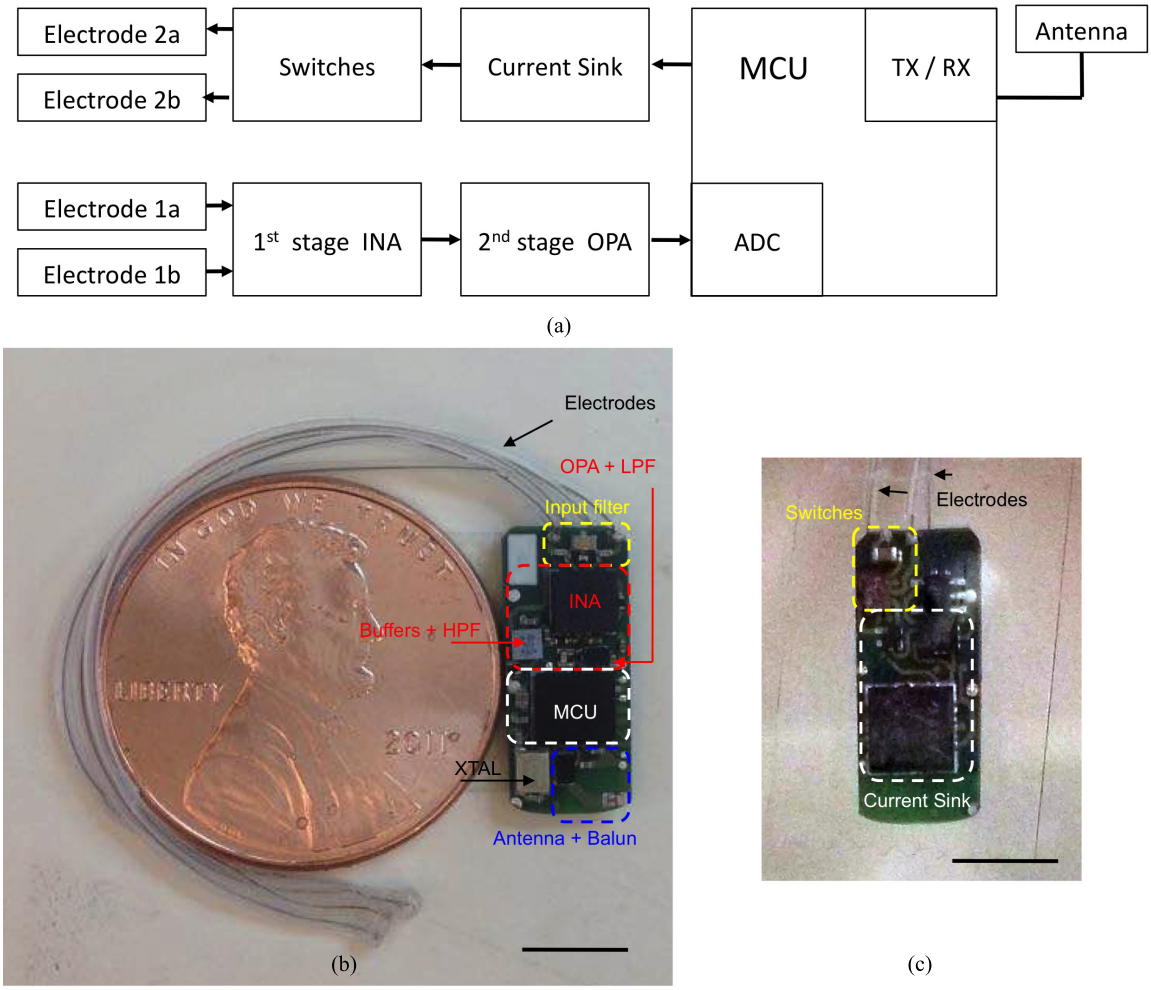

Figure 2.2 A miniature closed-loop device with 1 channel of biopotential acquisition and 1 channel electrical stimulation. a) Block diagram of the device. Electrodes 1a and 1b are the probes to connect the tissue to device. Two stages of amplification are performed. The first stage is an instrumentation amplifier (INA) and the second stage is an operational amplifier (OPA). Digitization of the analog signal is performed by the internal analog to digital converter (ADC) of the microcontroller

(MCU). The MCU also has a radio for two way communications with the basestation (not shown). The constant current stimulator is a standard current sink with switches to flip the polarity of stimulation. Electrodes 2a and 2b deliver the current to the tissue. For detailed circuit diagrams of the analog front end (AFE) and stimulator see Figure 3.3 and 3.5, respectively. b) The top side of the device contains the AFE circuitry. The device is pictured with flexible cuff electrodes used in peripheral nerve modulation. XTAL is the crystal for the MCU. Refer to block diagram for connections. c) The bottom side of the device contains the stimulation circuitry.

2.3 Biopotential Acquisition - Analog Front End

Biopotentials can be found anywhere a time varying electric dipole exists. While the electroencephalogram (EEG) is the gold standard in the clinical workup of epilepsy and other neural disorders, researchers are also interested: action potentials, local field potentials (LFP), electrocorticograms (ECoG), electrocardiograms (ECG), and electromyograms (EMG). The frequency and voltage amplitude content of these signals are depicted in Figure 2.3 (58,178). Current rodent studies in epilepsy primarily use EEG and LFP signals for analysis, and the frequency content is below 200 Hz. The ECG frequency content is within this bandwidth, but higher frequency EMG activity can be observed. The electrodes being used determine the detectable EMG bandwidth. Typical surface EMG is limited to 500 Hz activity, while fine intramuscular probes can detect motor unit action potentials with frequencies over 1 kHz (179). As this work is focused on using EMG measurements to determine respiration rates (49), motor units do not need to be observed. To satisfy the bandwidth required to observe electrographic seizures, ECG, and EMG activity, the low pass filter is designed for 1 kHz. If higher frequency signals are of interest to a particular experiment, the low pass filter can be reconfigured.

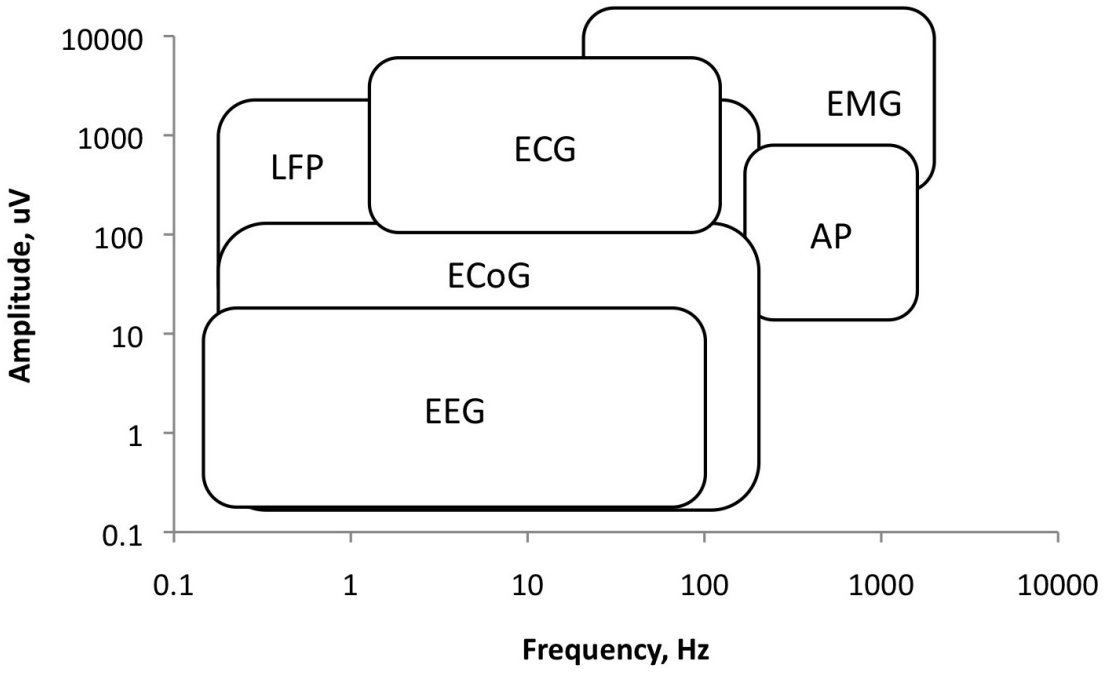

Figure 2.3 Frequency content and amplitudes of common biopotentials.

In a typical signal chain, each set of electrodes interfaces with a differential amplification scheme. After the first stage of amplification, often termed preamplification, the signal is high pass filtered to remove any slow potentials or DC offsets. A second stage of amplification is used for increased gain, and the low pass filter prevents aliasing. The resulting signal is digitized and transmitted. The signal chain from electrode output (amplifier input) to digitization is termed the analog front end (AFE). The purpose of the AFE is to differentiate the signal from noise; it must have the ability to measure a specific electrical marker that correlates to a physiologically relevant event. Figure 2.4 shows a typical signal chain and how the device accomplishes the features.

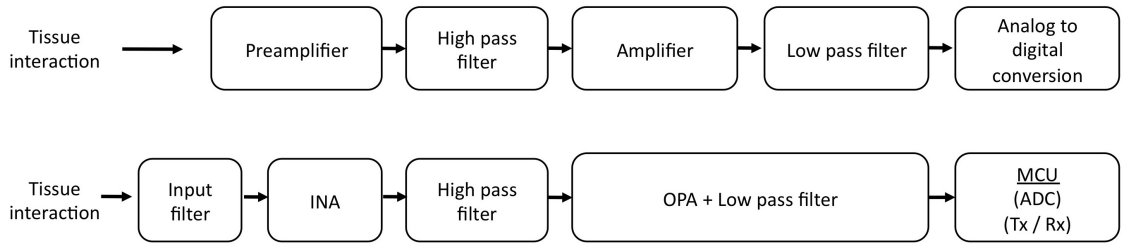

Figure 2.4 AFE features. (Top) Typical features in a generic amplifier chain. (Bottom) The AFE specific to the closed-loop device. An input filter limits radiofrequency interference and an instrumentation amplifier (INA) is the first gain stage. A high pass filter removes DC offsets and then an operational amplifier (OPA) serves as both the second stage of amplification and anti-aliasing low pass filter. The ADC in the MCU digitizes the amplified signal.

To maintain signal fidelity, additional important design features of the AFE are listed in Table 2.1. A detailed circuit schematic is provided in Figure 2.5. This schematic will be used to explain features and design choices. The AFE uses a cascaded amplifier topology with input and output filters (Figure 2.4-5). The electrode inputs are configured differentially and connected to an INA. Input filters between the electrodes and INA are used and component values are carefully implemented to minimize conversion of common mode to differential signals. The INA rejects common mode noise and provides preamplification. The second stage amplifier provides further amplification and signal conditioning. The topology only requires 2 physical connections to the subject and is considered ground free—no ground electrode is connected to the subject (180). This can prevent current discharge into the subject under device fault conditions and ease the surgical procedure.

Table 2.1 Analog Front End Design Specifications

Design Parameter	**Specification**	**Reason**
Input impedance	Hundreds MΩs - GΩs	To prevent voltage division and observe activity at point of electrode. Exact impedance needed depends on electrodes used.
CMRR	80 dB	Rejection noise, primarily from main power lines (50 or 60 Hz)
Low input-referred noise	< 10 μV	To observe small signals
Gain	60 dB (1000:1)	Amplify and increase resolution
Input dynamic range	35.56 dB	Measure wide range of signal amplitudes (20 μV-1.2 mV)
Size	<5 x 10 mm^2	Miniaturization
Power consumption	< 280 $\mu W/mm^2$	Prevent heating of biological tissue. Minimize as much as possible to lessen powering demands

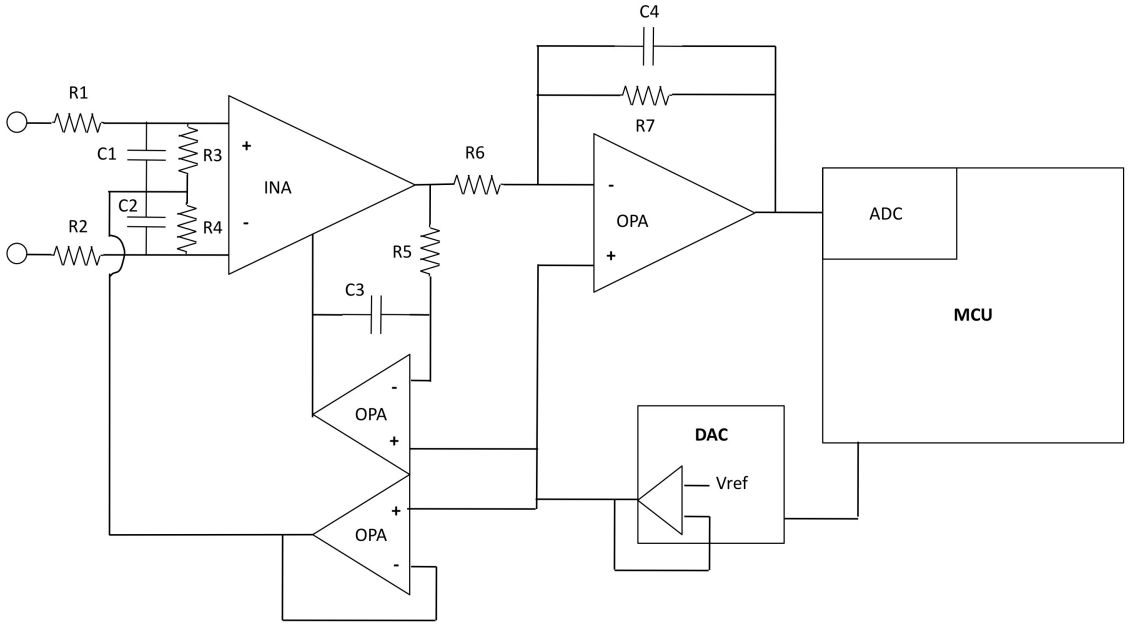

Figure 2.5 Circuit Topology of Analog Front End. INA = instrumentation amplifier, OPA = operational amplifier, MCU = microcontroller, ADC = analog to digital converter, DAC = digital to analog converter, R = resistor, C = capacitor.

2.3.1 Input Impedance

Input impedance of the INA is ideally infinite to prevent voltage division with the electrode. There are two input impedances, the differential, Z_{dm}, and common mode, Z_{cm}. The differential impedance must be large to maintain signal integrity, and the common mode impedance should be sized to minimize noise. The reported input impedance, typically differential, of most clinical amplifiers used in epilepsy centers is 10-50 MΩs (181). Electrode impedance is frequency dependent, changes over time, and variable between electrodes. From 1 Hz and 2 kHz, microelectrode impedances can range from a few MΩs to 10 kΩs, respectively (182). Geddes et al. reported that faithful EMG recordings could be acquired with input impedances ranging from 1 to 88 MΩ for stainless steel electrodes having areas of 500 to 125000 μm^2 (183). More recently, it was suggested that at least a 1 GΩ input impedance is required to prevent signal distortion of lower frequency content when microelectrodes are used in the clinic (181). Achieving a 1 GΩ input impedance with limited space is not always practical, though. For instance, the state-of-the-art Intan Technologies RHD2000 chip has a 13 MΩ input impedance at 1 kHz. Unfortunately, commercial devices from Telemetry Research and DSI do not report the input impedance specification. In Figure 2.5, the INA used is the INA333 since it has a differential input impedance of 100 GΩ (184). The common mode impedance, though, is determined by input biasing resistors, R_3 and R_4, and filtering capacitors, C_1 and C_2. Here, the discussion will be focused on the resistor values as the capacitors are set to 100 pF to minimize RF interference (Section 2.3.4). The resistors are required to center the input signal, and since Z_{dm} is essentially infinite compared to Z_{cm}, common mode signals see R_3 and R_4 as an impedance divider network with the electrode impedance (185). If R_3

and R_4 are not large with respect to the electrode impedance, then mismatches in electrode impedances will result in larger contributions from common mode to differential signal conversion (potential divider effect, Section 2.3.3) (186). This will degrade the signal quality by introducing noise. In this work, 10 MΩ bias resistors with a 1% tolerance were chosen since the power line noise contribution is simulated to be a few μVs with a CMRR of 80 dB (Section 2.3.3). Novel topologies should be investigated to further decrease noise contributions in low power, two-electrode topologies.

2.3.2 Common Mode Rejection Ratio and Differential Gain

The common mode rejection ratio (CMRR) is the ratio of differential gain, A_d, to common gain, A_{cm} (equations 2.1-3). A high CMRR amplifies differential signals while minimizing common mode signals. Impedance mismatches in the internal circuitry cause common mode signals to appear differential, and this will lower the CMRR. External components at the input of the INA (R1-4 and C1-2) can also severely degrade CMRR; this is known as the potential divider effect. To demonstrate, a 10 pF capacitance is added to C2, which creates a 10% mismatch between C1 and C2 (Figure 2.5). Figure 2.6 shows a greater than 20 dB decrease in CMRR due to the 10 pF mismatch (red trace). The potential divider effect does not reduce the differential gain (Figure 2.7), so it is important to measure the common mode gain to detect CMRR degradation. By selecting well-matched (within 1%, NP0 temperature rating) input resistors and capacitors, a CMRR of 100 dB at 60 Hz is achieved (blue trace, Figure 2.6). The CMRR is measured using a dynamic signal analyzer. First, the differential gain is measured by applying a differential mode voltage source. Then the common mode gain is measured by applying a

common mode voltage source (input terminals connected together). The gain is the ratio of V_{out} over V_{in}. V_{in} is either the differential input voltage, V_{dm}, or the common mode input voltage, V_{cm} (Equations 2.1-2.2). CMRR is obtained with Equation 2.3.

$$A_d = \frac{V_{dm}}{V_{out}} \tag{2.1}$$

$$A_{cm} = \frac{V_{cm}}{V_{out}} \tag{2.2}$$

$$CMRR = 20\log_{10}\left(\frac{A_d}{A_{cm}}\right) \tag{2.3}$$

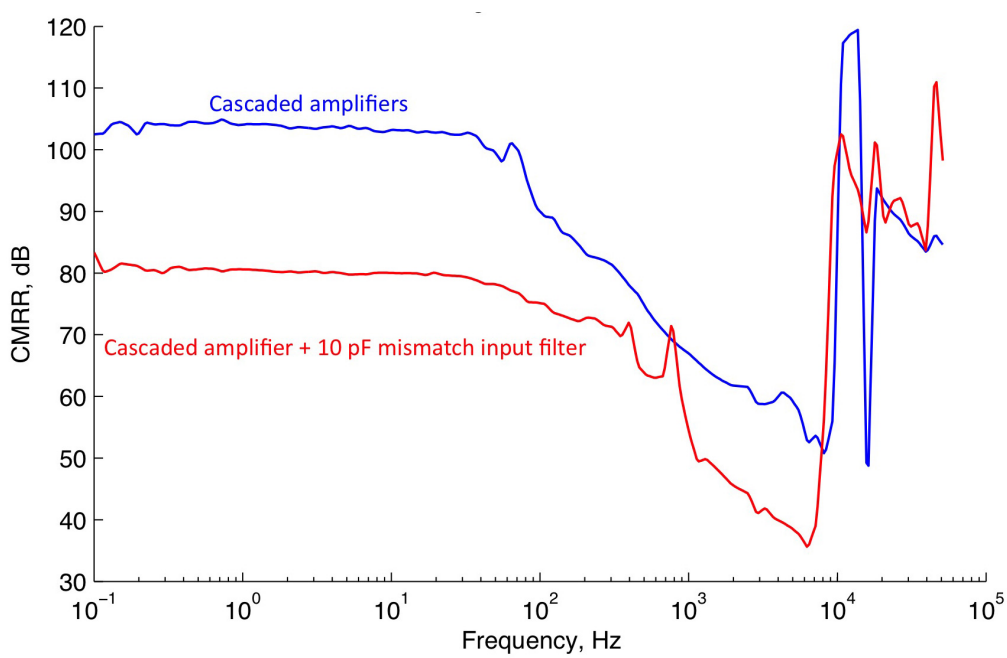

Figure 2.6 High common mode rejection ratio (CMRR) is achieved with well-matched components and degraded with mismatches. Cascaded amplifier topology was used with 1% matched components (blue). Potential divider effect is observed when 10 pF is added to one input capacitor to create a 10% mismatch (red).

The cascaded amplifier topology allows the gain to be distributed in order to maintain bandwidth and eliminate undesirable DC offset voltages. Electrode-tissue interactions create DC-potential offsets that can saturate the INA if the gain is too high (187). The first stage gain is designed for 20 dB (10:1) and measured at 19.99 dB (Figure 2.7, black trace). With a supply voltage of 1.8 V, the tolerable electrode offset voltages are less than 180 mV. The high pass filter eliminates any DC offsets. The second stage gain is designed for 40 dB (100:1) resulting in a total gain of 60 dB (Figure 2.7, blue trace). The total gain is 59.43 dB which is in good agreement with design. The high pass filter is controlled by R5 and C3. The low pass is controlled by R7 and C4. The respective 3 dB cutoffs are 0.72 Hz and 1.13 kHz. The 3 dB cutoff frequency, f_c, can be calculated by equation 2.4 where R and C are the resistor and capacitor involved in the specific filter.

$$f_c = \frac{1}{2\pi RC} \tag{2.4}$$

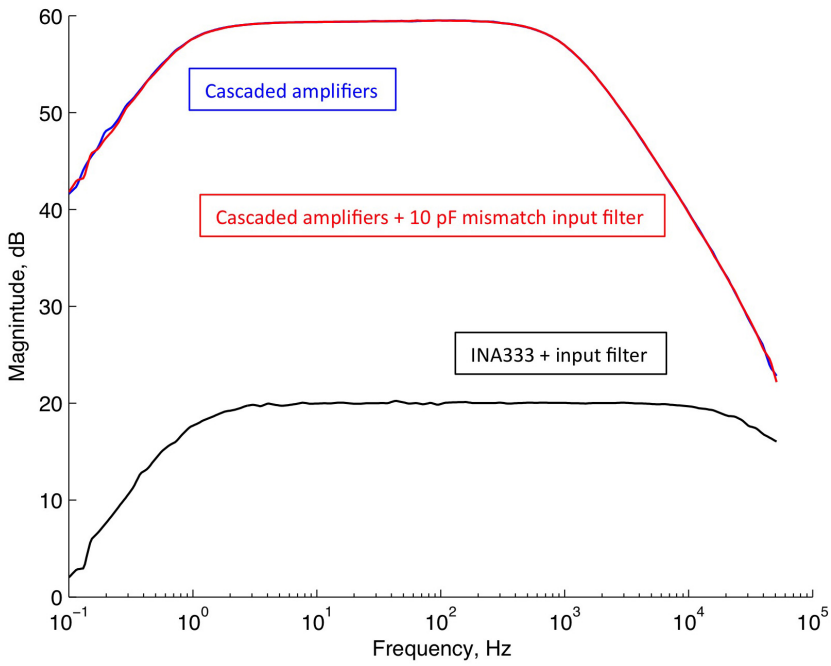

Figure 2.7 Gain and bandwidth of the analog front end. Three conditions were measured to observe how component addition affected the differential gain. Black = INA333 + the input low pass filter, blue = cascaded amplifier topology with input filter, red = cascaded amplifier topology with 10 pF mismatch at the input filter (see Figure 3.6 for CMRR degradation). High pass 3 dB cutoff frequency = 0.72 Hz, Low pass 3 dB cutoff frequency = 1.13 kHz. Cascaded amplifier (blue) gain = 59.43 dB in the pass band.

2.3.3 Power Line Noise Reduction

Noise is introduced to the analog front end by magnetic induction and capacitive coupling of electrical fields (186). From Faraday's Law, conducting loops allow magnetic fields to induce an electromotive force (emf). The resulting emf pushes current and creates noise. Alternating electrical fields displace charges in the electrode leads and subject's body. This also results in noise. Typically, the 50 or 60 Hz main power line is the primary noise source; however, in a wireless powered system, it is important to consider noise contributions from a the specific powering setup as well. Power line noise

will first be addressed. Figure 2.8 is the circuit representation of noise coupling into a two-electrode ground free circuit topology (180). Equation 2.5 represents the total noise at a specific frequency that is seen by a differential amplifier as depicted in Figure 2.8 (186). The total current seen by the subject's body due to the power mains coupling through C_1 is represented by i_{d1}. The KBS term represents noise from magnetic induction. K is a constant, B is the magnetic flux density, and S is the loop area that allows magnetic induction. The $i_{b1}Z_{e1}$ and $i_{b2}Z_{e2}$ terms represent the voltage noise caused by capacitive coupling into the leads. Z_{e1} and Z_{e2} represent the impedance of each electrode and i_{b1} and i_{b2} are the currents passing through each branch. Z_b is the impedance of the subject's body and i_b is the current flow in the body. The current from i_{d1} can flow to earth ground through the subject, i_{d2}, or through the common mode impedance (Z_{cm1} or Z_{cm2}) of the INA, i_{d3} (typically 1 nA) (180). The final term reflects the voltage noise due to current flowing through Z_{cm}. The bracketed portion shows the effect of the CMRR and potential divider effect. The KBS term can be ignored by minimizing conducting loop area with short connections, shielding, or twisting the electrode leads. This reduces the S term to a negligible value (assume S = 0). Previously, it has been shown that the currents through the electrode and Z_b are relatively small and can be neglected (180,186). Assuming that the common mode impedance of the INA is much greater than the electrode impedances (assume $Z_{cm} >> Z_e$), then remaining factors are the common mode impedance, CMRR, and potential divider effect. Thakor and Webster previously derived the simplified equation for a ground free, 2 electrode telemetry configuration (equation 2.6) (180). Z_d represents the mismatch between electrode impedances, and Z_{cm1} and Z_{cm2} are assumed to be equal (Z_{cm}).

$$V_n = KBS + i_{b1}Z_{e1} - i_{b2}Z_{e2} + i_b Z_b + i_d Z_g \left[\frac{1}{CMRR} + \left(\frac{Z_{e1}}{Z_{cm1} + Z_{e1}} - \frac{Z_{e2}}{Z_{cm2} + Z_{e2}} \right) \right] \tag{2.5}$$

$$V_n = i_{d3} \frac{Z_{cm}}{2} \left[\frac{1}{CMRR} + \left(\frac{Z_d}{Z_{cm}} \right) \right] \tag{2.6}$$

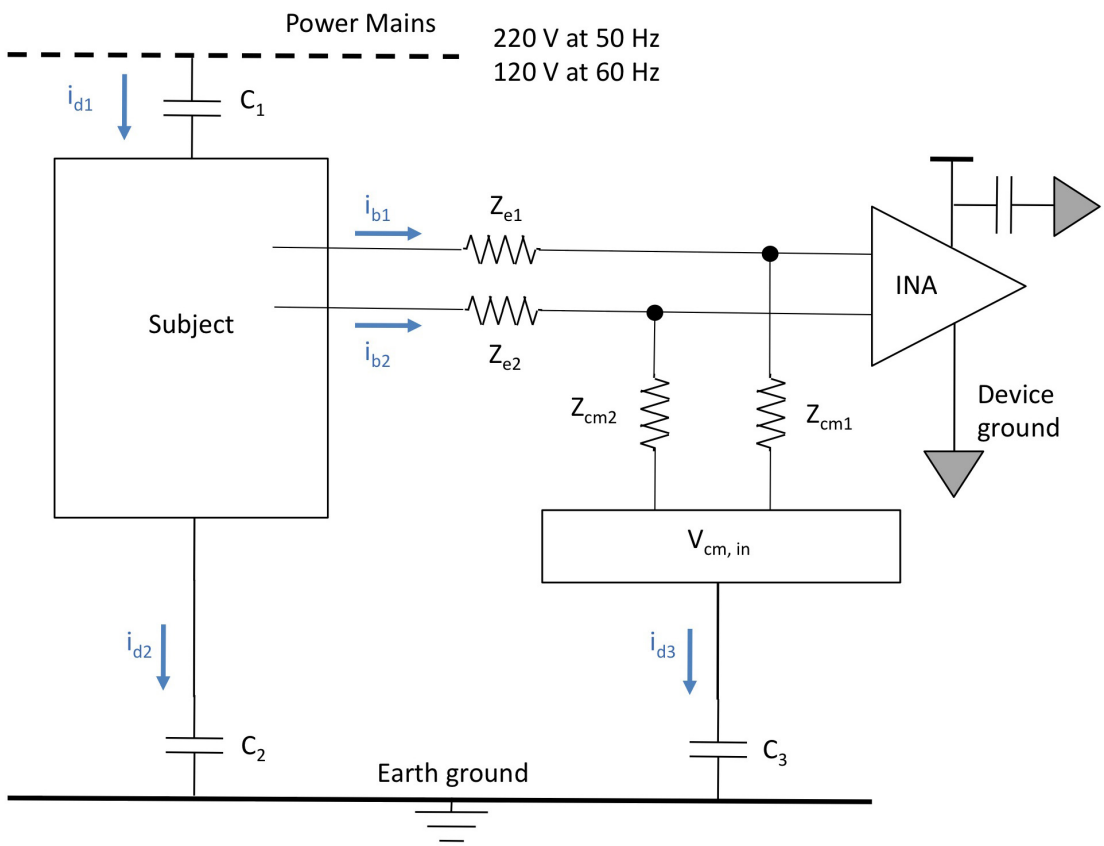

Figure 2.8 Circuit representation of a two electrode ground free biopotential recording system. Noise from main power lines is coupled through C_1 resulting in a current i_{d1}. This current can then flow through the electrodes and be seen by the device, (i_{b1}, i_{b2}, i_{d3}) or flow to the earth ground (i_{d2}). See equations 3.5 and 3.6 for the quantification of the noise.

From equation 2.6, the voltage noise contributions from the common mode impedance can be simulated for various CMRRs (5 kΩ electrode impedance mismatch, i_{d3} = 1 nA, Figure 2.9). In typical instrumentation amplifier settings, it is beneficial to have both a high common mode impedance and differential impedance. Importantly, in a ground free, 2-electrode configuration, the Z_{cm} can increase the noise for a particular CMRR and electrode-tissue impedance mismatch (Figure 2.9). This is not an intuitive result and should be carefully considered. Having an infinite CMRR would minimize the noise, but this is not realistic, especially when size and power are considerations for INA selection. Understanding the minimum noise requirements and potential electrode mismatches defines the CMRR required. Figure 2.10 shows how increasing mismatches in electrode impedances affect the voltage noise (CMRR = 80 dB, i_{d3} = 1 nA). The closed-loop device CMRR can range from 80-100 dB depending on the input filter matching (Figure 2.6). With a 5 kΩ electrode impedance mismatch and 80 dB CMRR, the voltage noise due to power mains coupling is < 3 μV. A 10 kΩ mismatch increases the noise to 5 μV.

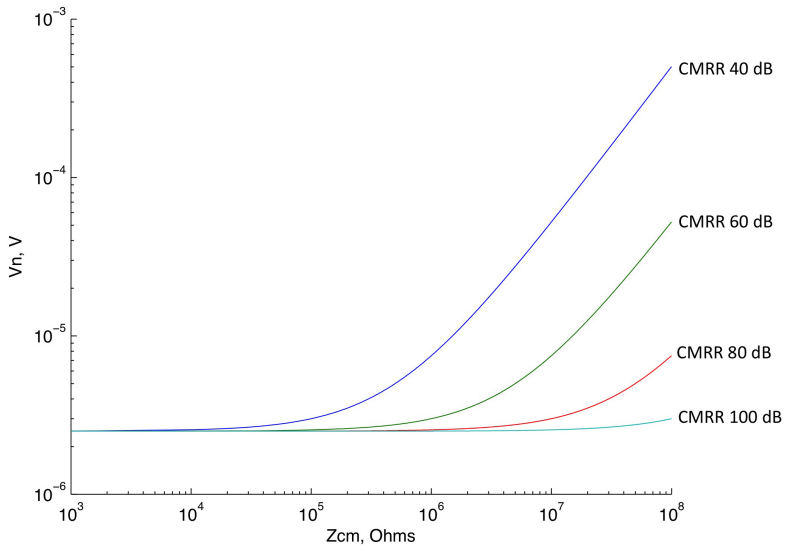

Figure 2.9 Voltage noise versus common mode impedance. Simulation data from equation 2.6. A 5 kΩ electrode impedance mismatch, Z_d, is used. CMRR from 40 to 100 dB are plotted.

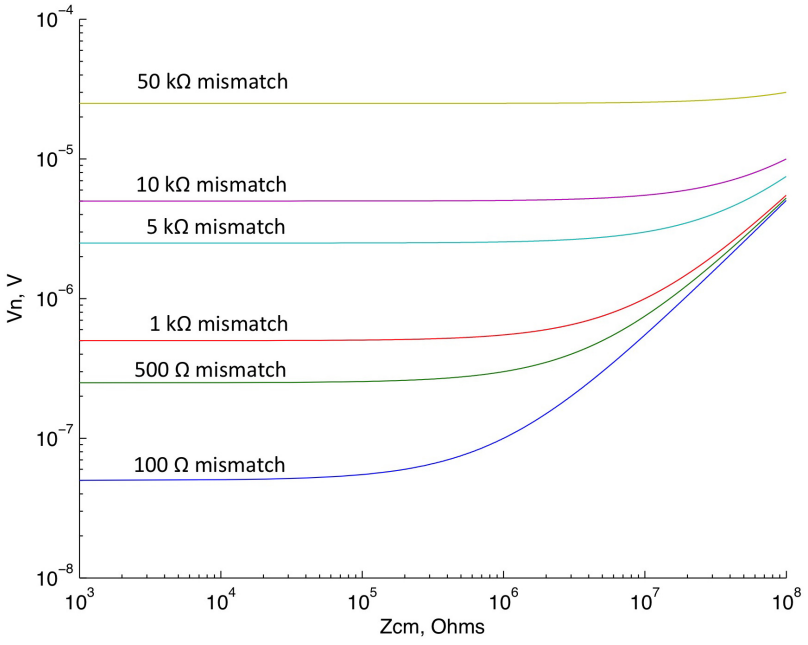

Figure 2.10 Voltage noise versus common mode impedance for various electrode impedance mismatches, Z_d. Simulation data from equation 2.6. 80 dB CMRR is used. Z_d from 100 Ω to 50 kΩ are plotted.

2.3.4 Minimizing Radiofrequency Interference

Radiofrequency wireless powering of devices introduces a planted noise source directed at the implantable device. Amplifiers in particular are susceptible to RF interference at the electrode inputs. If seen by the INA, frequencies in the MHz manifests as DC offsets and slow drifts. This behavior exists because amplifier inputs act as diodes in this frequency range and rectify the AC signal into DC or slow AC waves (188). This can be observed by directly inputting a high frequency differential signal into the INA inputs. To demonstrate, a signal generator is used to input 1, 10 and 20 MHz differential signals into the INA with no input filters and only input common mode bias resistors (Vdd = 3.0, gain = 43 dB (200:1)). Additionally, a reference voltage of 1.5 V was applied to the output through a unity gain buffer. The output voltage should be centered at 1.5 V. Figure 2.11 plots the average output voltage detected by an oscilloscope as the amplitude of the input signal is varied. The output voltage shifts well beyond 1.5 V, and this can result in undesirable drifting of the output signal and amplifier saturation.

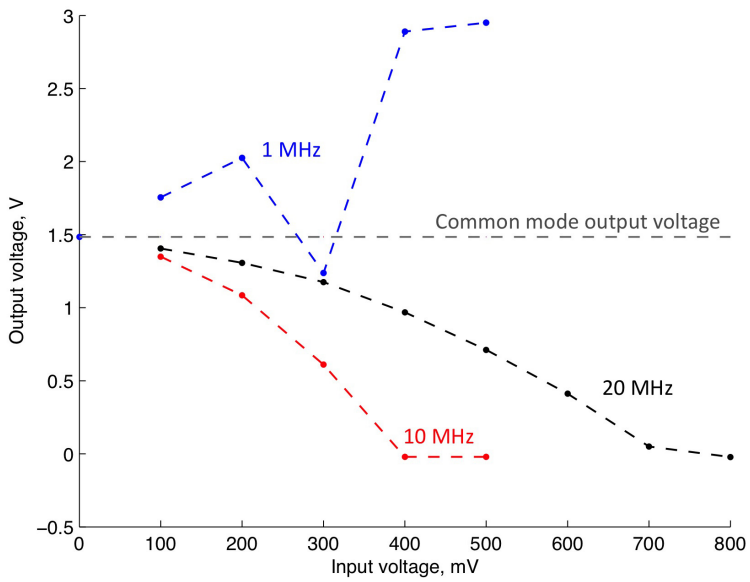

Figure 2.11 DC offsets and slow drifts caused by RF inputs into the INA. A function generator inputs 1 (blue), 10 (red), and 20 (black) MHz signals into the input of an INA with no filtering. The measured output is the average as observed on an oscilloscope. Vdd = 3 V and the output reference voltage is 1.5 V.

To minimize the RF induced drifts, a low pass input filter is inserted using C1, C2, R1, and R2 (Figure 2.5). Due to the potential divider effect, the components must be well matched. Low pass filters require smaller valued components than high pass filters. It is reasonable to find 1% matched COTS passive components with small footprints to prevent CMRR degradation. The benefit of the filter is shown in Figure 2.12. The full analog front end was used for this measurement (Vdd = 1.8 V, Gain = 60 dB). A 1, 4, and 8 MHz differential signal at various amplitudes is applied at the inputs with the signal generator. These frequencies are used since the wireless powering (Chapter 4) is performed at 4 MHz. The common mode output voltage is 0.6 V at 100 mV pk-pk input. For ease of viewing, the common mode output voltage is shifted to 1.6 and 2.6 V for the 500 mV and 1V conditions, respectively. The input filters remove the DC offset and drifting due to the RF input. The 1 MHz signal is noisier as there is less attenuation.

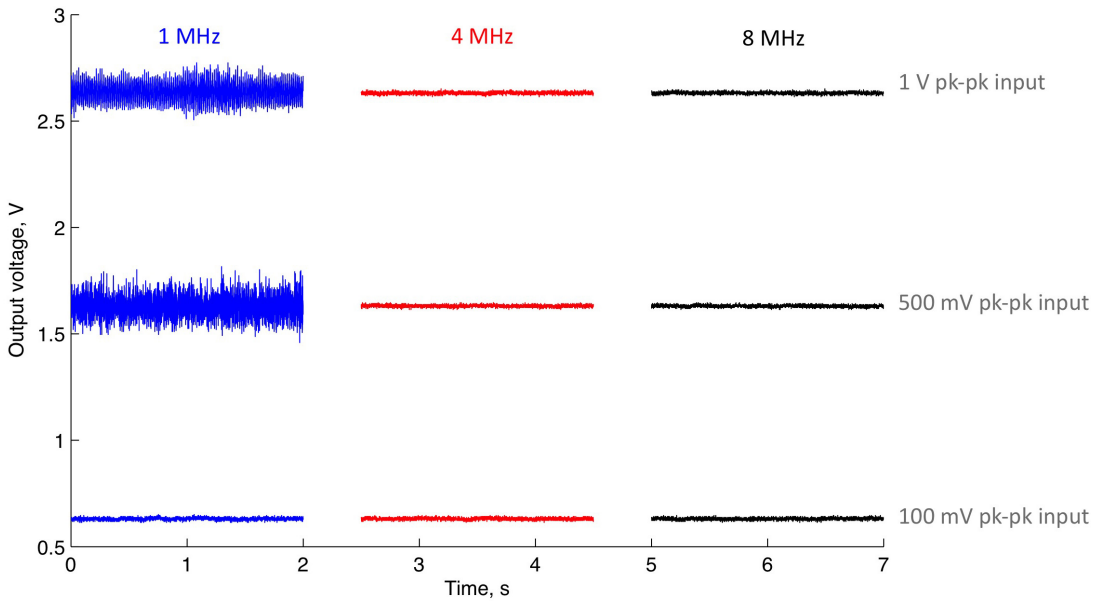

Figure 2.12 Prevention of DC drifting due to RF interference. A low pass filter was inserted into the inputs of the device AFE. A waveform generator is used to pass 100, 500 and 1000 mV pk-pk into the device. The data is digitized and transmitted. The common mode output voltage is 0.6 V, but the results have been level shifted for 500 and 1000 mV pk-pk signals. This was done for ease of viewing. No DC offsets or drifting is observed. Device gain is 60 dB

2.3.5 Input Referred Noise

The smallest signal the AFE can measure is determined by the device's internal noise. Instrumentation amplifiers have an input voltage noise source, output voltage noise source, input current noise source, and other external noise sources (i.e. electrodes or biasing circuitry). The total noise referred to the INA input can be quantified by equations 2.7 and 2.8 (189). The voltage noise source at the input, e_{ni}, is not affected by the gain, G, of the amplifier, while the voltage noise source at the output, e_{no}, is. The current source at the input, i_n, creates noise with respect to the electrode resistance, R_e. Using the INA specification sheet parameters and estimating external noise contributions,

an approximate noise value referred to input is calculated to be 56.92 nV·Hz$^{-1/2}$. Figure 2.13 shows the measured noise at the output of the second stage of analog front end (blue line). The noise referred to input is determined by dividing the total output noise by the gain (black line). At 20 and 200 Hz, the noise referred to input is 68.15 and 49.16 nV·Hz$^{-1/2}$, respectively. Values are well matched to theoretical calculations. To observe the minimum noise seen by the device, the electrode inputs of the device are shorted and the resulting voltage is digitized by the MCU. The baseline oscillates between 2 or 3 bits, indicating signals greater than 14 μV can be observed.

$$V_{n,total} = \sqrt{\left(e_{ni}\right)^2 + \left(\frac{e_{no}^2}{G}\right) + \left(i_n R_e\right)^2 + \left(V_{n,external}\right)^2} \tag{3.7}$$

$$V_{n,resistor} = \sqrt{4 k_B T R} \tag{3.8}$$

Table 2.2 Noise Referred To Input Parameters

Parameter	**Definition**	**Value**
e_{ni} (10 – 1000 Hz)	Voltage noise source at input	50 nV·Hz$^{-1/2}$
e_{no} (G = 10)	Voltage noise at output	200 nV·Hz$^{-1/2}$
I_n (max)	Current noise source at input	100 fA·Hz$^{-1/2}$
$R_{e,i}$ (i = 1,2)	Electrode resistance	10 kΩ
$V_{n,external}$ = resistor thermal noise k_B = Boltzmann's constant T = temperature	Thermal noise	13 nV·Hz$^{-1/2}$ per resistor
$V_{n,total}$	**Total noise**	**56.92 nV·Hz$^{-1/2}$**

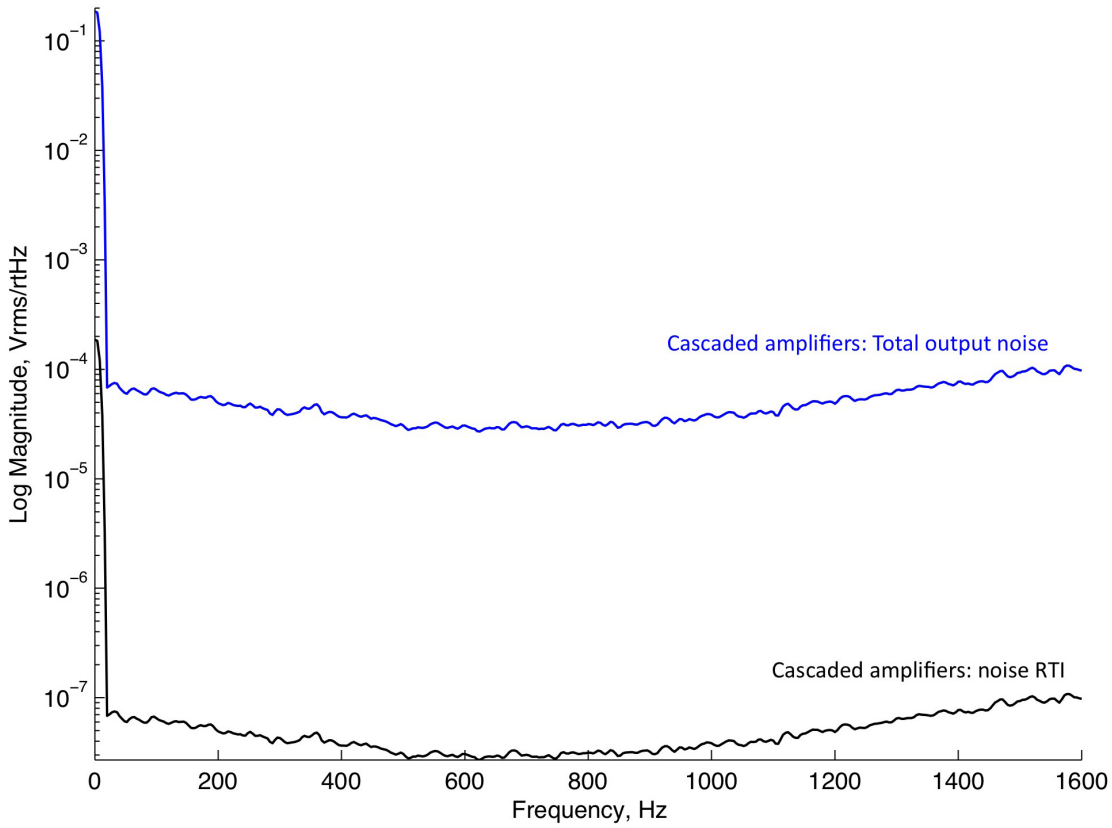

Figure 2.13. Total output noise (blue) and noise referred to input (black) of analog front end. The cascaded amplifier topology is used and noise is measured at the output of the second stage amplifier (input to the ADC). A dynamic signal analyzer is used with 100 sample averages.

2.3.6 Final AFE Specifications

The ADC within the microcontroller performs the digitization of the amplified and conditioned signal. The ADC can operate with 8, 9 or 10-bit resolution and operates with an internal 1.2 V reference. For a fixed gain of 60 dB (1000:1 ratio), the voltage resolution is 4.69 μV, 2.34 μV, and 1.17 μV for 8, 9 and 10-bit resolution, respectively. Typically, the 8-bit resolution is used. If 60 dB of gain and no noise are assumed, the input of the amplifiers require a signal larger than 4.69 μV. The maximum signal that can

be detected before saturating the ADC is 1.2 mV. As the noise floor seen by the device is 2 to 3 bits, detectable signals are greater than 14.07 μV. Thus, the dynamic range is 38.61 dB. The AFE occupies 7 mm x 7 mm of board space, and with telemetry, the area is increased to 7 mm x 14 mm. The device draws 1.8 mA RMS (1.8 V Vdd) which equates to a power consumption of 3.3 mW. The measured specifications of the analog front end can be found in Table 2.3. It is difficult to compare the AFE of this device to other COTS or commercially available devices since several of the product specifications are unreported (Table 2.4). Three important features standout, though. 1) This is the first implantable biopotential telemeter to offer electrical stimulation for closed-loop applications. 2) The size and power consumption are significant advancements from previous devices. When compared to the only non-implantable biopotential telemeter with stimulation (66), the size is reduced from 37 x 26 x 6 mm and 27 x 24 x 6 mm to a 7 x 14 x 3 mm and the weight from 4.44 g to less than 0.7 g (batteries and wireless powering not included). 3) The device presented is not limited by battery life and can be used for chronic applications.

Table 2.3 AFE Measured Specifications

Design Parameter	**Specification**
Input impedance	100 GΩ (from INA333 datasheet)
CMRR	80-100 dB
Low input-referred noise	68.15 $nV \cdot Hz^{-1/2}$ (20 Hz) 49.16 $nV \cdot Hz^{-1/2}$ (200 Hz)
High Gain	60 dB (1000:1)
Input dynamic range	38.61 dB
Size	7 x 14 x 3 mm (includes telemetry)
Power consumption	3.3 mW (5 kHz sampling, 1.8 V Vdd) 33.7 $\mu W/mm^2$

Table 2.4 Comparison of AFE to COTS and Commercial Devices

Device	(64) (TR50BB)	(65) (HD-S21)	(66)	(67)	This work
Number of recording channels	2	1 biopotential , up to 2 pressure	1	7-8 or 14-16	1
HP cutoff, Hz	Not reported	0.1	0.32	4-300	0.72
LP cutoff, Hz	Not reported	145	80	3000	1132
Bandwidth, Hz	Not reported	0.1-145	0.32-80	4-3000	0.72 - 1132
Sampling Rate	Up to 2 kHz	Not reported	200 Hz	20 kHz: 14-16 channels 40 kHz: 7-8 channels	5 kHz
Gain, dB20	Not reported	Not reported	60	54-90	60
Input referred noise	Not reported	Not reported	Not reported	2.2 μV	~2.3 μV
Telemetry	Yes; digital	Yes; digital	Yes; digital	Yes; digital	Yes; digital
Electrical Stimulation channels	None	None	Yes	None	Yes
Device components	COTS	COTS	COTS	COTS	COTS
Implantable?	Yes	Yes	No	No	Yes
Power consumption	Not reported	Not reported	31.8-54 mA	Not reported	3.3 mW
Powering Source	Rechargeable battery; inductive powering	Battery	Battery	Battery	Wireless; magnetic resonance powering
Battery Life, hrs	4-7	2 months	Not reported	1.5	No battery
Size (L x W x H)	28.5 x 24 x 10.5 mm	5.9 cm^3	Neural interface board: 37 x 26 x 6 mm MCU board: 27 x 24 x 6 mm	35 x 35 x 35 mm	7 x 14 x 3 mm
Weight, g	13	8	4.44 (not including battery pack)	22	< 0.7 g (powering board not included)

2.4 Constant Current stimulator

The function of a constant current stimulator is to deliver information to neurons through an electrical stimulus. Critical parameters for stimulators are: charge balanced

waveforms, safety under fault conditions, and controllable parameters (pulse width and amplitude). The stimulator topology is a current sink with switches to control the polarity (Figure 2.14) (190). A blocking capacitor is placed between one electrode and the switch to limit charge injection under fault conditions, maintain charge balance, and block DC currents (191,192). Additional blocking capacitors can be placed at each electrode as a safe practice. MCU timers are used to control the pulse width and frequency of stimulation while a digital to analog converter (DAC) outputs a reference to control the current amplitude.

The stimulator topology maintains a constant current by the feedback to the operational amplifier. When switch A connects the V_{ref} and V_a nodes, the operational amplifier will drive the MOSFET until $V_b = V_a$. Since V_b is equal to V_{sense}, the amplitude of current can be controlled with V_{ref} and is equal to V_{ref} / R_s. Given enough voltage head room to drive the load across the electrodes, the current will be held constant at the desired amplitude. The first generation topology can drive 1.316 mA across a 1.026 kΩ load (Figure 2.15). The MCU control logic of stimulation parameters is shown in Table 2.5. During the initialization, no current is passed. At event 1, the switches are configured to pass current through the electrodes in one polarity and then toggled at event 2 to flip the polarity. At event 3, both electrodes are tied back to V_{drain}.

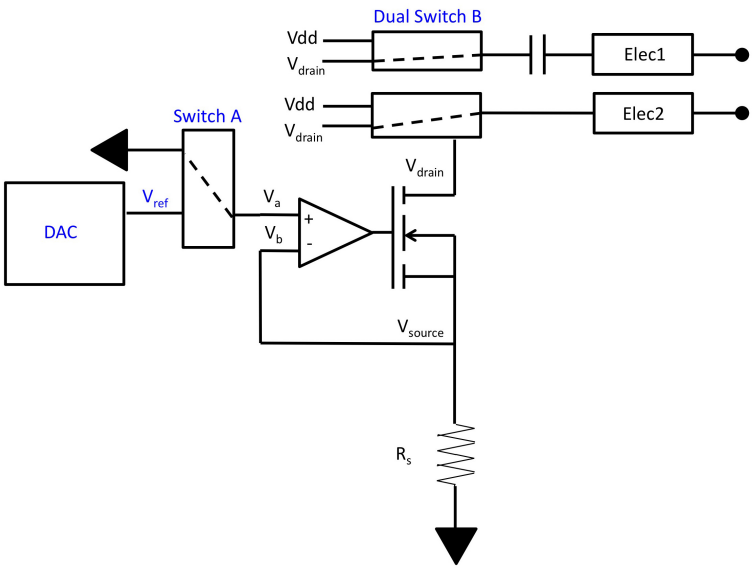

Figure 2.14 Constant current stimulator topology. The opamp wil drive the MOSFET until $V_a = V_b$. Current amplitude can be calculated by dividing V_{ref} by R_s. An additional DC blocking capacitor can be placed on electrode 2. Blue label indicates blocks that are controlled by the MCU. Switch operation is detailed in Table 2.5.

Figure 2.16 demonstrates fast stimulation at 1 kHz with 200 μs pulse widths. The frequency of pulsing is much greater than the typical deep brain stimulation paradigm (100-200 Hz). As some applications require more headroom to pass more current, a 2nd generation stimulator is designed that can handle a 12 V supply. The increased supply voltage provides voltage headroom to pass a minimum of 1 mA through a 10 kΩ load. Figure 2.17 compares the driving capabilities of the 1st and 2nd generation stimulators across a 10 kΩ load. The differential voltage measured in Figure 2.16 and Figure 2.17 were acquired with an oscilloscope probing the voltages at the output of electrode 1 and electrode 2. The two voltages were then subtracted.

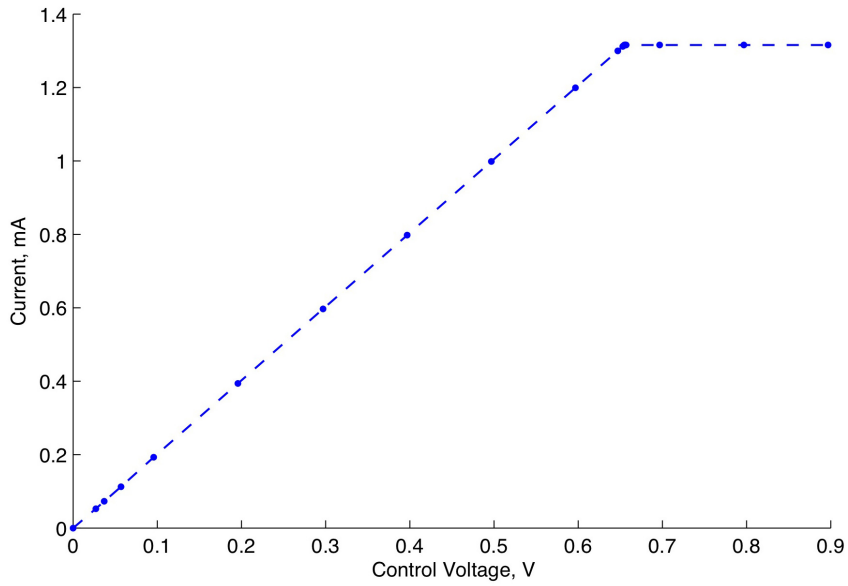

Figure 2.15 Linear control of current of constant current stimulator. R_s = 497.8 Ω, V_{dd} = 2 V, R_{load} = 1.026 k Ω. The current plateau is 1.316 mA.

Table 2.5 Control Logic of Stimulation Parameters

	Initial	**Event 1**	**Event 2**	**Event 3**
Electrode 1	V_{drain}	V_{dd}	V_{drain}	V_{drain}
Electrode 2	V_{drain}	V_{drain}	V_{dd}	V_{drain}
V_a	Gnd	V_{ref}	V_{ref}	Gnd

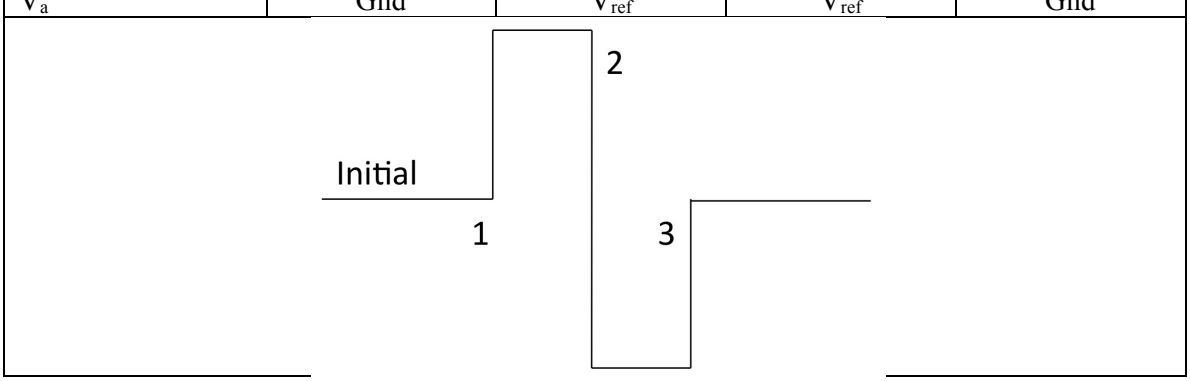

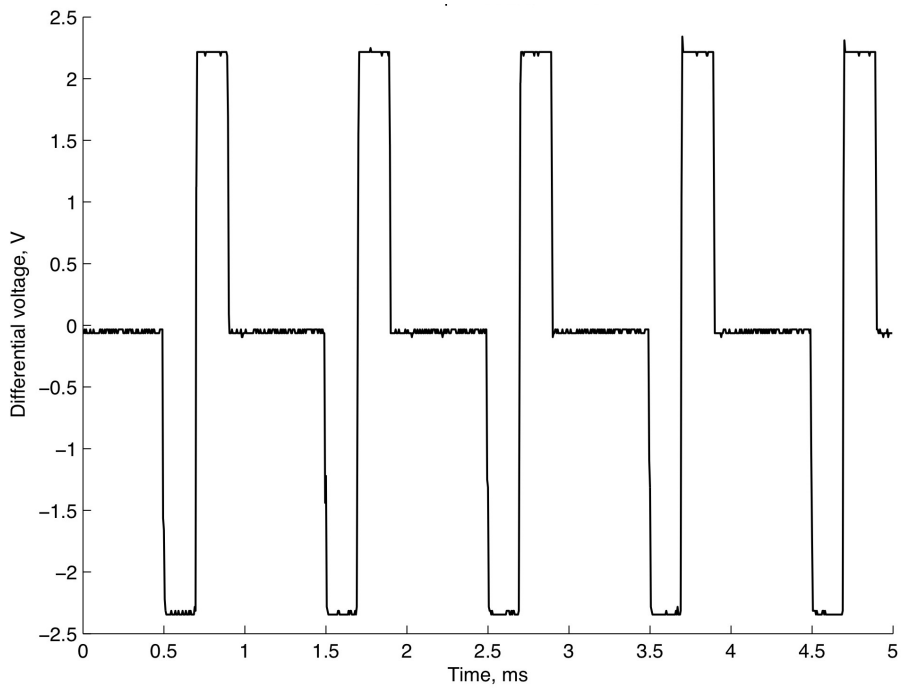

Figure 2.16. Biphasic stimulation pulse train. Stimulation is across a 11 kΩ load. Stimulation parameters are: 200 μA, 200 μs pulse width, 1 kHz period. Differential voltage is the voltage across the load.

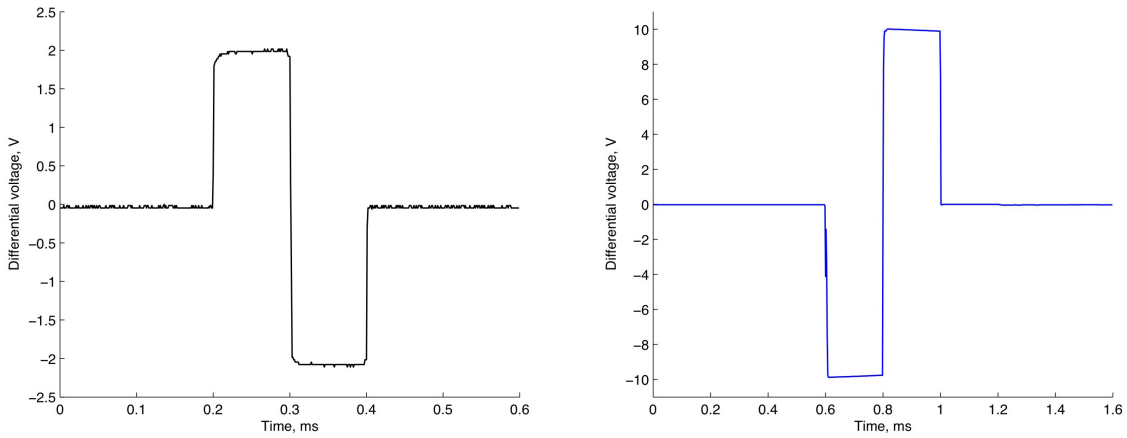

Figure 2.17 Comparison of the 1st generation and 2nd generation constant current stimulators. The first generation stimulator (black, left) is driving a 10 kΩ load with 200 μA (100 μs pulse width). The second generation CCS (blue, right) is driving a 10 kΩ load with 1 mA (200 μs pulse width).

2.4.1 Final Constant Current Stimulator Specifications

The measured specifications of the constant current stimulator are shown in Table 2.6. Programmable features include pulse width, frequency, current amplitude, and duration of stimulation. Experimental DBS protocols range from 1 Hz to 200 Hz stimulation (72-75). The maximum driving current is determined by the load and voltage headroom provided by the stimulator supply voltage (Vdd). As previously discussed in Section 3.3.1, electrode impedances can vary significantly *in vivo*. Clinical DBS macroelectrodes range in impedance values from 500-1500 Ω (193). Microelectrodes, though, can have impedances in the tens of kΩs (182). Increasing the voltage headroom for the 2nd generation stimulator allows experimenters to drive 1 mA across a 10 kΩ load, exceeding the typical drive currents of a few hundred μAs. Table 2.7 compares this work to other COTS implantable stimulators from Table 1.2. For brevity, non-implantable devices are not included. This work meets the specifications of other COTS stimulators, and excels in size and operating lifetime, as it does not rely on batteries. While it does not provide 2 channels of stimulation, this device includes a biopotential acquisition channel for closed-loop operation. It is difficult to compare current driving capacity as loads are not specified in other works. The measured specifications show that the CCS presented in this work is suitable for implantable chronic experiments.

Table 2.6 Final Specifications of the Constant Current Stimulator

Parameter	Condition	Specification
Minimum Pulse width		8 μs
Frequency		1-10 kHz
Stimulation current	R_s = 499 Ω	
V_{dd} = 1.8 V	R_{load} = 1 kΩ	1.2 mA
V_{dd} = 2 V	R_{load} = 1 kΩ	1.3 mA
V_{dd} = 3 V	R_{load} = 1 kΩ	2.0 mA
V_{dd} = 12 V (2nd generation)	R_s = 200 Ω R_{load} = 10 kΩ	1.0 mA
Biphasic Stimulation		Yes
Footprint (L x W x H)		6 x 5.5 x 3 mm

Table 2.7 Comparison of CCS to COTS and Commercial Devices

Device	(81)	(82)	(84)	(78,80)	This Work
Number of stimulating channels	2	1	1	2	1
Biphasic stimulation?	Yes	Yes	Yes	Yes	Yes
Power Supply, V	4.65	5 V compliance	3	3.6	1.8 – 12 V
Programmable?	Yes; not wireless	Yes; inductive powering rectification	Yes; wireless	Yes; tethered	Yes; wireless
Stimulation current, μA	20-100	100-500	50-600	13-1000	120 – 1000 (10 kΩ load)
Stimulation frequency, Hz	131	Not reported; stimulation current rise time is 10 **μs**	131	2-500	1-10000
Pulse width duration, μs	60	50-250	52	0-100% of period	8 μs to 100% of period
Telemetry	No	No	Yes; inductive near field communication	No	Yes; digital radio
Electrical recording channels	None	None	None	None	Yes
On / Off switch	Yes; magnet	Yes; inductive powering	Yes; inductive near field communication	No	Yes; telemetry

Implantable?	Yes	Yes	Yes	Yes	Yes
Power consumption	Not reported	Not reported	Not reported	Not reported	@1.8 V, 90 μW during off periods @12 V, 600 μW during off periods Stimulation power is depending on active current
Powering Source	Battery	Inductive powering	Battery	Rechargeable Battery	Wireless; magnetic resonsance powering
Battery Life	2 months	-	3-5 weeks	10 days	-
Size (L x W x H)	8 mm diameter, 30 mm length	14 x 22 x 6 mm	20 x 38.5 x 13.5 mm	33 x 20 x 8 mm	6 x 5.5 x 3 mm
Weight, g	2.1	2.5	~13	11.5	< 0.7 g (no powering board included)

2.5 Microcontroller and Telemetry

An ARM Cortex-M0 Nordic microcontroller (MCU) acts as the brain of the device. The MCU digitizes the output of the AFE and telemeters the data. The devices are configured with a total sampling rate of 5 kHz. The telemetry is setup to transmit 40 kbps and the MCU can support up to 2 Mbps (194). Similar to the firmware for the optogenetic device (Chapter 3), interrupt based logic is used to maintain low power consumption and sleep states. The fidelity of telemetry with respect to range and orientation of the antenna is an important consideration. By designing at a miniature scale, the manufacturer recommended antenna circuit board layout technique must be modified. To quantify packet loss, the device is placed in three orientations (in line, perpendicular, and standing)

with respect to the basestation (Figure 2.18). The packet loss is measured over 20 second intervals. The packet loss is less than 3% in most orientations and distances and less than 1 % in orientations 1 (in line, blue) and 2 (perpendicular, grey) at a distance of 12 inches. Packet loss is the worst with orientation 1 at 48 inches (12.5% loss) and position 3 (standing) at 24 inches (4.3% loss). To better understand losses in future iterations, the antenna radiation pattern should be measured in an anechoic chamber.

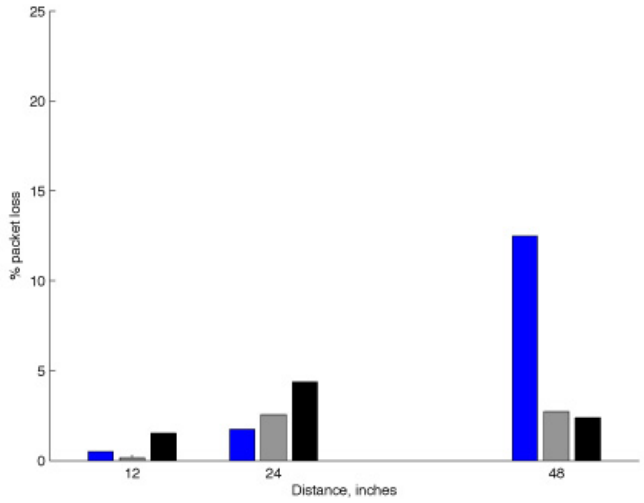

Figure 2.18 Packet loss with respect to distance for 3 device orientations. The device is parallel and inline (blue), perpendicular (grey), or standing (black) with respect to the basestation. Losses were measured at 12, 24 and 48 inches.

2.6 *In vivo* validation

Validation of device blocks *in vivo* is performed acutely and chronically in rats. All procedures were approved by the Purdue Animal Care and Use Committee (PACUC) under protocol 1112000339. For acute experiments, female adult Long-Evans rats were anesthetized with urethane (0.7-1.2 mg/kg, IP) and given butorphanol (0.5-2mg/kg, SC). The relevant biopotentials in this work are: ECG, external intercostal EMG for

respiration rates, LFP, and EEG or ECoG. Subsections of 2.6 will address each biopotential measurement. EEG and ECoG are categorized together as the frequency and amplitude content are similar.

The devices used for validation are a 1st generation device with 1 channel recording and 1 channel stimulation, and a 2nd generation device with 2 channels of recording and 1 channel of stimulation. The 1st generation device is characterized in Sections 2.1-2.5 and will be named device 1 (D1). The 2nd generation device is an extension of this work and will be named device 2 (D2). A DC power supply provides power at 1.8 V for both devices. The bandwidth of D1 is designed for 0.7 Hz to 1 kHz, while the bandwidth for D2 is 8 Hz to 1 kHz. Gain for both devices are set to 60 dB. Both devices are sampled at 2.5 kHz per recording channel. A GRASS amplifier (GA) is used for comparison. Various GA gain and bandwidth settings were used to observe the desired signal of interest. The GA low pass cutoff was always set to 10 kHz and sampled at 20 kHz. For the LFP validation, D2 is used to both stimulate and record to demonstrate both functionalities in the device.

2.6.1 Electrocardiogram *in vivo* Validation

Stainless steel leads are placed intramuscularly the lead 1 configuration (Figure 2.19). After suturing in the leads to prevent displacement, the leads are fed to a connector. The connector is used to exchange input connections between the GA, D1, and D2. Simultaneous measurements are not made to prevent undesired loading between amplifiers. Figure 3.19 compares the lead 1 ECG recording between the GA, D1, and D2. The order in which data was acquired is D1, GA, and then D2. Figure 3.19 compares the

3 acquisition systems for a 7 second recording (left) and a 1 second recording (right). The P wave, QRS complex, and T wave are all distinctly visible in all 3 recordings. The QRS distortion (M shaped-wave and lower amplitude) seen in the GA recording is caused by the 60 Hz input notch filter and can be avoided in future experiments by switching off the filter. In the 7 second D2 recording, a slow ~0.5 Hz oscillation is observed. This is a motion artifact associated with the breathing rate of the subject. Due to D1's lower highpass filter, this signal is seen in D1 and not D2. Interestingly, the heart rate decreases from D1, to GA, to D2, which is the order of recording. In 7 seconds, the number of heartbeats is 25, 21, and 19 for D1, GA, and D2, respectively. While urethane anesthesia should maintain steady cardiopulmonary physiology (195), cardiac depression has been previously observed (196). D1 and D2 are both suitable for ECG acquisition *in vivo*.

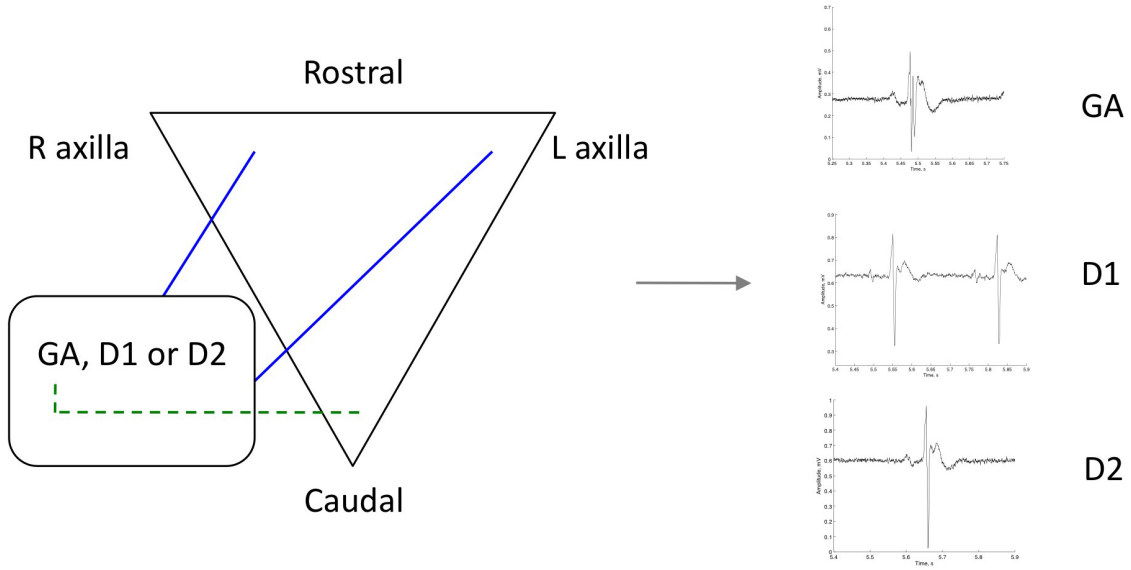

Figure 2.19 ECG Lead 1 Measurement Setup. The GRASS amplified (GA) uses 3 electrodes. Two differential (blue) and a common mode (green) electrode. Device 1 (D1) and Device 2 (D2) only use the differential electrodes.

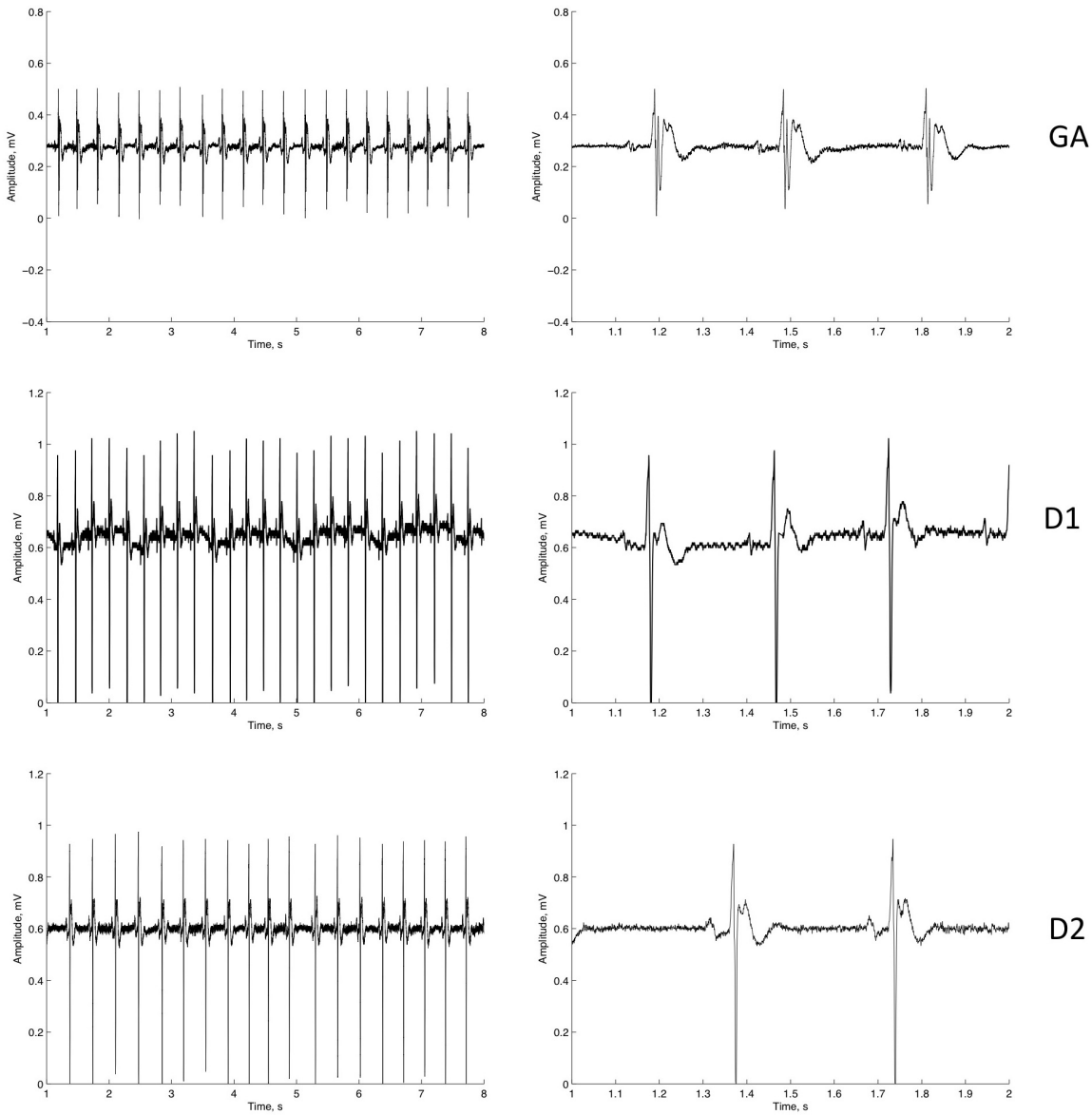

Figure 2.20 Comparison Between Acquisition Systems. Lead 1 recordings from a GRASS amplifier (GA), Device 1 (D1), and Device 2 (D2). 7 second recordings are pictured on the left and 1 second recordings on the right. Leads are sutured intramuscularly and switched between amplifier systems. The order of recordings is D1, GA, D2.

2.6.2 Electromyogram *in vivo* Validation

Respiration rate activity can be observed by measuring the EMG of the external intercostal muscles (49,197). Stainless steel leads are placed intramuscularly in the right external intercostals. The same connector setup for ECG validation is used (Section 2.6.1). Figure 2.21 shows EMG and ECG recordings at the mid-thoracic right external intercostal muscle. The order of recording was GA, D1, and then D2. The GA's high pass was increased to 10 Hz to eliminate motion artifacts that are visible in the raw D1 trace (blue). No digital filtering was required on the GA. D1 and D2 have noisier recordings and are both high passed at 100 Hz with a digital second order butterworth filter. Raw traces for D1 and D2 are shown in blue, and post filtering is in black. The high pass filter drops the signal common mode to 0 V. The signal quality of the GA is superior. The common mode electrode of the GA provides increased noise rejection. However, the EMG signature is still observable by D1 and D2. From this data, it can be seen that respiration is occurring at approximately 1 Hz.

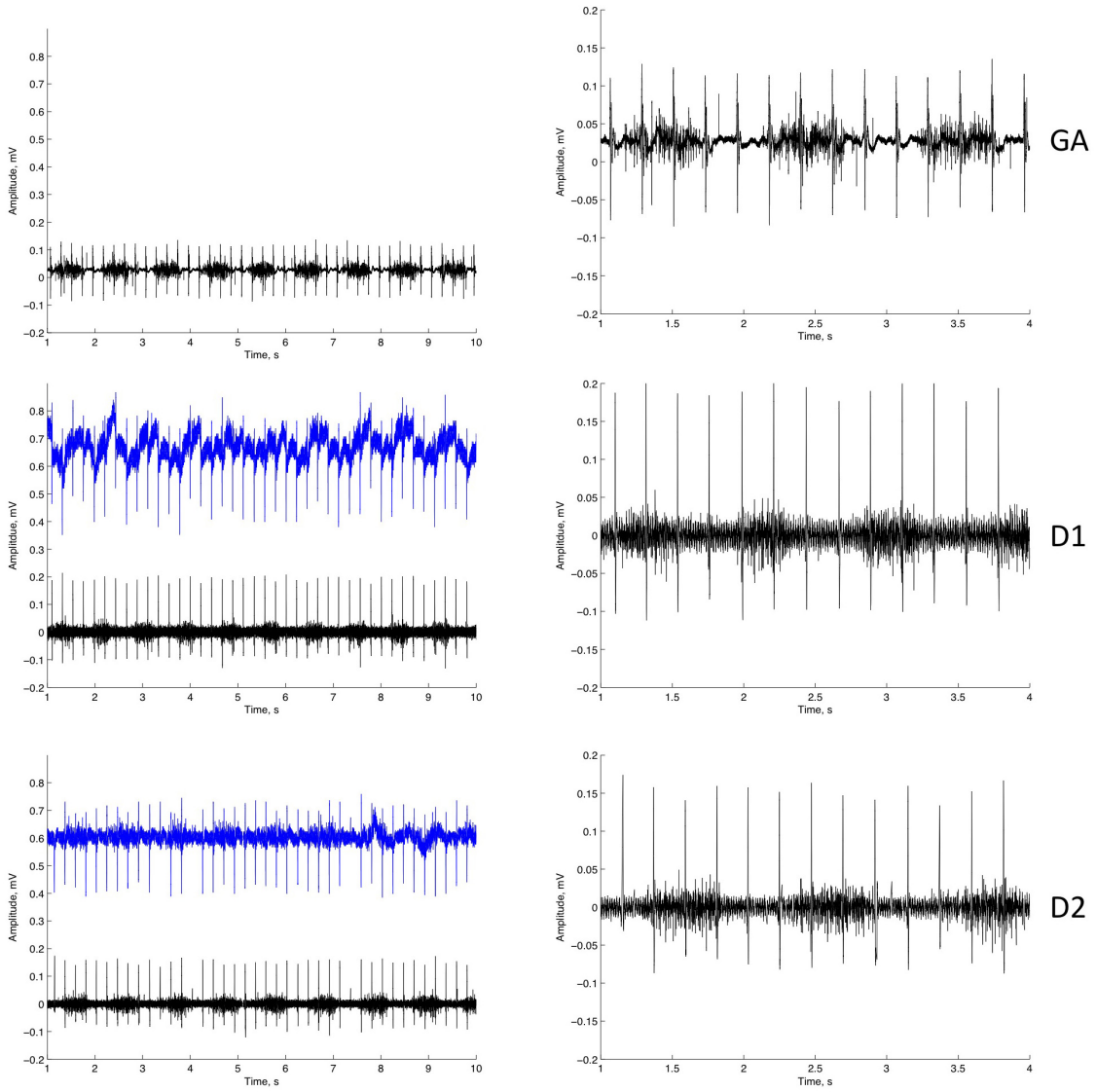

Figure 2.21 External intercostal EMG's recorded by the grass amplifier (GA), device 1(D1) and device (D2). For D1 and D2, the blue signals are raw and the black signals are high pass filtered at 100 Hz. The high amplitude spikes are QRS complexes. The left figures show 9 seconds of data while the right displays only 3. The EMG activity can be detected with all three measurement systems.

2.6.3 ECoG Evoked Potentials *in vivo* Validation

To observe cortical neural activity, the EEG or ECoG is often used. Cortical evoked potentials can be observed if an upstream portion of the neural network is

electrically stimulated. Evoked potentials have been used to map pathways in epileptic patients (198), and the method is used here to elicit cortical activity for observation. The cingulate cortex is a downstream site of the classic Papez circuit (199) and should be activated by stimulation at the fimbria or fornix. In this validation experiment, a stainless steel bipolar twisted pair of recording electrodes is placed at the surface of the left cingulated cortex (AP: 1 mm, L(left): 0.5 mm, DV: -1 mm from skull surface; bregma reference). A bipolar stainless steel bipolar twisted pair for stimulation is targeted at the fimbria-ventral hippocampal commissure white matter tracts (AP: -1.3, L(left): 0.2 mm DV: -4.5 mm from brain surface; bregma reference). A commercial stimulator was used to activate the fimbria-ventral hippocampal commissural axons (3 Hz stimulation, 200 μA, 200 μs pulse width). Figure 2.22 compares the evoked potentials at the surface of the left cingulated cortex. The recording progression was GA, D1, and then D2. The D2 recording had a large amount of 60 Hz noise. As a result, a digital IIR notch filter was used. The raw data is shown in blue and the filtered signal in black. It seems that larger evoked potentials are observed in D1 and D2 when compared to GA. Figure 2.23 shows each evoked potential from a trial aligned and then averaged (thicker black line). It is clear that the GA plot has a lower amplitude. It is possible that as the GA was used first for recording, sufficient time had not passed to recruit neurons for a larger response. In all 3 recording systems, evoked potentials can be seen 3 ms after the stimulation artifact (aligned at 10 ms, Figure 2.23). In D1 and D2, a valley is seen at 15 ms after the stimulation artifact, and then second peak at 30 ms (Figure 2.23, overlay, red and blue). The recordings in D1 and D2 are in good agreement; however, it is unclear why the GA

response is different. As evoked responses can be experimentally difficult to maintain, future setups should simultaneously record the same signal.

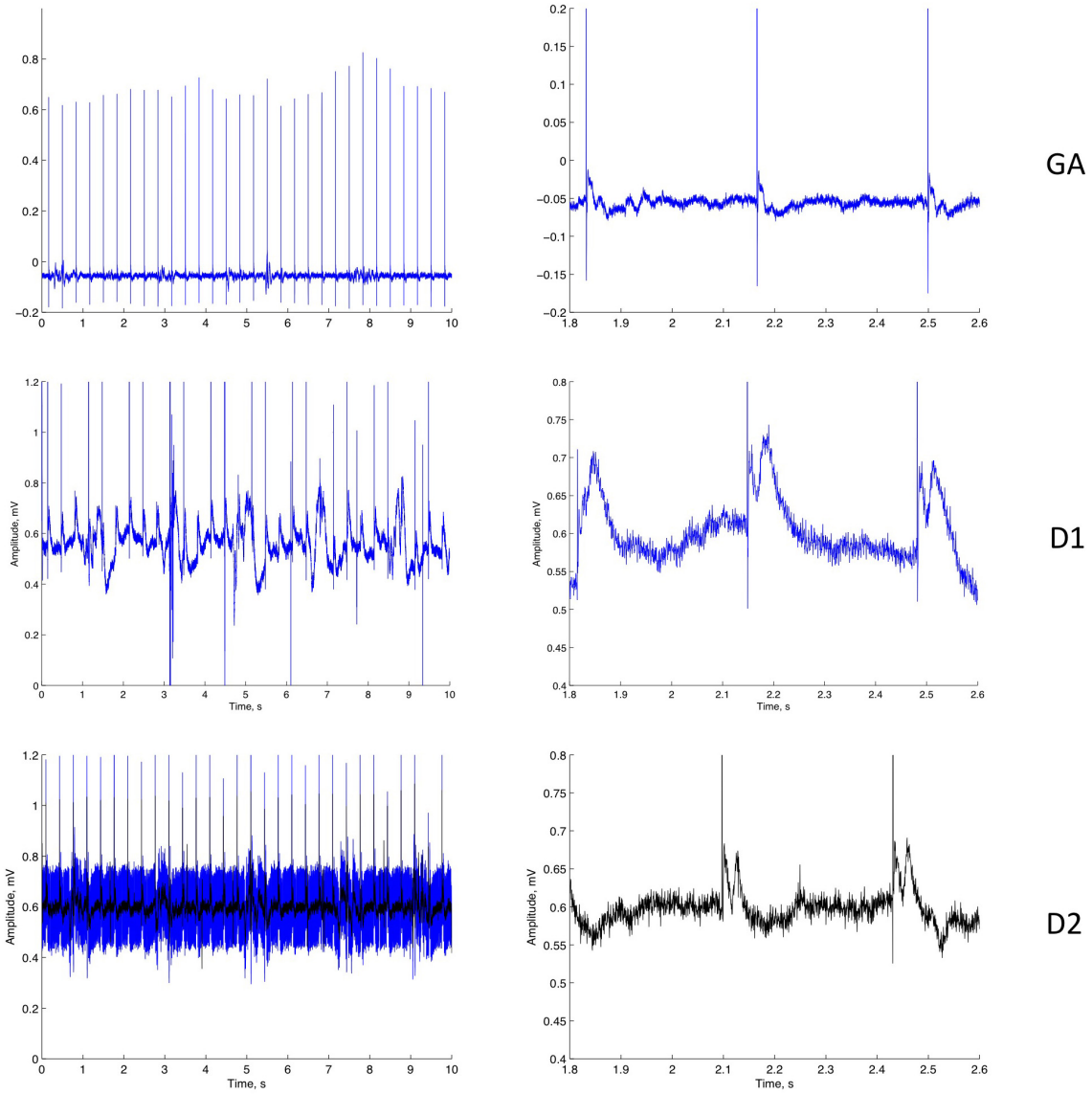

Figure 2.22 Evoked potentials recorded by the grass amplifier (GA), Device 1(D1) and Device 2 (D2). Electrodes were placed at the surface of the left cingulated cortex. A commercial stimulator was used to activate the fimbria-ventral hippocampal commissural axons (3 Hz stimulation, 200 μA, 200 μs pulse width). The left figures show 10 seconds of data while the right only 0.8 seconds. The blue traces are raw data in all three figures. D2 required a 60 Hz digital notch filter.

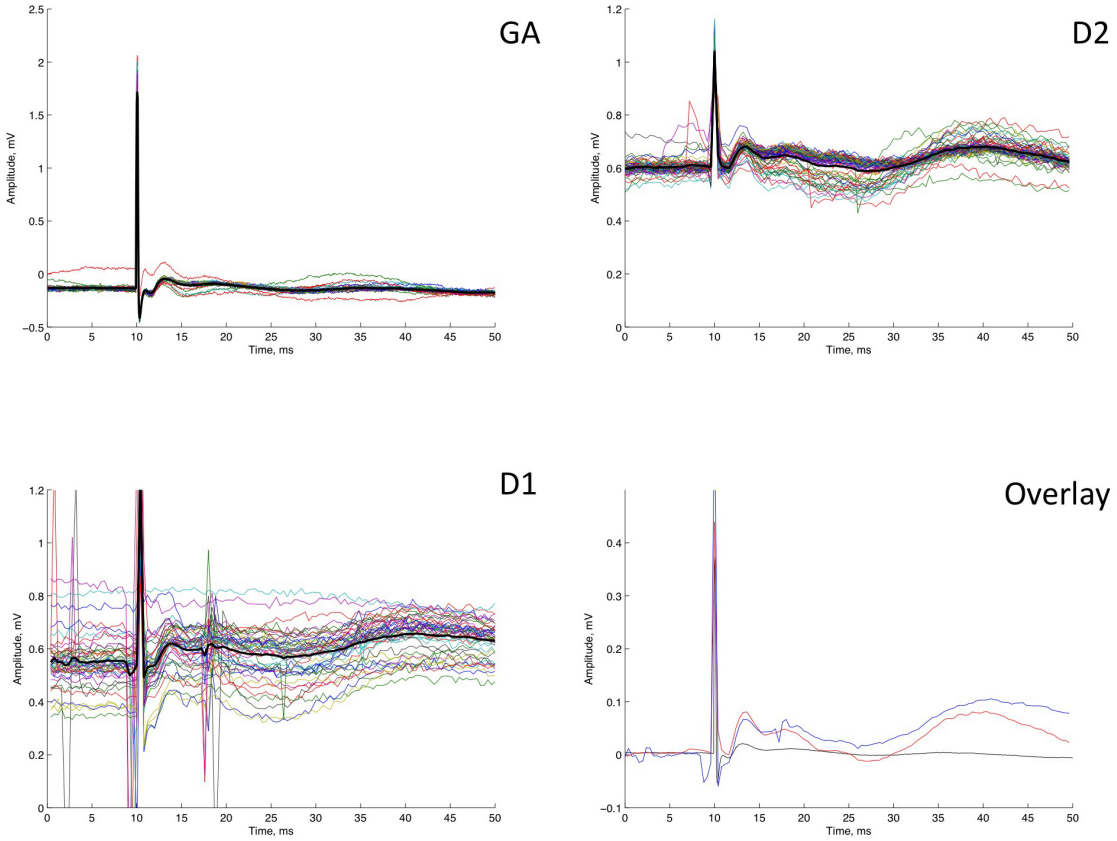

Figure 2.23 Averaged evoked potentials from Figure 2.22. Evoked potentials were aligned and averaged. The GA is recorded first, then D1 and then D2. Bottom right overlays the averages for each recording system (GA = black, D1 = blue, D2 = red).

2.6.4 LFP Evoked Potential *in vivo* Validation

The local field potential can be observed using depth electrodes. Using a similar setup to Section 2.6.3, evoked potentials are recorded at the ventral hippocampus (AP: -5.2 mm, L(right): 4.5 mm, DV: -5.5 mm from brain surface; bregma reference). Stimulation is at fimbra-ventral hippocampal commissural axons (same as Section 2.6.3). In this validation, Device 2 is used to both stimulate (200 μA, 200 μs pulse width) the axons and record the evoked response. Figure 2.24 shows overlapped and averaged

evoked potentials recorded at the right ventral hippocampus. The data is notch filtered to reduce 60 Hz noise. Each color represents one evoked potential and the thicker black trace is the average response. The peak is 30 ms after end of stimulation. The D2 stimulation caused the amplifier to saturate and any earlier peaks are missed. This data shows that the 2nd generation stimulator can deliver sufficient current to the tissue, and that the same device can record the response shortly after.

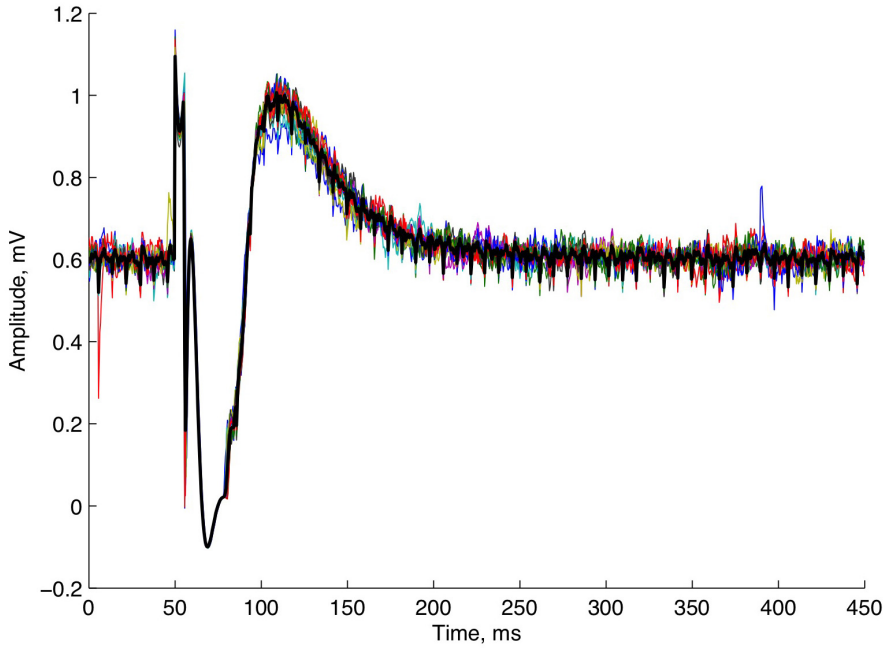

Figure 2.24 Evoked response recorded using only D2. The fimbria ventral hippocampal commissural axons are stimulated. The response is recorded in the right ventral hippocampus. The data is notch filtered to reduce 60 Hz noise. The peak is 30 ms after end of stimulation.

2.6.5 Multichannel Chronic *in vivo* Validation

The closed-loop device can be redesigned into a 2-channel biopotential device. Two of these devices (Device A and Device B) are used to collect chronic data from a rat

for preliminary experiments in SUDEP. A RF wireless powering board is mounted next to Device A (Figure 2.25). The power board has a coil receiver that couples energy from a larger source coil. The RF energy coupled is rectified into a DC source. Capacitors (not shown in Figure 2.25) smooth the voltage, and a 1.8 V linear dropout (LDO) regulator provides a stable power supply to both Device A and Device B. The powering board and Device A are implanted on the rat's flank and leads are routed subcutaneous and sutured intramuscularly in lead I and lead II ECG configurations. Device B is routed subcutaneous to the skull and measures LFP from the left ventral hippocampus and ECoG from the contralateral motor cortex. Twisted pair platinum electrodes are used for the LFP and stainless steel bone screws for the ECoG. The transmit powering coil is a single solenoid wrapped around a cage. An example dataset is shown in Figure 2.26. This experiment was performed in collaboration with Professor John Jefferys at the University of Oxford. In Figure 2.26, it is clearly shown that 2 implantable devices can simultaneously acquire 4 channels of biopotentials. This is crucial for experiments in SUDEP as correlating seizure activity to respiratory and cardiac abnormalities is a key goal.

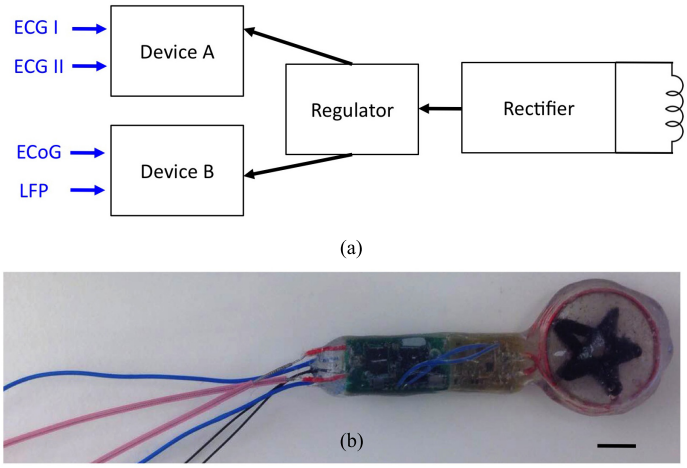

Figure 2.25 Fully Implantable Device for Multichannel Biopotential Acquisition. a) The RF wireless powering receiver circuitry consists of an inductor antenna fed to a rectifier. The rectifier converts the RF signal is converted to a DC voltage. Capacitors (not shown) buffer the rectifier output and a single 1.8 V regulator creates a stable supply for Device A and Device 2. Device 1 acquires 2 lead configurations of ECG and Device B acquires ventral hippocampal LFP and ECoG from the contralateral motor cortex. b) Image of the powering circuitry tied to a Device 1. The star marks the coil receiver. The green board is Device 1 and the yellow board is the powering circuitry. The black wires provide power to Device 2 (not pictured). The coil is 15 mm in diameter. The black bar is 5 mm.

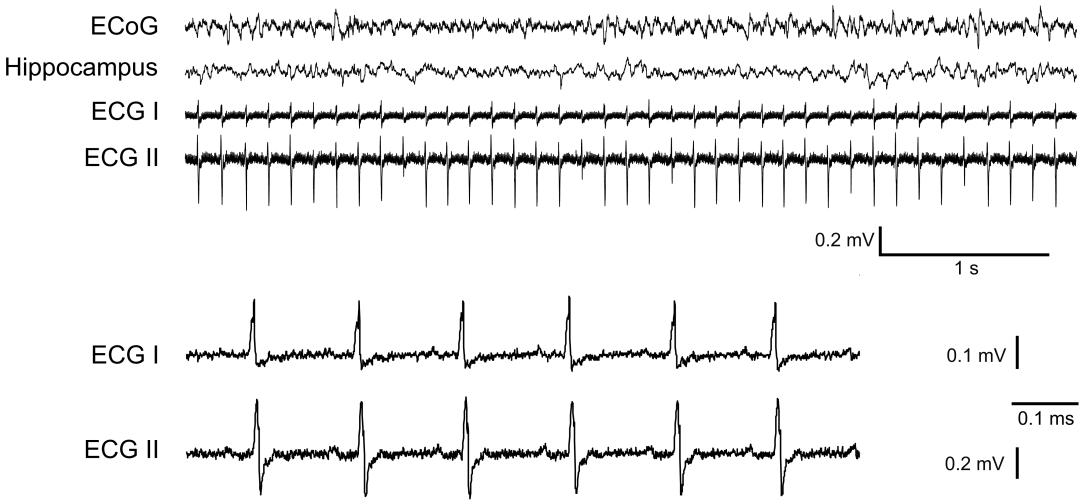

Figure 2.26 Chronic *in vivo* Validation of Multichannel Biopotential Acquisition. 4 channels of biopotentials are simultaneously acquired from 2 implanted devices. Clear ECG, ECoG, and LFP activity can be observed.

2.7 Pressure Monitoring for Urinary Urge Incontinence

Urinary incontinence is the inability to control the bladder. Previously, it has been shown acutely that the bladder can be controlled by deep brain stimulation in the periacqueductal grey (PAG) area in both rats and humans (174). Before pursuing chronic human studies, chronic animal validation studies are required. The proposed closed-loop system would measure bladder pressure and stimulate based upon a threshold to prevent urination. As a proof-of-concept experiment, a device development board was reconfigured to operate with a Bremen capacitive pressure sensor. When pressure is exerted on the membrane of the sensor, the distance between the end plates is reduced. This results in a detectable change in capacitance. For the experiment, the capacitive pressure sensor and development board are used to monitor acute changes in bladder pressure in an anesthetized rat. The Bremen pressure sensor (now owned by Protron Mikrotechnik) and measurement IC are provided by the manufacturer. For integration into the device platform discussed in previous sections, the packaged sensor and measurement IC can communicate to the Nordic MCU with already available general purpose digital input output pins. Figure 2.27 shows the surgical setup. An infusion pump delivers saline into the bladder at a rate of 6 mL/ hr. A reference sensor and the capacitive sensor are measuring pressure from a T piece of tubing. A GRASS amplifier monitors the EMG of the external urethral sphincter and the experimenter visually monitors the urine output. The urine output is recorded with a clicker and the entire voltage pulse indicates urine output from start to finish. Figure 2.28 shows the experimental data. First, both sensors are shown to be linear in the 0-40 mm Hg pressure range. The capacitive sensor is noisy and smoothing function is used (Figure 2.28b, blue = raw, black = smoothed

data). As can be seen, the smoothed data shows the features of the raw data. As saline is infused, the pressure in the bladder increases. A critical threshold is reached and then the EUS activates and urination occurs. The data from the experiment is in good agreement with previous animal experiments (174). The platform is able to detect this reliably and integration into a device form for closed-loop control of urinary incontinence is possible with the presented technologies.

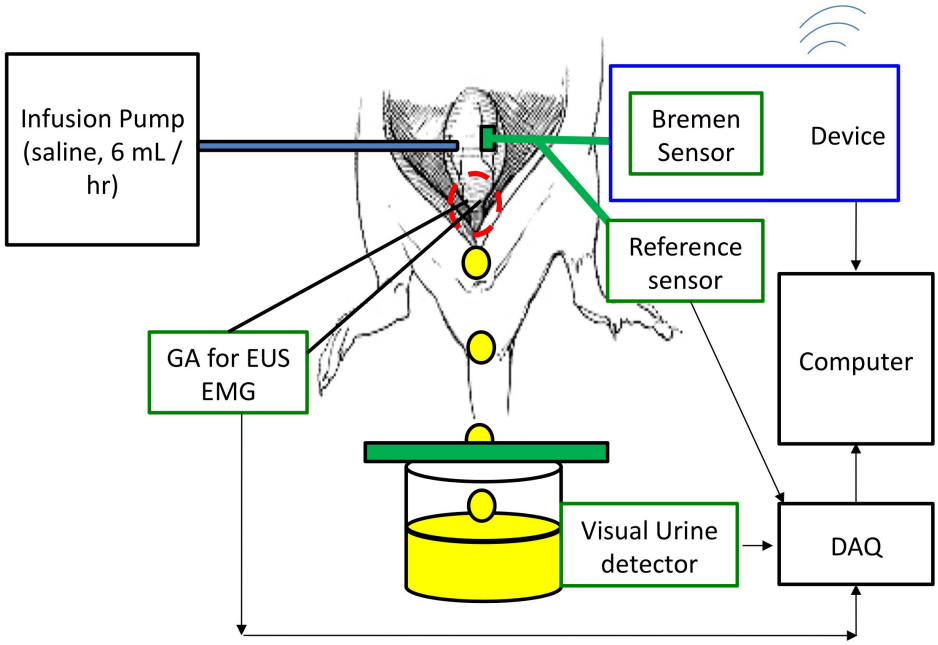

Figure 2.27 Surgical setup of the *in vivo* experiment. The Bremen sensor is connected to the device (development board). A tube runs from the bladder to the sensor and is air filled at the base to prevent fluid entry into the device. The same tube is split to a reference sensor. The device samples at 54 Hz and wirelessly transmits the data to the basestation. The reference sensor is sampled at 500 Hz by the data acquisition unit (DAQ). A grass amplifier sampled at 500 Hz measures the EMG from the external urethral sphincter, and a visual detection is used to mark periods of urination. An infusion pump steadily flows saline into the bladder at a flow rate of 6 mL/hr.

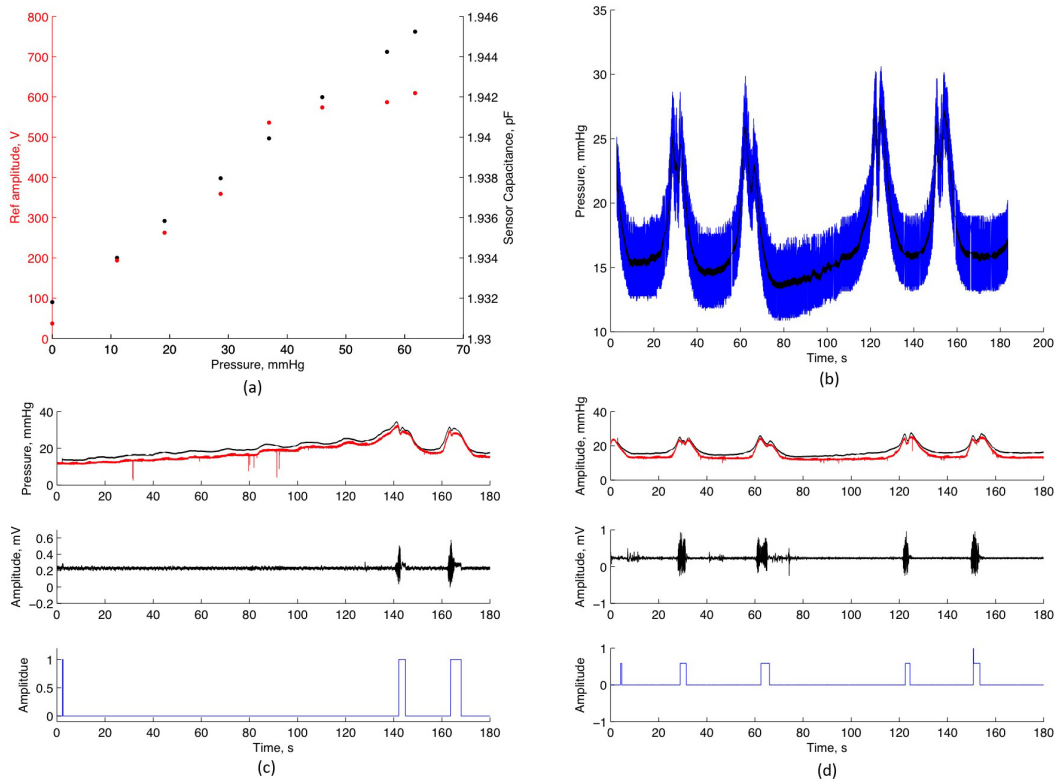

Figure 2.28 Pressure sensing *in vivo* validation. a) Air chamber calibration data for a capacitive sensor (black) and reference sensor (red). The pressure was increased with a custom manometer. Capacitive sensor data points are 20 point averages and were measured by a LCR meter (Agilent) with 1 MHz, 1V excitation. b) *In vivo* pressure measurements with the capacitive sensor require smoothing. The blue trace is raw data sampled at 54 Hz. The black trace is a moving average with a 54-sample window. The smoothed data agrees with the raw data trends. c) A trial observing an empty bladder slowly fill and increase in pressure until urination is observed. d) A trial observing the bladder continually urinate. *In vivo* bladder pressure from the reference sensor (red) and capacitive sensor (black) are in good agreement in both (c) and (d). The pressure drops as urination occurs and the external urethral sphincter activates. The pulse width of the urine markers (blue) indicates the total time of urination. The first mark is the beginning of the trial. EMG data is collected with a grass amplifier sampled at 500 Hz.

2.8 Conclusion

The platform technologies for sensing of electrical signals and providing electrical stimulation have been verified on the bench and validated *in vivo*. The technologies

create a useful and flexible platform for researchers to investigate wide ranging neurological and psychiatric diseases in rodent models. For use in epilepsy, optimization of closed-loop electrical stimulation to increase efficacy and understanding the important features needed in seizure suppression is of great need. To the author's knowledge, the first implantable device with 1 channel biopotential acquisition and 1 channel stimulation is presented. In SUDEP, preliminary experiments show that with two devices, 4 channels of biopotentials can be simultaneously acquired chronically. This experiment paradigm can help to address mechanistic questions involving sudden death. For urinary urge incontinence, pressure sensing *in vivo* is demonstrated acutely. Integration of the sensor into the device for chronic implementation is the next step in creating a closed-loop device to control mictruition.

The individual building blocks of the analog front end, constant current stimulator and microcontroller are modularly integrated into a family of 1st generation devices. With slight modifications to the circuitry to reduce size and share resources, other device systems can be designed for specific applications. Additionally, the optical stimulator for use optogenetics (Chapter 3) can be driven with the CCS. A wireless, closed-loop optical stimulator for use in optogenetics would be of great use to the research community. Table 2.8 lists a family of devices based on the core technologies presented and the possible applications. Applications in blue have been studied or are currently under study with these devices.

Table 2.8 Family of Devices and Possible Applications

Device	**Features**	**Programmable Parameters**	**Possible Applications**
Closed Loop Deep Brain Stimulator **(DBS-CL)**	• Biphasic Electrical stimulation • 1-2 differential recording channels • On board MCU	• Current per phase of stimulation • Frequency of stimulation • Duty cycle of stimulation • Duration of stimulation • Feedback algorithms • Feature detection algorithms on the MCU	• **Parkinson's disease** • **Epilepsy** • **SUDEP** • **Vagal nerve stimulation (VNS)** • **Autonomous neural control (ANC)** • **Addiction** • **Urinary Incontinence** • Social behavior • Anxiety • Autism • Fear • Depression • Sleep/wake cycles • Memory •
Closed Loop Optogenetic Stimulator **(OGS-CL)**	• LED based stimulation • 1-2 channels, differential recording channels • On board MCU	• Stimulating current amplitude • Frequency of stimulation • Duty cycle of stimulation • Duration of stimulation • Feedback algorithms • Feature detection	
Open loop DBS (**OL-DBS)**	• Biphasic electrical stimulation	• Same as DBS-CL but without feedback or feature detection	
Open loop optogenetic stimulator **(OL-OGS)**	• LED based stimulation	• Same as OGS-CL but without feedback or feature detection	
Recording only	• 1-2 channels differential recording • Tie two devices together for 4 channels		

CHAPTER 3. A MINIATURE, FIBER-COUPLED, WIRELESS DEEP-BRAIN OPTOGENETIC STIMULATOR

The data and work in this chapter is accepted for publication in the IEEE Transaction of Neural Systems and Rehabilitation Engineering (PMID: 25608307) . The citation can be found in the CV. This chapter is primarily a reproduction of the publication and has been reformatted for the dissertation © 2015 IEEE (200). This work was performed in collaboration with Dr. Simon John and Dr. Da-Ting Lin at The Jackson Laboratory.

3.1 Introduction

Optogenetics is a powerful core methodology for dissecting neural circuits (201). Pairing of miniature and wireless optoelectronic systems can enhance the rapidly expanding optogenetic (202) and electroceutical (203) toolboxes. In this work, a novel optogenetic stimulator (OGS) is presented for use in rodents. This is a lightweight, miniature, expandable, power efficient, wireless and low cost device to offer control of stimulation parameters with demonstrated deep brain targeting in rodents. Pairing of this technology to a biopotential acquisition device (Chapter 2) would allow closed-loop deep brain optical stimulation. The stimulator is expected to allow many experiments that are not currently practical. Section 3.2 details the modular hardware blocks. Section 3.3 describes the *in vivo* validation with transgenic mice in a conditioned place preference

behavioral test. Section 3.4 follows with a brief discussion, and Sections 3.5-3.7 focus on the materials and methods. The novel contributions from this work are:

1) A new, low profile fiber coupling technique
2) A wireless platform technology for deep brain optical stimulation
3) One of the earliest demonstrations of behavioral modification in mice due to wireless deep brain optical stimulation with optogenetics

3.2 The Optogenetic Stimulator

The OGS is a modular solution (3 modules: optical, control, and power) that consists of a cranially mounted fiber-coupled LED, an ultralow power microcontroller (MCU) to control stimulation protocols, a wireless link to trigger stimulation, and rechargeable solid-state batteries (Figure 3.1a).

3.2.1 The Optical Module

Targeting of deep brain structures is essential to the study of behavior (112,204) and disease (e.g. Parkinsonian circuitry (201) and epilepsy (85,115)). The optical module achieves this by coupling an optical fiber (core diameter = 200 μm; numerical aperture = 0.39) to an LED (Figure 3.1c,d). Since optical throughput is limited by the relatively narrow acceptance angle (numerical aperture) and small surface area of the optical fiber, previous tethered LED fiber-coupled strategies had poor coupling efficiencies and required a driving current of 1.0 A for 27 mW/mm^2 irradiance (465-485 nm) (99). With the presented fabrication methods, the same irradiance level can be achieved while providing 21.01 mA of current to the LED (~50-fold current reduction, Figure 3.3a). This

irradiance level readily activates channelrhodopsin-2 (requires 1 mW/mm^2 of 473 nm light (8)).

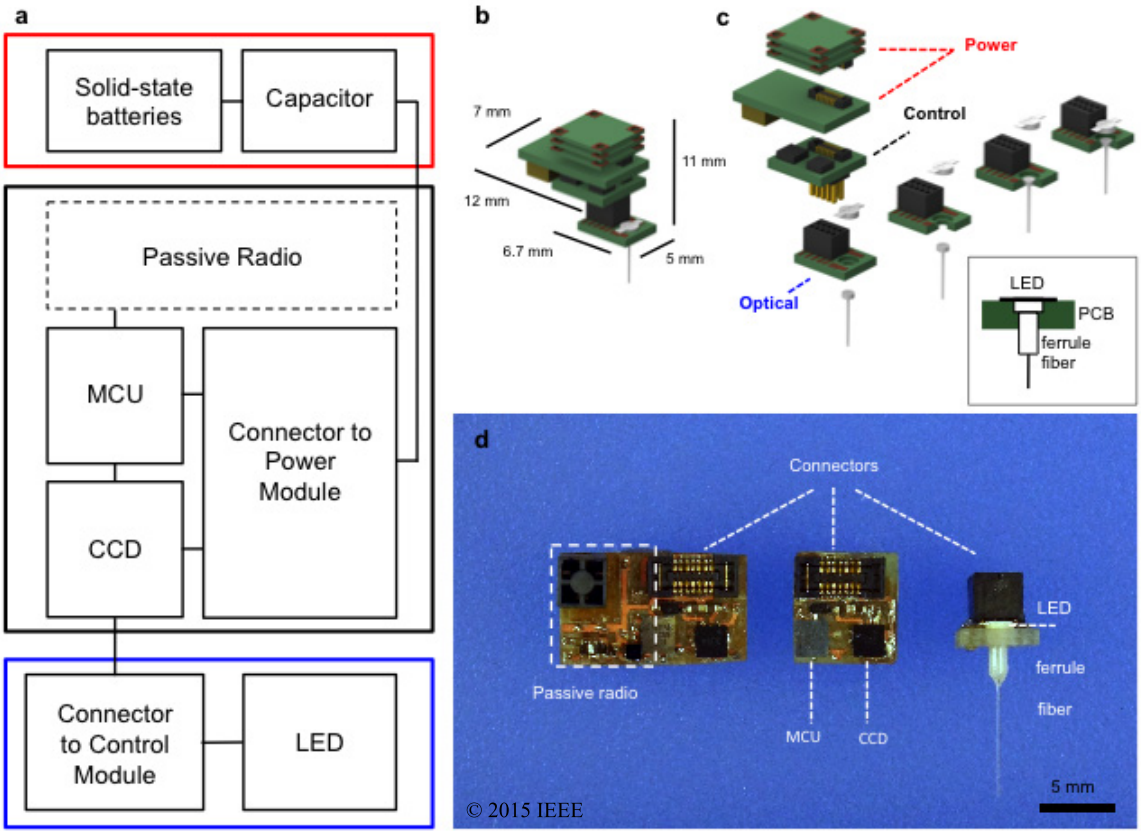

Figure 3.1 The optogenetic stimulator (OGS) modules and full system. a) Block diagram of the OGS. The Passive radio (dashed line) can be removed if not needed. Solid-state batteries in parallel with a capacitor is used to provide continuous power. A MCU and current driver are used to control the LED stimulation protocol. Red = power module, black = control module, blue = optical module. b) A rendering of the OGS fully connected. c) Connecting the 3 modules: power, control, and optical. The optical module is depicted with corner cut away to show the coupling of the LED to fiber-ferrule. Inset is a cross sectional perspective of the optical module. d) Control modules for wireless (left) and internal triggering (middle). Since the internally triggered device does not require a passive radio, the antenna and rectifier are removed from the device. This makes the control module even smaller. The optical module (right) with a fiber-ferrule directly coupled to a LED. MCU = microcontroller. CCD = constant current driver. For alternative module configurations, see Figure 3.2. Side view of wireless control module is provided in Figure 3.2a.

LEDs are used due to the form factor, narrow emission spectrum, rapid rise time (nanoseconds), consistent light output, lifetime, and safety. Since the surface area ratio of the fiber to LED package is < 1, the most efficient optical coupling is achieved by directly butting the fiber to the light source (205). This is realized with a modified fiber-ferrule approach. A circularly packaged, reverse mounted LED is embedded in a printed circuit board (PCB) and a shaved ferrule is mounted through the opposing side (Figure 3.1c). This novel module is fabricated with two concentric through holes of differing depths (1.5 mm and 0.75 mm) and diameters (1.25 mm and 2.00 mm, respectively) to align and hold the fiber and LED. Temperature at the bottom (ventral) surface of the optical modules adjacent to the optical fiber only increased by ≤ 0.80 ^{o}C under different conditions that are far more exacting than those used in the *in vivo* validation experiments below (Figure 3.3d, e), and temperature changes at the skull would be considerably less. To the author's knowledge, this is the first cranially mounted optical module with LED-fiber coupling to allow power efficient, tether free, deep brain targeting.

3.2.2 The Control Module

Controllable optical stimulation enables more sophisticated stimulation protocols. It allows desired setting of various frequencies, pulse widths, irradiances, and patterns. The control module is designed for user programmability of stimulation algorithms and management of power consumption. An ARM Cortex-M0 MCU is interfaced with a constant current LED driver to offer control over the frequency (Figure 3.3b), pulse width (Figure 3.3c), and optical irradiance of stimulation. The optical and temporal parameters can be defined with microwatt and sub-millisecond resolution, respectively. Since the

optical output power is linearly proportional to the input driving current to the LED (Figure 3.3a), the digitally programmable constant current driver (14 steps from 1.8 – 20.0 mA) predictably controls the optical irradiance emitted from the optical fiber. During periods with no stimulation, the device turns off all unneeded MCU peripherals and enters a deep sleep state consuming less than 7 μA (3.3 V supply, < 23.1 μW). Within a stimulation train, the MCU is awake during stimulation and is in sleep for the remainder of the period. Deep sleep wake up times are dependent on MCU configurations (0.056 – 7.0 ms; see NXP Application Note AN11027). Internal MCU timers or an external wireless trigger from the passive radiofrequency receiver (Figure 3.2a) can wake the MCU from deep sleep for stimulation. Using the internal timers, *in vivo* validation was performed with looping algorithms for periodic trains of stimulation (deep sleep wake up time = 7.0 ms).

3.2.3 The Power Module

Ultra-low power consumption and low duty cycle operation open avenues for a variety of powering strategies. Previous optogenetic device studies have used RF radiative far field powering (42), inductive powering (40) or coin cell batteries (39) individually. Here, a more robust technology for behavioral experimental paradigms is used: rechargeable solid-state batteries that are non-cytotoxic, lightweight and thin (Cymbet Corporation). Two 50 μA-Hr batteries were stacked in parallel to provide current to the device. A tantalum capacitor delivers the surge currents required during the 1 s stimulation train. The capacitor is recharged during deep sleep states (no stimulation periods).

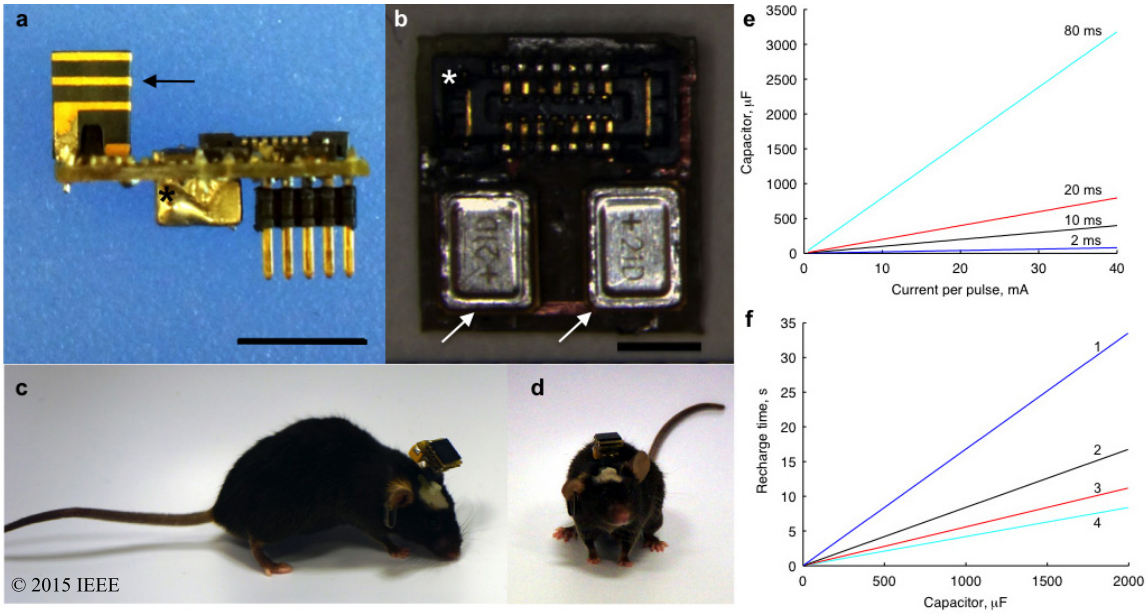

Figure 3.2 OGS modularity allows various configurations. a) 2.4 GHz monopole antenna (black arrow) used with a rectifier and comparator to trigger the MCU. This is a side view of wireless control module shown in Figure 3.1d. Additional ceramic capacitors (black asterisk) are placed next to the bottom connector. b) Supercapacitor modification for the power module. Two supercapacitors (14 mF, white arrows) stacked in series. This module can be used in certain experiments if more charge needs to be delivered than the tantalum capacitor can provide. White asterisk = Power connector. c, d) Optional surface mount package, 8mm x 8mm) used instead of bare die (5.7mm x 6.1mm). The surface mount package is slightly larger but easier to fabricate (see Figure 4.3f for comparison to bare die package). e) Plot of capacitor values versus pulse current at various pulse widths. Blue = 2 ms, black = 10 ms, red = 20 ms, aqua = 80 ms. f) Recharge time required specific capacitor values with various numbers of batteries, Recharge voltage = 4.1 V. Blue = 1 battery, black = 2 batteries, red = 3 batteries, aqua = 4 batteries. Scale bars a = 5 mm; b = 2 mm.

Capacitor sizing can be designed for a single or train of current pulses. This is critical in providing the proper current and stimulation frequency (Figure 3.3e, f). Designing for a 1 s train of 4 ms pulses (10 mA, 20 Hz), a single continuous pulse of 80 ms as a worst case is assumed (see Section 3.5.3). The within train pulse rate is limited by the MCU wake up time and not the capacitor. The minimum capacitor was 795 μF and 1 mF was used. With two batteries, ~8.4 s are required for recharge between trains (Figure 3.2f), and 59 s was

provided. Additionally, recharge occurs between pulses. The batteries provide allow closed experimental setups that are not RF compatible can be used. Miniature and lightweight systems are critical for use in rodents to allow freely moving behavior. When completely connected, the OGS configuration used for *in vivo* validation is 12 x 7 x 11 mm^3 (L x W x H) and weighs <1.6 g. The mice are freely moving and unrestricted (Figure 3.3f, g).

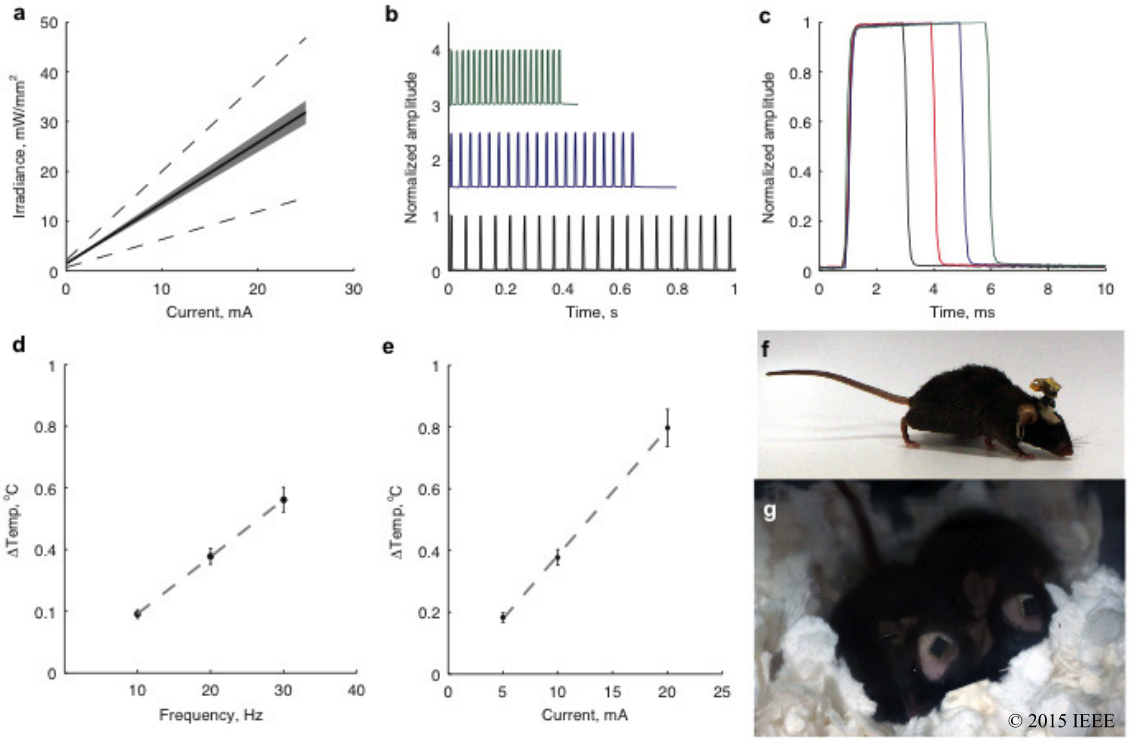

Figure 3.3 OGS characterization for control of stimulation parameters. a) Irradiance of optical modules (n = 41) with respect to input current. Solid black line = average, grey shading = 95% confidence intervals, dotted lines = maximum and minimum. Measurements made with PM100D (Thorlabs) power meter. b) Controlling stimulation frequencies with the microcontroller (MCU) and constant current driver (CCD). Normalized amplitude is the analog response of the power meter from an uncoupled LED connected to the control module. Green = 50 Hz, blue = 30 Hz, black = 20 Hz. 20 pulses each. c) Controlling pulse widths with the MCU and CCD. Each trace is a single pulse at 20 Hz. Black = 2 ms, red = 3 ms, blue = 4 ms, green = 5 ms. d, e) heating from bottom surface of optical modules (n = 5) after 3 minutes of constant stimulation (d: 10 ms pulse

width, 20 mA; e: 20 Hz, 10 ms pulse widths). Measurements were made at room temperature (22-24 ^{o}C). Dotted lines are least square regressions. Error bars are standard errors. f) OGS used for *in vivo* validation on freely behaving mouse. Since wireless triggering was not needed, the smaller internal triggering control module was used, g) Mice can be grouped housed.

3.3 *In Vivo* Validation

Device validation *in vivo* was performed using a well-validated three chamber conditioned place preference (CPP) paradigm (112,206). Mice were generated that express ChR2-H134R and *tdTomato* in dopaminergic neurons after activation by *Slc6a3*-cre (Figures 4.4-5). *Slc6a3-Cre*$^{+}$ mice (treatment groups) and *Slc6a3-Cre*$^{-}$ mice (no ChR2 expression, control groups) were implanted with optical fibers in the right ventral tegmental area (VTA; coordinates AP: -3.44, L: 0.5, DV: -4.1) (Fig. 3.3.1). Phasic, burst stimulation in this region is established to cause place preference (42,112). Mice were conditioned over 3 days. The control and power modules were first connected and then plugged into the optical module immediately prior to the conditioning sessions. Stimulation (20 pulses, 20 Hz, 2-4 ms pulse width, 5-10 mA, 1 minute period) was provided only in the afternoon. While input current controls the optical irradiance, the optical dose is also dependent on the pulse width and is described as output energy per pulse (optical power multiplied by the pulse width). The OGS was programmed to achieve a specific range of doses (Figure 3.6a). At various irradiances, pulse widths from 1 to 1000 ms have been shown to elicit action potentials (8) and drive behavior (38,42,112). We tested the ability to drive place preference with two groups (treatment group 1, Tx1, lower dose range and 2, Tx2, higher dose range). Only the higher dose range Tx2 showed a significant increase in change of preference (one-way ANOVA, $F_{3,18}$

= 13.3983, p = 0.00008, Tx2 significantly different to all other groups with Tukey-Kramer post-hoc, $\alpha = 0.01$) and significantly greater post-test preference ($F_{3,18} = 9.2681$, p = 0.0006, Tukey-Kramer post-hoc, $\alpha = 0.05$) (Figure 3.6c, d). Critically, in treatment groups, the post-test preference for the conditioned chamber increased with dose (Figure 3.6f), and activity levels were not significantly different between groups ($F_{3,18} = 1.2971$, p = 0.3059) (Figure 3.6b) or between the pretest and post-test (Figure 3.7). These results are consistent with previous tethered optogenetic CPP experiments (42,112).

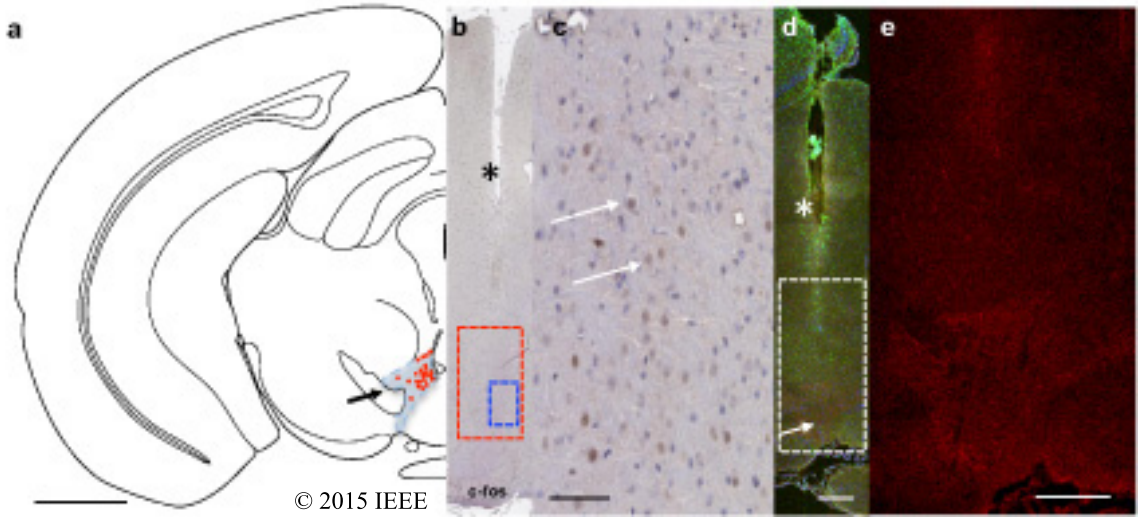

Figure 3.4 Histological characterization of optical fiber implants. a) Optical fiber placement at the right ventral tegmental area (VTA). The black arrow points to the VTA (shaded blue) and the red circles show the placements of individual optical fibers. b) histological characterization with c-fos staining for neurological activity after 1 hour of the CPP stimulation protocol (20 Hz, 10 mA, 4 ms, 20 pulses per minute). The black asterisk indicates the optical fiber lesion tract. Red box indicates the implant site (VTA). Blue box indicates enlarged view in c. c) Enlarged view of blue box in b. White arrows point to c-fos positive neurons indicating recent neural activity. Bar = 50 µm. d) Confocal image of IBA1 (green) and tdTomato (red). As is typical for implantations, IBAI shows mild microglial activation immediately adjacent to the fiber lesion tract (brighter green). As expected following *Slc6a3-cre* activation, the tdTomato is localized at the VTA (white arrow). White asterisk indicates fiber lesion. e) Enlarged view of white box in d showing Slc6a3 activated tdTomato. For further histological characterization of B6.SJL-

(*CAG COP4*H134R/TdTomato*); *Slc6a3*-cre mice, see Figure 3.5. Scale bars a,b 1mm; c, 250 µm; d, 200 µm; e, 500 µm.

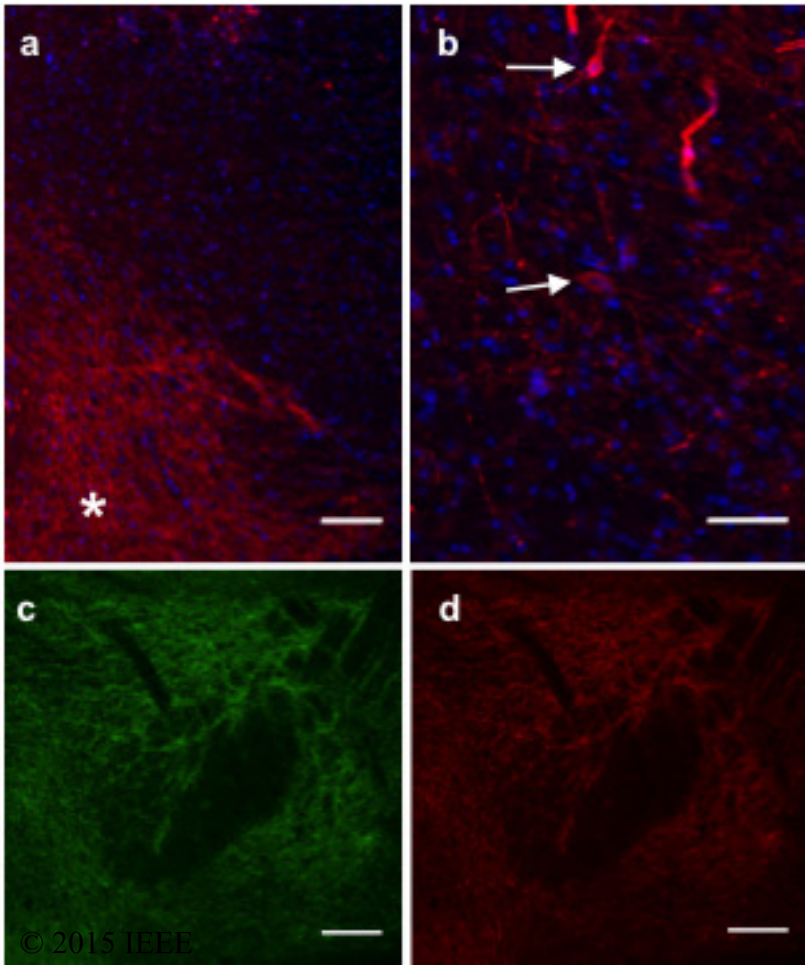

Figure 3.5 Histological characterization of B6.SJL-(*CAG COP4*H134R/TdTomato*);*Slc6a3*-cre mice**.** a) tdTomato (Red*)* expressed in axon tracts (white asterisk). b) tdTomato expressed in soma (white arrows) and dendrites. c) DAT, dopamine transporter, antibody labeling (green) in the VTA. d) Slc6a3-cre activated tdTomato (red) in the VTA. This overlays with DAT in c to infer expression of ChR2-H134R in dopamine producing neurons. Scale bars a = 100 µm; b = 50 µm; c, d = 200 µm.

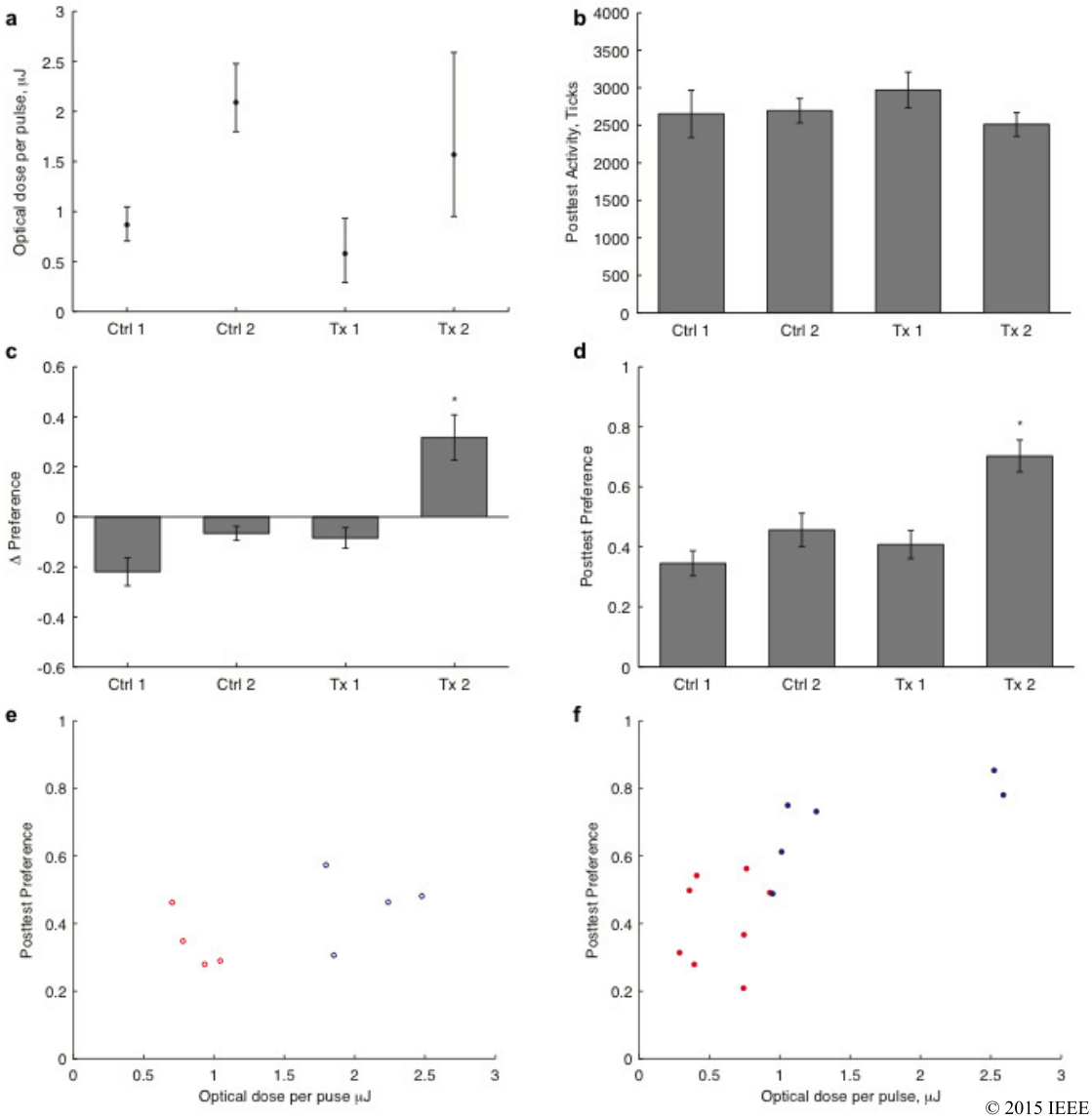

Figure 3.6 Dose dependent induction of conditioned place preference. a) Optical dose range and mean for each group (n = 4-8 per group). b) Posttest activity. There was no difference between groups (one-way ANOVA, $F_{3,18} = 1.2971$, $p = 0.3059$). c) Change (posttest – pretest) in preference towards conditioned side. Tx2 preference change was significantly different to all other groups (one-way ANOVA, $F_{3,18} = 13.3983$, $p = 0.00008$, Tukey-Kramer post-hoc, $\alpha = 0.01$). All other groups were not significantly different from each other (TK post-hoc, $\alpha = 0.01$ and 0.05). d) Posttest preference. Tx2 preference was significantly different to all other groups ($F_{3,18} = 9.2681$, $p = 0.0006$, TK post-hoc, $\alpha = 0.01$ for Ctrl1 and Tx1, $\alpha = 0.05$ for Ctrl 2). All other groups were not significantly different from each other (TK post-hoc, $\alpha = 0.01$ and 0.05). e) Posttest preferences versus optical dose for all control groups. Red open circles = Ctrl 1, blue open circles = Ctrl 2. f) Posttest preferences versus optical dose for all treatment groups. Red closed circles = Tx

1, blue closed circles = Tx 2. All error bars show standard errors unless indicated otherwise. *Indicates significance across all groups.

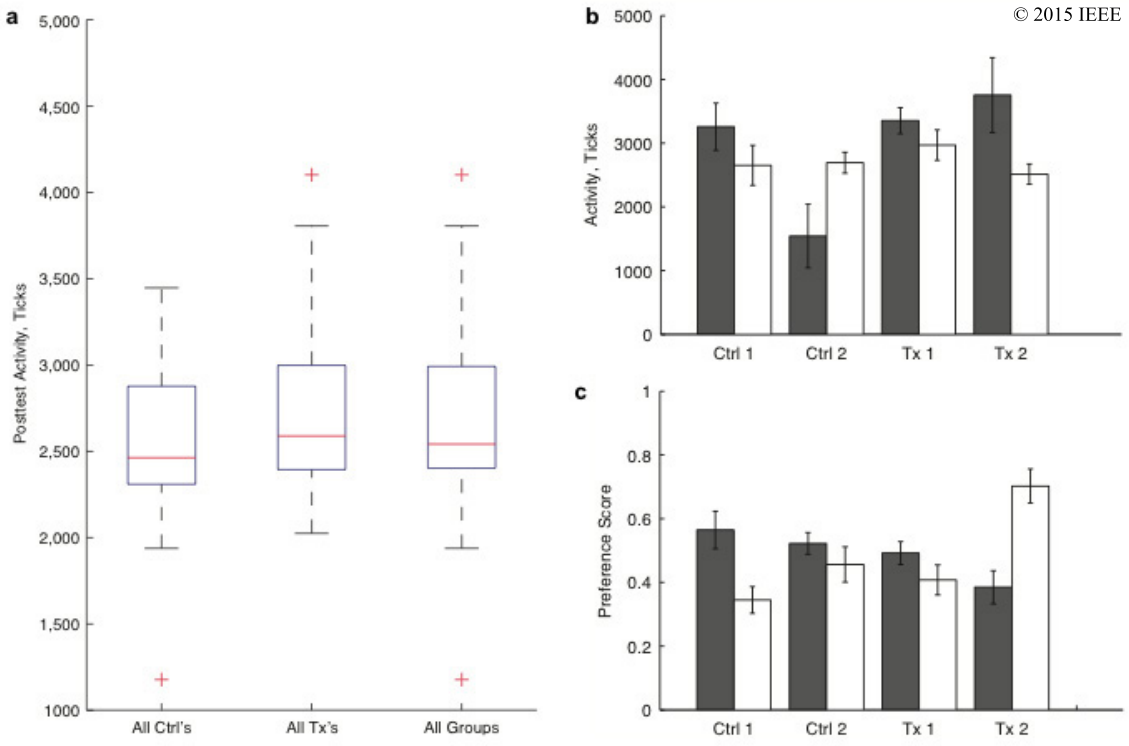

Figure 3.7 CPP results**.** a) Boxplot of post-test activities in the CPP experiments. The lower outlier in the Ctrl group (Ctrl 1) was excluded from analysis due to non-exploratory behavior. b) Activity during the pretest (dark grey) and post-test (white). There was no difference in activity between pretest and post-test for all groups (paired Student's t-test). c) Preference score for pretest (dark grey) and post-test (white). All error bars are standard errors. For statistical analysis between groups, see Figure 3.6.

3.4 Discussion and Conclusion

The OGS is compatible with current behavioral assays in rodents. It offers user defined stimulation protocols, controllable optical dosing, wireless triggering, and deep brain targeting with a modular fiber-ferrule approach. To the author's knowledge, this is

the first untethered optogenetic device to successfully drive behavior dependent on deep brain structures with a fiber-coupled LED. Recently, Hashimoto et al. developed a novel, battery-powered, multi-LED stimulator with wireless infrared control of stimulation parameters (duration, frequency, and pulse width) (111). The device was demonstrated *in vivo* with transcranial stimulation. For targeting intracranial structures, the authors coupled a 0.5-1 mm diameter optical fiber and could produce 1.9 mW/mm^2. This device does not allow control of the optical power and is a relatively large optical fiber if it were to be used in deep brain structures. Importantly, the OGS can control the optical dose by programming the control module. With a 200 μm diameter fiber, an irradiance of 27 mW/mm^2 (21.01 mA) is achieved. The modular OGS design allows for rapid improvements and expansion. As a result, the device serves as a platform to integrate RF circuitry (207) (Chapter 4) to recharge the solid-state batteries or replace them in fully implantable implementations, incorporate an electrical stimulator, and add front-end sensors (56,208), signal processing (28) for closed-loop experimental paradigms (85,115), and aspects of other MCU based optical stimulators (40,111). Importantly, we used commercially available components, so the OGS can be widely accessible. The schematic, suggested PCB layout, fabrication, and basic code for the MCU are made available by request. The future of novel, miniature devices, such as the OGS, is promising. Technological advances paired with the proper molecular tools enable new experimental designs in modern neuroscience research and have far reaching implications for the study and treatment of diseases.

3.5 Materials and Methods – Device Fabrication

The optogenetic stimulator (OGS) was designed and fabricated using a host of equipment and software packages. The device layout for the printed circuit board (PCB) was developed using Osmond PCB software. PCBs were fabricated in house with a milling machine (ProtoMat S100, LPKF, Tualatin, Oregon, USA or Accurate 350, Accurate CNC, Inc., Fort Wayne, IN, USA). All PCBs were populated with components using a combination of reflow and hand soldering. Populated PCBs were cleaned with acetone and then isopropyl alcohol or methanol.

3.5.1 Optical Module

The optical module was fabricated on FR4 printed circuit boards (59 mil thickness, 106394-1, LPKF). Two different sized through holes were drilled into the board to mount the ferrule and LED. From the topside of the board, with a 1.20 mm diameter drill bit (hole ~1.25 mm), the first through hole was made. From the same side, with a 2.00 mm diameter drill bit, the second through hold was made halfway through the board. Due to process variations, the 2.00 mm diameter hole may not always be deep enough and this can be corrected by manually extending the through hole with the drill bit. 1.25 mm diameter zirconia ferrules (Thorlabs) were cut with a diamond-crusted dremel blade, and stripped 200 um diameter optical fibers were inserted into the shortened ferrule and sealed with epoxy. The fiber-ferrule was then polished using previously described protocols. First, a low insertion force connector (CLE-105-01-G-DV, Samtec, New Albany, IN) was populated. Then the LED (PointLED, OSRAM, Munich, Germany) was reverse mounted from the top side of the PCB, and the fiber-ferrule was then inserted

from the bottom side. Medical grade epoxy was used to add mechanical stability to the ferrule-PCB connection. A diamond tipped pen was used to score and break the optical fiber to the desired length. Variation in coupling efficiency of the optical module (Figure 3.3a) has potential to alter optical output for a given driving current. Low efficiency modules required a higher input current to provide the same optical output as a high efficiency module.

3.5.2 Control Module

The control module was fabricated on FR4 PCB (22 mil thickness, 108761, LPKF, Garbsen, Germany). The topside was populated with the microcontroller (MCU, LPC1104UK, NXP, Eindhoven, Netherlands; 2.2 mm x 2.3 mm) and constant current driver (ZLED7012, ZMDI; 2 mm x 2 mm). Low insertion force connectors are used to attach the optical and power modules. This architecture allows the design of low duty cycle operation. Untethered devices benefit from carefully designed stimulus waveforms, where the duty cycle is minimized without decreasing the desired modulation of neural activity, in order to reduce power demands and increase lifetime of operation under a given power budget (135). For example, when calculating with a safety factor of 2, the duty cycle used during *in vivo* experimentation was less than 0.3%. The safety factor doubles the calculated duty cycle. This provides a conservative estimate for design. Wireless triggering is implemented by passively rectifying RF signals at 2.4 GHz (Figure 4.2). This is similar to a previous wireless stimulator design (42); however, power demands are much less for our design since the rectified signal is only driving the trigger which requires significantly less power. Importantly, the batteries and capacitors provide

the necessary power to drive the LEDs. The RF power link calculations are detailed below. When the wireless trigger is not needed, it can be removed.

The Friis transmission equation (209) (Equation 3.1) can be used to estimate the power budget of a wirelessly powered RF system in the far field. Often, the log (base 10) format (Equation 3.2) is preferred since simple addition and subtraction can be used. Here we use the log form and report power values in dBm and antenna gain in dBi. The equations are

$$P_r = P_t G_t \left(\frac{\lambda}{4\pi R} \right)^2 G_r \tag{3.1}$$

$$\begin{aligned} \log(P_r) &= \log(P_t) \\ &+ \log(G_t) + 20\log\left(\frac{\lambda}{4\pi R} \right) + \log(G_r) \end{aligned} \tag{3.2}$$

where, P_r = Power received at the input to the rectifier; P_t = Power transmitter from the RF power amplifier into the transmit antenna; G_t = Gain of the transmitting antenna; G_r = Gain of the receiving antenna; λ = wavelength (2.4 GHz = 0.125 m); R = distance from transmit antenna to receive antenna (1 m).

The power required at the input of the rectifier (1 meter distance) is determined by power required at the comparator input and the efficiency of the rectifier. The input power to the comparator is given by:

$$P = IV_{load} = \frac{V_{load}^2}{R_{load}} \tag{3.3}$$

where, P = Power; I = Current; V_{load} = Voltage across the load (input to the comparator); R_{load} = Resistance of the load. The threshold voltage is 0.2 V and the load is 1 MOhm; therefore, the input power is 43.98 dBm (40 nW). In actuality, slightly less power will be required since the bias current into the comparator is 10 nA (www.maximintegrated.com/datasheet/index.mvp/id/5823). This creates a 0.01 V offset. Assuming a conservatively low rectifier efficiency of 25% (-6 dBm), the required power received at the input to the rectifier is -37.98 dBm (160 nW). Equation 2 can be rearranged to solve for the required power transmitted ($\log(P_t) + \log(G_t)$). Assuming a receiving antenna gain of -10 dBi, the required transmitted power is 12.07 dBm, well below the Federal Communications Commission (FCC) maximum effective isotropically radiated power (EIRP) of 36 dBm (4 W) for ISM bands (FCC, Part 15—Radio frequency devices, Title 47, CFR 15; http://www.ecfr.gov/). There is a nearly a 24 dBm (251.1 mW) buffer to account for other mismatches.

3.5.3 Power Module

The power module was fabricated on 22 mil thick FR4 PCBs. Surface mount (QFN package, 8 mm x 8 mm) or bare dies (5.7 mm x 6.1 mm) of the solid-state batteries (CBC050, Cymbet, Elk River, MN) were used (Figure 3.1-2). For the surface mount batteries, each battery was soldered to a PCB. Two battery-mounted PCBs were then physically stacked and connected. Mechanical stabilization was achieved by threading through holes with wires. Company specified battery-handling instructions were followed (www.cymbet.com, AN-1026).

The die battery module consisted of more complex fabrication procedures. First the pads of the bare dies were stud bumped with a wire bonder. One gold wire bond was made to each pad of the battery. The floating tails (non-bonded end) were manually removed with forceps under a microscope. Conductive epoxy was applied to each of the stud bumped pads and allowed to cure for an hour at 75 ^{o}C. Conductive epoxy was then placed on the battery footprint pads of the PCBs and the bare dies were flipped, attached, and allowed to cure for an hour at 75 ^{o}C. Two batteries were then stacked with a process similar to the surface mount battery modules.

To provide the needed current for stimulation, a 1 mF tantalum capacitor was mounted on a separate PCB (22 mil) and connected in parallel to the batteries. To provide larger values of current, supercapacitors or ultracapacitors may be used as well (Figure 3.2a). When using a tantalum capacitor, it is important to consider the leakage current. Carefully selecting the capacitor and using voltage ratings higher than needed (derating) can minimize leakage and also protect against failures due to transient overvoltages. Capacitor sizing for the batteries is detailed in Cymbet application note AN-1025. Maximum, minimum, and recharge voltages for stimulation were 4.0, 3.0, and 4.1 V, respectively. Briefly, the designer must decide the capacitance value and then determine if there is sufficient recharge time with the intended power source. Importantly, there is a tradeoff between capacitance size and recharge time (Figure 3.2f) that must be considered in order to apply a stimulation protocol. This powering strategy should be used in low duty cycle applications. For more stringent and power demanding experiments, such as a continuous sine wave of stimulation, higher power sources should be used. One possible source is the 10 mA-hr battery used by Hashimoto et al. (111).

3.5.4 Device Programming

The microcontroller (MCU) algorithm was created with CrossWorks for ARM 2.2 (Rowley Associates, Dursley, United Kingdom), a C/C++ development environment. A custom development board was designed and fabricated to allow debug and program download through a 10-pin serial wire debug (SWD) interface. Current, timing, device verification, and power consumption measurements were taken using this development board. Example code specific to this device is made available upon request to any interested external users for looping stimulation protocols.

3.5.5 Optical Measurements

Optical power was measured using a triple power supply (Agilent 3631A; Agilent, Santa Clara, CA), digital multimeter (DMM, Agilent 34410A), optical power meter (PM100D, Thorlabs, Newton, NJ) and sensor (S121C, Thorlabs). The power supply was connected in series to the DMM and optical module. A threaded-fiber adaptor (S120-FC, Thorlabs) was connected to the S121C sensor to prevent non-fiber emitted light from entering. The optical module was stabilized on a stand and the fiber was placed next to the sensor through the FC/PC hole. The power meter was set to “Relative Power” to subtract the ambient light. For blue light, the wavelength, λ, was set to 473 nm. Optical power data points were collected from input currents of 0 – 25 mA. To measure frequency and pulse width data, the development board was used with an uncoupled LED. The PM100D bandwidth was set to “HI” and the analog voltage output was recorded with a 350 MHz oscilloscope (MSO7034B). Since this data is not calibrated by the PM100D

and only timing information was desired, normalized values were reported. The data was normalized by the maximum analog output at a specific current input.

3.5.6 Temperature Measurements

Post euthanasia, devices with dental cement intact were removed from the skull and 2-wire thermistors were superglued to the ventral surface of the optical module. The thermistors were placed adjacent to the optical fiber and the 2-wires were connected to a digital multimeter (DMM; Agilent 34410a) with temperature sensing functionality. The optical module was controlled with a custom LED driver circuit board, waveform generator (Agilent 33522a), triple power supply (Agilent 3631A), and a DMM. The DMM was programmed to sample at 1 Hz for 8 minutes while the optical module was OFF for 1 minute, ON for 3 minutes, and then OFF for 4 minutes. The input current and frequency of stimulation were varied while the pulse width was held at 10 ms. The current was varied at 5, 10, and 20 mA while the frequency was 20 Hz. The frequency was varied at 10, 20, and 30 Hz when the current was held constant. All measurements were taken at room temperature (22 – 24 ºC).

3.6 Materials and Methods – *in vivo* Validation

For the condition place preference (CPP) experiments, B6.SJL-(*CAG COP4*H134R/TdTomato*);*Slc6a3*-cre mice (*Slc6a3*-Cre) were generated by mating B6.*(ROSA)26Sor<tm27.1(CAG-COP4*H134R/tdTomato)>* and B6.SJL-*Slc6a3*$^{tm1.1(cre)Bkmn}$/J mice. In Cre+ mice, the channelrhodopsin:*TdTomato* cassette is

selectively expressed in dopaminergic neurons. Adult Cre+ and Cre- mice (22-35 g) were selected for experimental and control groups, respectively.

3.6.1 Animal Surgery

Mice were anaesthetized in an induction chamber (5% isoflurane) and then prepped for surgery. The mice were secured in a stereotaxic frame (1-2% isoflurane) and given carprofen (IP, 5 mg/kg). After the initial incision, connective tissue was removed until the skull was exposed. A craniotomy was made above the right ventral tegmental area (VTA, AP -3.44, L 0.5). The dura matter was removed and optical fiber was implanted to the VTA (AP, -3.44, L 0.5, DV: -4.1) Coordinates were selected from previous studies(112) and confirmed with the Paxinos mouse atlas (210). Coordinates were adjusted for undersized mice, and a custom stereotactic adaptor was made to hold the optical module. After implantation, the optical module was secured with dental cement (Liquid Denton, Pentron). Mice were given a SQ bolus of warmed sterile saline and allowed to recover for at least 3 full days prior to behavioral testing. The Jackson Laboratory IACUC approved all procedures and protocols (#99108).

3.6.2 Conditioned Place Preference

A randomized 3-chamber CPP procedure was performed over 5 days similarly to previously published protocols (42,112,206). Randomization refers to the chamber assignment for the unconditioned stimulus (discussed below). Two identical unbiased commercial 3-chamber CPP behavioral apparatuses were used (Med Associates, St. Albans, VT). The middle chamber had grey walls with a solid floor while the two side

chambers had a black wall with solid bar flooring and a white wall with mesh grid flooring. On the morning of day 1, the pretest was performed. Mice were given 5 minutes to habituate in the middle chamber and then 15 minutes to explore. For days 2-4, mice were given two 30-minute conditioning sessions, one in the morning and one in the afternoon. Conditioning sessions were at least 4 hours apart. For all morning sessions, devices were attached but no stimulation was provided. During the afternoon session, devices were attached and stimulation (20 Hz for 1 second every 60 seconds, 2-4 ms pulse width, 5-10 mA input current) was provided. On the morning of day 5, the posttest was performed identical to the pretest.

After the pretest, a preference score for the black chamber was made for each subject. Based on this preference, we randomized the chamber in which each subject would always receive optical stimulation (afternoon conditioning session). If any subject had a pretest preference of greater than 80% or less than 20%, they were removed from the study.

3.6.3 Immunohistochemistry

For fluorescent immunohistochemistry, brains were placed into ice-cold 4% PFA for 24 hours followed by 30% sucrose overnight; frozen in OCT compound and cryosectioned at a thickness of 20µm. For immunohistochemical staining, the techniques outlined in the literature (211) were followed with a few alterations. Briefly; slide mounted sections were allowed to warm to room temperature (RT) in a desiccating chamber for 30 minutes and then washed with 5% Triton-X in phosphate buffer (PBST) for 5 minutes. Following this sections were incubated for 2 hours at RT with antibodies

against GFAP, IBA1 or DAT (all Abcam, USA) in 0.5% BSA and 10% chick serum in PBST. Sections were then washed 3 times in PBST for 5 minutes each and incubated with either chicken or rabbit secondary antibodies conjugated to AF488 (Invitrogen, USA) in 0.2% BSA in PBST for 1 hour. Finally sections were washed 3 times for 10 minutes in PBST, incubated with DAPI in PBS for 5 minutes, washed again for 5 minutes with PBST, mounted in Fluoromount, coverslipped, and sealed with nail polish.

For cFos staining a Ventana Discovery XT was used with anti-cFos (Abcam, Cambridge, MA). The detection kit was a ChromoMap DAB, a multimer-based HRP kit (Ventana Medical Systems, Tucson, AZ) using an anti-rabbit secondary (OmniMap anti-rabbit HRP).

For Nissl staining and hematoxylin and eosin (H&E) staining, mice were euthanized by perfusion fixation with ice cold PBS followed by ice cold 4% PFA, embedded in paraffin and serially sectioned to 5μm thick. Sections were deparaffinised with two 5 minute washes in xylene and rehydrated through a graded alcohol concentration (100%, 95%, 70%). For Nissl staining sections were incubated at 60°C in warm filtered cresyl violet solution for 8 minutes. H&E staining sections were incubated in hematoxylin for 4 minutes and washed in water for 5 minutes before being blued in ammonia water for 1 minute. Slides were differentiated in two changes of 95% alcohol before dehydration in 100% alcohol and cleared with xylene. Slides were mounted with Permount, coverslipped and sealed with nail polish.

3.6.4 Experimental Design

For CPP, 4 groups were tested: Control 1 (Ctrl 1, n = 4), Control 2 (Ctrl 2, n = 4), Treatment 1 (Tx 1, n = 8), and Treatment 2 (Tx 2, n = 6). Optical dose per pulse was controlled and determined by multiplying the optical power output by the pulse width (PW) as given by:

$$Dose_{optical} = Power_{optical} \times PW \ . \tag{3.4}$$

The power output for a given optical module at a specific current input is dependent upon the optical efficiency of the LED and coupling efficiency between the fiber-ferrule and LED. The optical efficiency of the LED varies with each batch from the manufacturer and end users are not provided with information. According to the PointLED data sheet, there are four bins of LEDs and the manufacturer does not sort them. Due to this uncontrolled factor and variability in fabrication, optical modules will have some variance in optical power output for a given current input. This variance accounts for the range in optical doses for each group.

Previous studies have shown ChR2 to be activated *in vivo* with pulse widths as short as 1 ms (38). To demonstrate the capacity of the device to titrate optical doses, we first controlled for pulse width (2 ms) and varied the input current for groups Ctrl 1 and Tx 1. The input currents proportionally reflected the irradiance per pulse. Either 5 or 10 mA driving currents were used to deliver the optical doses. There was no behavioral difference between groups, and we believed this was a result of insufficient optical dose. We then hypothesized a higher optical dose would could result in place preference. For

Tx 2 and Ctrl 2, doses were increased by implanting more efficient optical modules and ranging pulse widths from 2-4 ms.

One mouse from Ctrl 1 was excluded from the data analysis due to non-exploratory behavior during the posttest. The subject's activity levels were ruled as low outliers when grouped with all controls and all mice (Figure 3.7). Another subject replaced this control. One mouse participated in both Tx 1 and Tx 2. In Tx 1, this mouse had less than a 0.03 change in preference. When participating in Tx 2, this mouse performed another pretest and was then conditioned with light on the opposite chamber as in Tx 1. Other mice with less than a 0.05 change in preference from Tx 1 were tested as well with increasing dose; however, an unexpected disturbance occurred during testing and all of those subjects were removed from the study.

3.7 Preference Scoring and Statistical Methods

After the pretest, the pretest preference for the black chamber was calculated as:

$$P_{black} = \frac{t_{black}}{t_{black} + t_{white}} \tag{3.5}$$

where, P = preference score and t = time for the respective chambers. The distribution of pretest preferences was plotted in a histogram to determine if the 3-chamber apparatus bias existed. Posttest preference scores were calculated similarly:

$$P_c = \frac{t_c}{t_{black} + t_{white}} \tag{3.6}$$

where P = preference score, t = time, and c = black or white. To obtain the change in preference, the preference scores from the posttest for the chamber paired to the optical stimulation was subtracted from pretest preference score for the same chamber. This is given by:

$$\Delta P = P_{posttest,c} - P_{pretest,c} \tag{3.7}$$

To determine if there was a significant difference in ΔP between means from all groups, an one-way ANOVA for unbalanced groups was performed. A Tukey-Kramer ($\alpha = 0.01$ and 0.05) post-hoc analysis was conducted for multiple comparisons. $P < 0.05$ was used for significance. Pretest and posttest activity scores were compared with a paired Students t-test (Figure 3.7). For comparisons between groups, see Figure 3.6 in the main text. Statistical analyses were made in MATLAB (R2010a; MathWorks, Natick, MA) and STATA 10 (StataCorp, College Station, TX).

3.7.1 Optical Power Analysis

A least squares linear regression in Microsoft Excel was performed on the raw data to predict the optical power output for a given current input. Since input currents were typically 5-10 mA, the regression was not forced to cross the y-axis at zero in order to minimize bias for lower current data points. Descriptive statistical analysis was performed on the slopes and y-intercepts. The mean, 95% confidence intervals and range were calculated in MATLAB.

3.7.2 Temperature Analysis

The ambient temperature, determined by the first minute and last minute of recording, was subtracted from the raw data to obtain the change in temperature due to stimulation. The maximum value from the 3 minutes of stimulation was selected. Five devices were tested and the average maximal change under each set of stimulation parameters was reported. Analysis was performed in Microsoft Excel.

CHAPTER 4. THREE AXIS RCFET WIRELESS POWERING CAGE

Wireless powering of implantable medical devices is a foundational engineering challenge in freely behaving animals. Current rodent behavioral studies are dominated by wired technologies which are physically restrictive, susceptible to infection from the percutaneous connector, and impractical for large scale, chronic experimentation. Batteries are popular with clinical devices; however, the weight, size, and lifetime limit the applications. Wireless powering technology would obviate the aforementioned disadvantages and eliminate the need for batteries. The solution must deliver sufficient power to the load while minimizing harmful biological tissue interactions and noise to the acquisition system. This work will use the principles of strongly coupled magnetic resonance (SCMR) for planted radiofrequency (RF) powering as a solution (136).

To design a magnetic resonance powering system for biomedical applications requires a robust understanding of the relationship between physical design, circuit models, and optimization equations. Previously, others have experimentally demonstrated powering to multiple receivers (138,146), control of impedance parameters or transmit frequency to maximize power transfer with respect to distance (144,212), and powering of a left ventricular assist device (LAD) ex vivo (139). Recently, much work has been performed using microwave filter design methods, specifically the use of impedance inverters (142,144-146). BPF synthesis greatly simplifies the design methodology. As

such, this work will use microwave bandpass filter (BPF) synthesis techniques to design, model, and realize the physical powering solution (144,146,213-215). In particular, the resonantly coupled filter energy transfer (RCFET) method developed by Mei et al. is used to design the WPT system (147). Section 4.1 will introduce basic concepts important to BPF WPT systems. Section 4.2 will detail basic BPF design equations. Section 4.3 arrives at an impedance match condition with respect to the characteristic impedance of K-inverters. While the impedance match condition is not novel, to the author's knowledge, the specific equation has not been shown in literature. Section 4.4 discusses the RCFET method and validates the design solution against the impedance match equation in Section 4.3. The RCFET method should arrive at the same impedance match solution for maximal WPT. Detailed RCFET equations will not be presented as the work is currently unpublished and is the intellectual contribution of Mei et al. (147). Section 4.5 presents the novel design of the three-axis RCFET wireless powering cage and preliminary *in vivo* results. Future work will be to more extensively validate the cage *in vivo*. Novel contributions in this chapter are as follows:

1) Derivation of the optimal impedance match condition with respect to the characteristic impedance of impedance inverters (K-inverters)
2) Design of the three-axis RCFET wireless powering cage
3) Preliminary *in vivo* validation of the cage

4.1 Basic Concepts in Bandpass Filter Wireless Power Transfer Design

4.1.1 Description of Resonantly Coupled Systems

The first demonstration of magnetic resonance coupling used 4 coils—2 loops and 2 resonators (Figure 4.1) (136). The first loop is connected to the powering source and inductively coupled to one resonator. In a mirroring fashion, the second loop is connected to the load and inductively coupled to the other resonator. The two resonators are resonantly coupled.

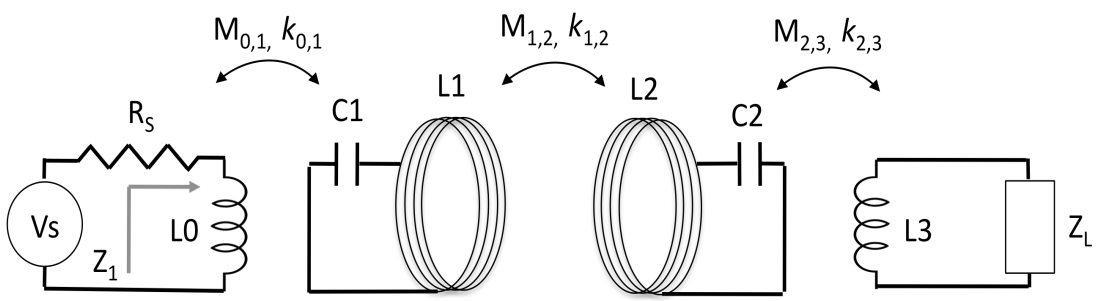

Figure 4.1 Four coil strong magnetic resonance powering configuration. $M_{i,j}$ = mutual inductance between coils i and j. $k_{i,j}$ = coupling coefficient between coils i and j. Cross coupling between L0 and L2, L0 and L3, and L1 and L3 are 0 and not shown in the figure. Z_1 = the impedance seen by the source.

The electromagnetic energy exchange between two coils (i and j) is described by the coupling coefficient, $k_{i,j}$ (142). Coupling is primarily a function of geometry and physical positioning of the powering coils (216). For instance, as two axially aligned coils are separated farther apart or misaligned, the coupling coefficient decreases. The other crucial physical parameter in inductive and magnetic resonant systems is the quality factor, Q, of the coils. The quality factor is the ratio of the energy stored to energy dissipated. In coils, Q can be related to the inductance, L, and series resistance, R, at the resonant angular frequency, w_o, by (Equation 4.1) (216).

$$Q \approx \frac{w_0 L}{R} \tag{4.1}$$

Q and k are the two most import physical factors in maximizing power transfer and are often described as the multiplied entity, kQ (217,218). As k is defined by the physical powering setup, much research has been placed on coil design to maximize Q (218,219). Low kQ systems will limit the maximal power transfer efficiency.

In Figure 4.1, the coupling coefficients $k_{0,1}$ and $k_{2,3}$, are known as external coupling coefficients. These terms describe the relationship between a load or individual input and output ports with the nearby internal resonator. $M_{i,j}$ represents the mutual inductance between coils i and j and describes the rate of magnetic flux change in coil j with respect to the rate of current change in coil i. Similar to the coupling coefficient, the mutual inductance is only dependent on the geometry of the coils. The relationship between $k_{i,j}$ and $M_{i,j}$ is (213):

$$k_{i,j} = \frac{M_{i,j}}{\sqrt{L_i L_j}} \tag{4.2}$$

The mutual inductance between coils directly affects the impedance parameters of the circuit. The impedance seen by coil 1 due to coil 2 is equal to (212):

$$Z_{1,2} = -i\omega M_{1,2} \tag{4.3}$$

where $i = (-1)^{1/2}$ and ω is the angular frequency.

Maximum power transfer between a source and load is observed when the source and load impedances are equal (purely resistive) or conjugately matched (reactive components). One method to meet this impedance match condition is to solve for all the

currents in each unique branch of the circuit (136,212,220). This results in a set of lengthy and complex equations as the number of coils increases. To physically realize the model, the coupling coefficient, $k_{1,2}$, between the two resonators can be determined first by measuring the mutual inductance for a specific distance and orientation. Then the external coupling coefficients can be tuned to meet the impedance condition. Tuning is achieved by rotating or increasing the distance of L0 with respect to L1 or L3 with respect to L2 (136,143). Defining the optimal impedance condition, desired coupling coefficient between resonators, and tuning external coupling coefficients are the critical steps in designing WPT systems for maximum power transfer.

4.1.2 Maximal Power Transfer with BPF Design Methods

BPF synthesis is a well-developed field that has been traditionally used for telecommunications (214,220). Using BPF for WPT is different to telecommunications in two respects (146). Firstly, in WPT system for biomedical applications, the physical system is defined by the end experiment. Then the optimal filter parameters are solved for. In telecommunications, the desired filter parameters are defined first and then the physical solution is realized. Secondly, all the traditional BPF parameters are not critical for optimal performance in WPT. The filter response should be maximally flat; simple Butterworth filters are typically used. The physical power transfer system of Kurs et al. (136) can be viewed as a BPF model (215) (Figure 4.2). This equivalent circuit has 3 primary advantages: 1) a direct-coupled resonator is realized which results in the use of only 2 coils for power transfer, 2) with lumped components, the BPF circuit is easily

implemented on miniature circuit boards, and 3) the optimization of power transfer is greatly simplified.

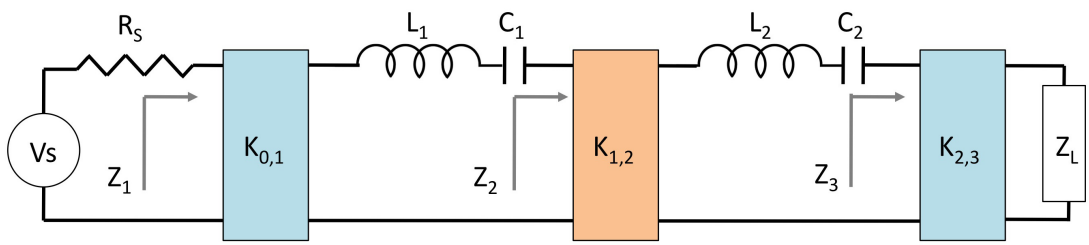

Figure 4.2 Bandpass filter representation of the four coil physical model in Figure 4.1. The coupling coefficients between coils can be modeled as impedance inverters, $K_{i,i+1}$. The external K-inverters are tunable (blue) while the impedance inverter, $K_{1,2}$, is defined by the geometric structure of L_1, L_2 and the distance between them. Z_L is the load impedance. Z_1 is the impedance looking into K-inverter $K_{2,3}$. Z_2 is the impedance looking into $K_{1,2}$, and Z_1 is the impedance looking into $K_{0,1}$. C_1 and C_2 are capacitor values forming resonators with L_1 and L_2, respectively. Coils are assumed to be of low loss. If coils have high loss, a series resistance should be inserted at each coil. R_s is the source resistance and V_s is the AC voltage source.

The mutual inductance between coils can be transformed or represented by immittance (impedance, K, and admittance, J) inverters (142,213). The immitance inverters invert the impedance or admittance seen by the port of analysis (Equation 4.4, Figure 4.3). Previously, both K and J inverters have been used in BPF design of wireless powering (142-145). K and J inverters are reciprocally related and are more convenient when dealing with series and parallel resonators, respectively (213). In this work, K inverters will be used. $K_{i,i+1}$ denotes the characteristic impedance of the K-inverter between coil i and coil i + 1. For external couplings, the K-inverter represents the characteristic impedance between the source or load and the adjacent coil.

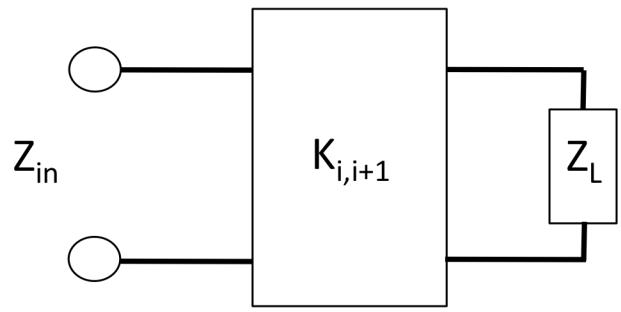

Figure 4.3 K-inverter impedance inversion. $K_{i,i+1}$ can be viewed as a two port network. The K-inverter inverts the output load impedance, Z_L, as seen at the input, Z_{in}.

$$Z_{in} = \frac{K_{i,i+1}^2}{Z_L} \tag{4.4}$$

Maximal power transfer is achieved when the BPF has the lowest insertion loss. This occurs when the proper impedance match condition between the source and load is reached. BPF WPT design methodologies attempt to arrive at either the proper impedance matching conditions (144-146) or minimizing insertion loss (147). Typical behaviors of a resonantly coupled power transfer system are shown in Figure 4.4. Three distinct power transfer regions are observed with two coupled resonators: over-coupled, critically coupled, and under-coupled (Figure 4.4a). Over-coupling provides good power transfer but splitting of the resonant frequency occurs (136,212). The frequency split widens as the coupling coefficient nears 1. Power transfer is now optimal at two different frequencies for a particular coupling coefficient, and power transfer at the resonant frequency is suboptimal. The critically coupled point provides maximal power transfer without frequency splitting, and the under-coupled region provides lower power transfer. The coupling decreases proportionally to cubic distance between the coils (143).

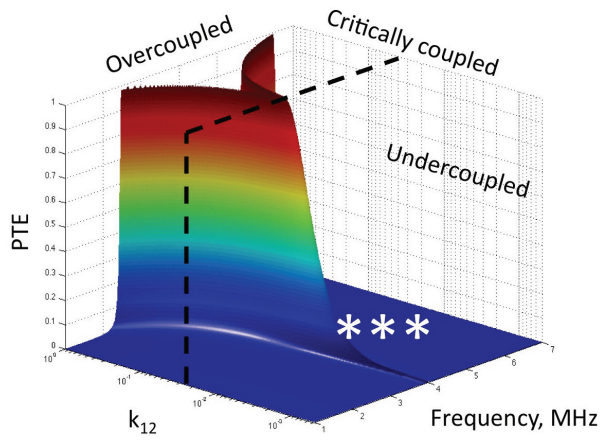

Figure 4.4 Power transfer behavior of two coupled resonators. The dotted line indicates where the critical coupling point. This is where maximum power transfer is achieved at a single frequency. k12 is the coupling coefficient. PTE = power transfer efficiency. *** = undercoupled region and is typically where biomedical devices operate.

Most previous WPT systems have performed in the critical to strongly coupled regions due to the high power transfer efficiencies (136,212,215). This cannot always be realized, however. The general behavior of Figure 4.4 should be observed with any two-resonator power transfer system given that the Q's are infinite. In implantable biomedical systems, though, Q's are typically low due to the size of the receive coil. For instance, Harrison used receive coils with a Q less than 10 (131), and Jow et al. have designed planar spiral coils with Q's less than 90 (219). As Q decreases, the maximal achievable optimal PTE also decreases. Interestingly, at some low Q threshold, a given power transfer system no longer exhibits the critical or over coupling behavior seen in Figure 4.4 (147). This is the case for implantable biomedical systems as Q's of small coils are far from ideal. As in traditional inductive powering topologies, wireless power transfer design is thus limited to the undercoupled region. Traditional inductive coupling techniques, though, load the coils which further decrease the Q (138). Different to traditional inductive powering, K-

inverters do not load the resonant coils and creates the proper impedance match to achieve higher PTE's. The WPT system in this chapter is designed to operate in the undercoupled region but is able to maintain sufficient power transfer due to optimized impedance matching.

4.2 Design Equations

Filter synthesis theory begins with a low pass prototype model that is transformed to the desired filter type (213,214,220). A maximally flat, Butterworth filter response is used throughout this work. From the prototypical element values of the desired filter response, the relationship between mutual inductance and the characteristic impedance can be found. Equations 4.5-11 show the relationships for the BPF in Figure 4.2 (213).

$$M_{i,j} = \frac{1}{\sqrt{g_i g_j}} \tag{4.5}$$

$$K_{0,1} = M_{0,1}\sqrt{R_s L_1 w_0 FBW} \tag{4.6}$$

$$K_{1,2} = M_{1,2} w_0 FBW \sqrt{L_1 L_2} \tag{4.7}$$

$$K_{2,3} = M_{2,3}\sqrt{Z_L L_3 w_0 FBW} \tag{4.8}$$

$$w_0 = 2\pi f_0 \tag{4.9}$$

$$g_0 = g_3 = \sqrt{2} \tag{4.10}$$

$$g_1 = g_2 = 1 \tag{4.11}$$

where FBW = fractional bandwidth, f_0 = resonant frequency, w_0 = resonant angular frequency. The element values are specific to the maximally flat filter response and others can be found in tables from microwave filter textbooks (213). From Equations 4.2

and 4.6-8, the relationship between coupling coefficient and the characteristic impedance of K-inverters can be easily determined. K-inverters can be physically realized by several circuit topologies and many options can be found in Matthieu et al (213). In this work, a 2 capacitor network is used to represent the external couplings (Figure 4.5).

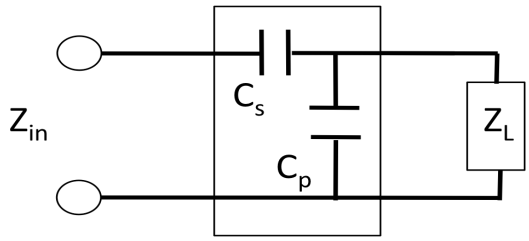

Figure 4.5 The physical realization of the external K-inverters, $K_{0,1}$ and $K_{2,3}$. C_s and C_p are series and parallel capacitors, respectively. Z_L is the load impedance and Z_{in} is the input impedance of the K-inverter.

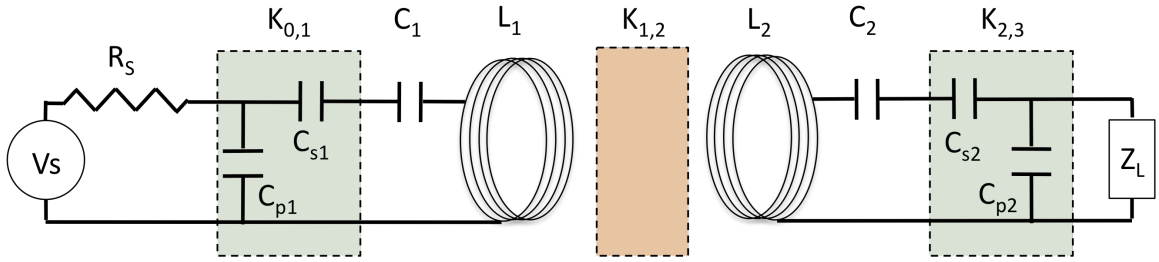

Figure 4.6 Physical implementation of the bandpass filter. The external coils are replaced by $K_{0,1}$ and $K_{2,3}$. $K_{1,2,}$ is defined by the geometrical properties of L_1 and L_2. C_1 and C_2 form a resonant structure with L_1 and L_2, respectively. C_1 and C_2 can be absorbed by C_{s1} and C_{s2}, respectively, to reduce components. Z_L is the load impedance. R_s is the source resistance. Vs is the AC source voltage. Compare to Figure 4.1 and Figure 4.2.

The resulting physical manifestation of the BPF is shown in Figure 4.6. Assuming Z_L is purely resistive, the relationship between the capacitors and the characteristic impedances of the K-inverters are (147,213):

$$C_{p1} = \frac{\sqrt{R_s^2 - K_{0,1}^2}}{w_0 K_{0,1} R_s} \tag{4.12}$$

$$C_{s1} = -\frac{1 + w_0^2 C_{p1}^2 R_s^2}{w_0 K_{0,1} R_s} \tag{4.13}$$

$$C_{p2} = \frac{\sqrt{Z_L^2 - K_{2,3}^2}}{w_0 K_{2,3} Z_L} \tag{4.14}$$

$$C_{s2} = -\frac{1 + w_0^2 C_{p2}^2 Z_L^2}{w_0 K_{0,1} Z_L} \tag{4.15}$$

The values of C1 and C2 are determined by the desired resonant frequency, f_0 (equations 4.16-17), and can be absorbed by C_{s1} and C_{s2}, respectively for physical implementation.

$$f_0 = \frac{1}{2\pi\sqrt{L_1 C_1}} \tag{4.16}$$

$$f_0 = \frac{1}{2\pi\sqrt{L_2 C_2}} \tag{4.17}$$

From the previous equations, the physical realization of K-inverters allows the direct tuning of the external coupling coefficients by 2 capacitor values. Additionally, it removes the need for inductors L_0 and L_3 (Figure 4.1 versus Figure 4.6). Deriving the impedance match condition will inform how the capacitors should be tuned.

4.3 K-inverter Impedance Match Condition for a 2 Resonator BPF

The impedance matching condition of resistive loads for maximum power transfer occurs when $Z_1 = R_s$. Previously, Lee et al., demonstrated this condition for J-inverters (144). A similar analysis can be applied to K-inverters. For a 2 resonator BPF (Figure 4.2), the impedance matching condition for the BPF is determined in Equations 4.18-4.23. In this analysis, it is assumed that the coils are lossless (high quality factor).

$$Z_3 = \frac{K_{2,3}^2}{Z_L} \tag{4.18}$$

$$Z_2 = \frac{K_{1,2}^2}{Z_3} = \frac{K_{1,2}^2 Z_L}{K_{2,3}^2} \tag{4.19}$$

$$Z_1 = \frac{K_{0,1}^2}{Z_2} = \frac{K_{0,1}^2 K_{2,3}^2}{K_{1,2}^2 Z_L} \tag{4.20}$$

$$Z_1 = R_s = \frac{K_{0,1}^2 K_{2,3}^2}{K_{1,2}^2 Z_L} \tag{4.21}$$

$$K_{1,2}\sqrt{Z_L R_s} = K_{0,1} K_{2,3} \tag{4.22}$$

Assuming a 50 ohm source and load, the matching condition is Equation 4.23.

$$K_{1,2} 50 = K_{0,1} K_{2,3} \tag{4.23}$$

The process to design a BPF wireless powering system using the impedance match condition is as follows. First, $M_{1,2}$, L_1, and L_2 are measured with a vector network analyzer at the resonant frequency. $K_{1,2}$ can then be determined. $K_{0,1}$ and $K_{2,3}$ are arbitrarily chosen to satisfy Equation 4.23. The capacitor values are determined by

Equations 4.12-4.15. For low Q power transfer systems, the series resistance of each coil would need to be added to the circuit model and equations. The high Q impedance match condition (Equation 4.23) is used in Section 4.4 to validate the RCFET design methodology.

4.4 RCFET Methodology

The RCFET design methodology developed by Mei et al. optimizes the BPF for minimal insertion loss (147). The design method is unique in 2 respects: 1) the method arrives at the minimal insertion loss criteria using the measured coil properties of inductance, quality factor, and mutual inductance, and 2) K-inverter realization of the capacitor values is not arbitrary. Previous methods in BPF synthesis optimize by only measuring L and k and then arbitrarily choosing characteristic impedances to arrive at the impedance match condition (144,146,215). As k and Q are both critical factors in PTE, this difference allows the designer to predict the power seen by the load in simulation and also realize realistic capacitor values for the K-inverters without several design iterations. The RCFET design method is as follows: 1) measure coil properties and coupling coefficient range between coils, 2) define a targeted critical coupling point to optimize for, 3) calculate the optimal mutual inductances 4) calculate the characteristic impedances and 5) determine the K-inverter capacitor values. A comparison to previous design methods is shown in Figure 4.7.

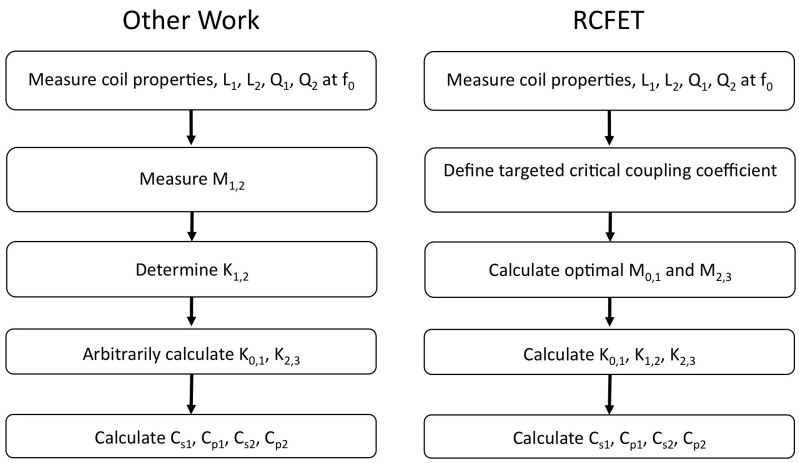

Figure 4.7 Design process of BPF wireless powering systems. The left flow chart calculates capacitor values by arbitrarily choosing characteristic impedance values for $K_{0,1}$ and $K_{2,3}$ to satisfy equation 4.23. The RCFET design method is shown on the right column.

As the design equations of the RCFET are unpublished, they will not be provided here. Instead, simulations and physical measurements are used to validate against the derived K-inverter impedance match condition. To demonstrate the RCFET methodology, a 2 resonator BPF design example is shown. Measured quantities including L_1, L_2, Q_1, and Q_2 can be found in Table 4.1. Figure 4.8 displays how the coupling coefficient changes with respect to distance for coils L_1 and L_2. The target critical coupling point critical is chosen to be equal to 0.03. To validate the RCFET derived capacitor values, the impedance match condition from Equation 4.23 is first verified and the values are reported in Table 4.1. The values are in good agreement. The slight mismatch is due to finite Q, which is not accounted for in Equation 4.23. RCFET, however, does account for coil losses. $k_{1,2}$ is approximately 0.03 at 11 cm (Figure 4.8) and the PTE was measured by the S21 response

(Figure 4.9). Simulation (dotted black trace, Figure 4.9) and measurement (blue trace) are in good agreement thereby validating the RCFET methodology.

Table 4.1 Two Resonator BPF Design Example

RCFET Input values		**Calculated values**	
L_1	805.7 nH	$K_{0,1}$	9.0401
L_2	805.8 nH	$K_{1,2}$	0.8096
Q_1	383.5	$K_{2,3}$	4.5159
Q_2	95.71	$C_{s1} \parallel C_1$	2.438 nF
f_0	3.998 MHz	C_{p1}	10.111 nF
FBW	0.04	$C_{s2} \parallel C_2$	3.188 nF
R_s	50 Ω	C_{p2}	5.007 nF
Z_L	50 Ω	**$K_{1,2}$ x 50**	**30.3608**
		$K_{0,1}$ x $K_{2,3}$	**30.8175**

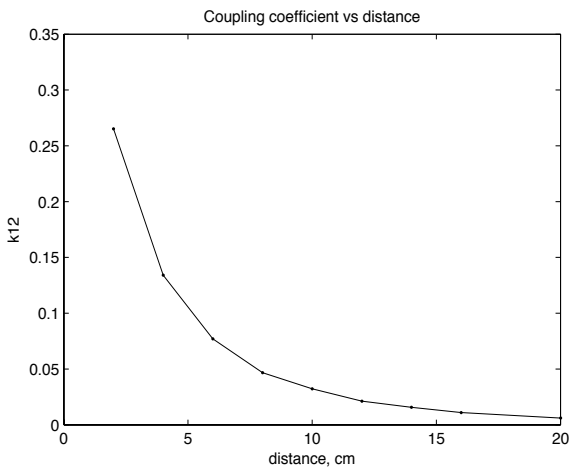

Figure 4.8 Coupling coefficient, $k_{1,2,}$ for two resonator BPF design example. $k_{1,2}$ decreases as the distance increases between coils L_1 and L_2. Coil parameters are found in Table 4.1.

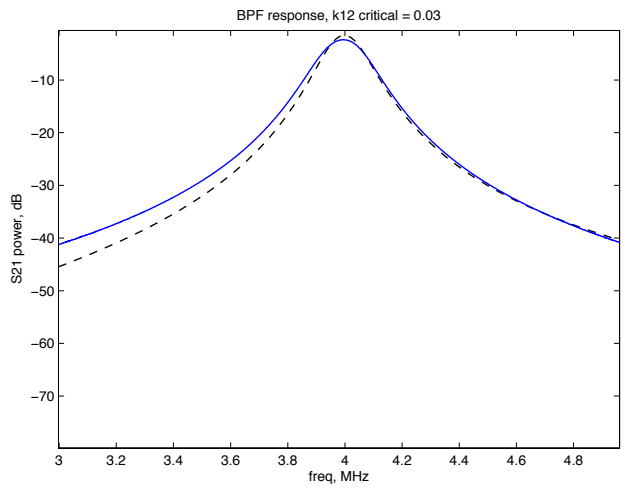

Figure 4.9 Simulation and measurement of the PTE with respect to frequency. Power transfer is nearly 0 dB at the critical coupling point. Refer to Table 4.1 for component properties of the RCFET design example.

4.5 Three-axis RCFET powering cage

Wireless technology for freely behaving animal experiments require powering in three spatial axes. The two resonator powering strategy is sufficient for experiments where the subject is stationary (i.e. a virtual reality jet ball). Chronic, epilepsy related experiments, though, need spatial freedom to study seizures and behavior. The engineering objective is to design a powering system that would allow unrestricted rodent housing and continuous powering. The proposed solution is a three-axis RCFET cage (Figure 4.10). Coil 1 is the transmit coil and has magnetic, B, fields in the Z-axis. Coils 2a and 2b are relay coils with B fields in the X axis and Y axis, respectively.

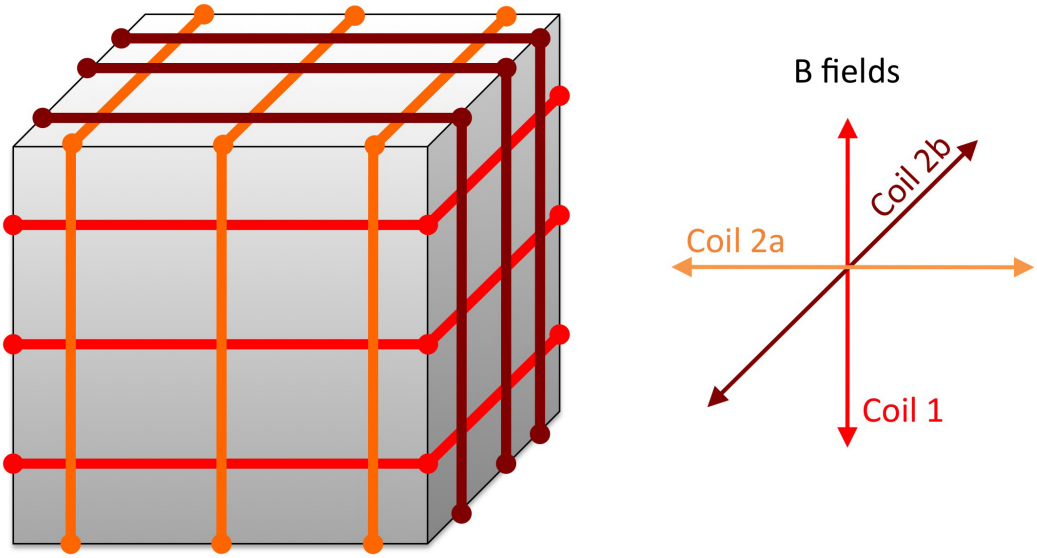

Figure 4.10. Three-axis RCFET wireless powering cage. Direction of magnetic fields, B, produces are shown on the right. The cage dimensions are 12” x 12” x 11.5” (L x W x H). The coils are made of 8 gauge copper wire. The top center wires are removable to provide access for the subject. The receive coil is circular and 20 mm in diameter (not pictured).

The cage design method is to 1) define acceptable coil sizes 2) sweep coil parameters for high Q with respect to frequency 3) measure coil to coil coupling 4) determine optimal capacitor values using RCFET and 4) verify simulations with measurements. This is similar to the method in Figure 4.7. The cage is first characterized assuming a 50 ohm source and 50 ohm load. This allows s-parameter measurements with the vector network analyzer. Once the correct impedance matching conditions have been established, the features of the power transfer frequency response are recreated for a complex, non-50 ohm load. In the case of powering a device, the load is a rectifier (AC to DC converter) with storage capacitors and voltage regulation.

According the NIH Guide for the Care and Use of Laboratory Animals, group housing rats weighing 400-500 g require 60 in^2/rat of floor space and 7 inches of height (221). Often rats induced with seizures are singly housed and would require more floor space. To allow ample of space, the powering system is designed to fit a separate 11 x 11 x 11 in^3 housing unit. The powering system is built with a polycarbonate box. The primary external source coil, coil 1, wraps around the box first. Then two other external coils, coil 2a and 2b, are wrapped perpendicularly to coil 1 (Figure 4.10). Coil 2a and 2b weakly couple to coil 1 and serve as relay coils to reorient the magnetic fields. Coils 1 – 2b are nearly the same size and have similar Q factor and inductance values (Table 4.2). The Q is slightly lower for both coil 2a and 2b since both coils contain detachable wires to allow entrance of the animal. The receive coil is small compared to the wrapped coils. The diameter is 20 mm, and this size is tolerable by adult (260 g or larger) rats. Decreasing the implantable coil size is an optimization that should be considered for future iterations of the powering system.

Table 4.2 Coil Parameters for a Three-Axis RCFET Wireless Powering Cage

	Coil 1 (Transmit)	Coil 2a (Relay)	Coil 2b (Relay)	Coil 4 (Receive)
Measured Q @ 4 MHz	323.8	262.5	270.1	85
Inductance L, nH @ 4 MHz	4252	4400	4325	346.9
Size and shape	12” edges square	12.25” edges square	12.5” edges square	20 mm diameter, circular
Number of turns	3	3	3	3

4.5.1 Magnetic Field Interactions

The three external coils allow energy to couple the receive coil in all orientations. There are 2 general powering strategies to couple energy to the receive coil: 1) use each external coil as an independent source coil 2) use one external coil as the source and the other 2 coils as relays. Option 1 more simply realizes continuous powering through theory as the case is simply 3 independent, 2 resonator BPF's. Practical realization is costly and disadvantageous, though. Multiple signal generators, phase shifters, and power amplifiers would be required. Option 2 is theoretically more challenging, but implementation requires only a single signal generator and power amplifier. Power is transferred either directly from coil 1 to coil 3 or indirectly from coil 1 to relay (coil 2a, coil2b) to coil 3. Option 2 is used due to cost and end user accessibility.

The interaction of magnetic fields from the drive coil and relay coils to the receive coil must be considered for powering in various orientations. This conceptualization and result is critical, as extensive coupling coefficient measurements would otherwise be required with each cage iteration to observe the behavior. Current through coils 1, 2a, and 2b create alternating magnetic fields with component vectors in the Z, X and Y directions, respectively. According to Faraday's Law, the magnetic field from coil 1 induces an electromotive force (emf) that is seen by both coils 2a and 2b. The emf pushes a current through the relay coils, which then create magnetic fields. The emf is 90° out of phase with respect to the coil 1 magnetic field (Figure 4.11). At resonance, the impedance is real, and the induced current within the relay coils is in phase with the emf. Given these conditions, the coil 2a magnetic field is always in phase with the coil 2b magnetic field. For simplicity, the interaction between coil 2a and 2b is first considered. If both relay

coils are coupling energy, using vector addition, the total magnetic field will oscillate in amplitude in a singular direction throughout the entire XY plane (Figure 4.12). When the receive coil is perpendicular to the total magnetic field vector, then the most amount of power will be received as the induced currents due to the component magnetic vectors are in the same direction and sum. When the receive coil is parallel to the total magnetic field vector, then the least amount of power will be received. The induced currents due to the magnetic vectors are in opposite directions and cancel. In this particular case, the receive coil will see either maximal or no power at 45° (225°) and 135° (315°) with respect to either relay coil. Coils 2a and 2b couple energy equally into the receive coil at these orientations. Adding a Z component to the total vector does not influence the power transfer when the receive coil is perpendicular to coil 1. To avoid the dead orientations (no power transfer), coils 2a and 2b cannot be simultaneously coupling energy.

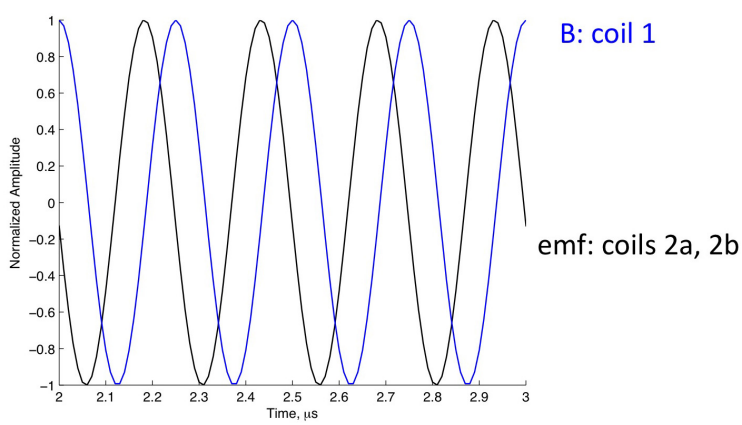

Figure 4.11 Phase of induced emf of relay coils 2a and 2b at resonance (4 MHz). The magnetic flux, B, due to coil 1 induces an emf in coils 2a and 2b. When the slope of B is 0 (peaks and troughs), then the induced emf goes to 0. The resulting current in the relay coils is in phase with the induced emf. The magnetic flux from coils 2a and 2b are then in phase with each other and out of phase with coil 1. Amplitude is normalized.

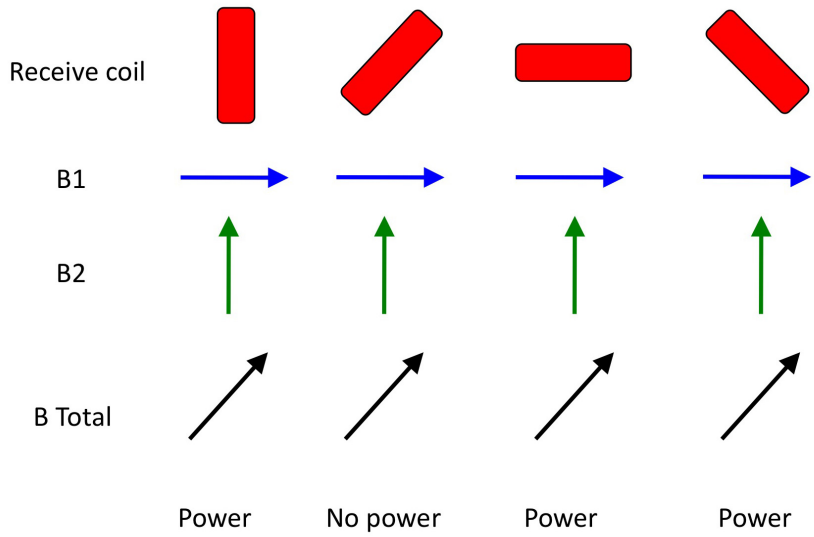

Figure 4.12 Power transfer when two external powering coils have in phase magnetic fluxes. The receive coil (red) is shown in various orientations in one plane. B1 and B2 represent the magnetic flux orientation of two coils. The flux magnitude will follow the sinusoidal pattern shown in Figure 4.11 (blue trace). B total is the sum of B1 and B2. The direction of B total will become negative when B1 and B2 are both negative. Power is maintained except in the second orientation from the left. The B1 and B2 components will induce currents in opposite directions at the same time within the receive coil If the currents are equal in magnitude, no power will be received. If there is a 90° phase difference between B1 and B2, the currents in orientation 2 will still be opposite; however, the time difference between the induced currents prevents cancellation.

The case of power transfer due to interactions between coil 1 and one relay coil (2a or 2b) is more complex. The case will be considered for interactions between coil 1 and coil 2a. The coil 1-coil 2b case should be nearly equal. The magnetic field between coil 1 and coil 2a is 90° out of phase since at resonance. The induced emf seen by coil 2a and resulting current are in phase. The total magnetic field vector over one period of oscillation generates vectors in every direction of the XZ plane. This should result in no power transfer dead orientations when the receive coil is perpendicular to the plane. Some orientations will have weaker power transfer than others, though, as the magnetic field

from coil 1 is greater than coil 2a. The coil 1-coil 2b case is similar but with field components in the YZ plane.

The results from the magnetic field interactions analysis provide the following physical guidelines for the cage design: 1) coil 1 and a relay coil can provide power transfer to a receive coil in all orientations perpendicular to the powering plane, and 2) coils 2a and 2b cannot concurrently act as relays. The design solution is realized with optical solid-state relays to switch the relay coils on and off (Table 4.3). When coil 2a is acting as a relay, the terminals of coil 2b are shorted. When coil 2b is acting as a relay, the terminals of coil 2a are shorted. This solution sets the physical conditions of cage. The power transfer system can be modeled as a three resonator BPF with two operating conditions.

Table 4.3 Operation of the Transmit and Relay Coils

	Time Point 1	Time point 2
Coil 1 (Tx)	ON	ON
Coil 2a (Relay)	ON	OFF
Coil 2b (Relay)	OFF	ON

4.5.2 Three Resonator BPF and Impedance Match Condition

When compared to the 2 resonator BPF, the three resonator BPF model introduces two K-inverter terms. Figure 4.13 is the model for a 3 resonator BPF. L_1 is the transmitting coil; L_{2n} is the nth relay coil; L_3 is the receive coil; R_s is the source resistance (50 Ω); Z_L is the load impedance; $Z_{1\text{-}4}$, are the input impedances seen by the respective K-inverters, $K_{i,j}$; C_m is the resonating capacitor for L_m; and V_s is an AC voltage.

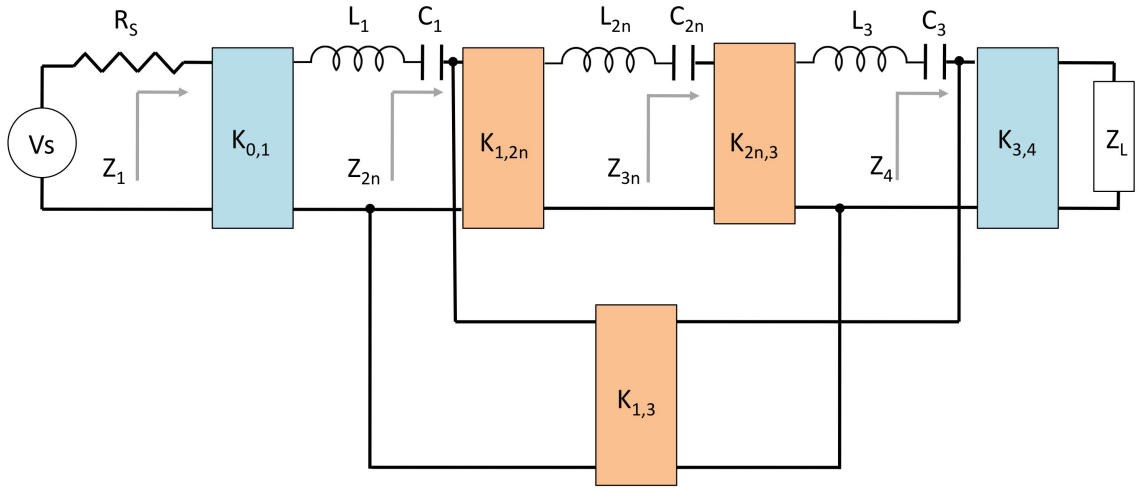

Figure 4.13 Three resonator BPF model of the three-axis powering cage. Orange K-inverters are set by the geometric relations of the coils L_1, L_{2n}, and L_3. The blue K-inverters are tuned using a two capacitor topology. L_1 is the transmit coil, L_{2n} is relay coil 2a or 2b, L_3 is the 20 mm diameter receive coil. Z_L is the load impedance and Z_i is the input impedance of the $K_{i,i+1}$ inverter. V_s is the AC voltage source.

If it is assumed that the components are lossless, the source and load are real, and no coupling exists between coil 1 and the receive coil, then the coupling coefficient between coil 1 and 3 and $K_{1,3}$ are 0. Under this condition, deriving the optimal impedance match condition with respect to K-inverters is straightforward and follows the process from Equations 4.18 – 4.23. When $Z_1 = R_s$, then the relationship between characteristic impedances is denoted by Equation 4.24.

$$K_{1,2}K_{3,4} = K_{0,1}K_{2,3} \tag{4.24}$$

When cross coupling between resonators (i.e. $k_{1,3}$) cannot be ignored, then the impedance match condition can be solved by using the impedance matrix. Lee et al., previously provided the matching condition with J inverters for optimal power transfer in a BPF

model with relay coils (145). As J inverters are reciprocal to K-inverters, this condition is easily adapted to the K inverter case. The optimal power transfer is observed when:

$$[Z]_{1,1}^{-1} = \frac{1}{2R} \tag{4.25}$$

where [Z] is the impedance matrix of the BPF, and R is the impedance value of the source, R_s, and load, Z_L, (assumed to be equal). The impedance matrix terminology for a BPF can be found in standard microwave filter-engineering textbooks (213,214). Using Matlab, the $[Z]_{1,1}^{-1}$ term is shown in Equation 4.26.

$$[Z]_{1,1}^{-1} = \frac{K_{1,2n}(K_{1,2n}K_{3,4}^2 - 2K_{1,3}K_{2n,3}Rj)}{R(K_{0,1}^2K_{2n,3}^2 + K_{1,2n}^2K_{3,4}^2 - 2K_{1,3}RK_{1,2n}K_{2n,3}j)} \tag{4.26}$$

To verify that the RCFET method and this impedance match condition can arrive at the same solution for a 3 coil BPF, a simulation is run with arbitrary coil parameters and coupling coefficients (Table 4.3). High Q components are assumed, and the source and load are 50 ohms. The impedance match condition sets $[Z]_{1,1}^{-1}$= 0.01. From Equation 4.26, the RCFET method arrives at $[Z]_{1,1}^{-1}$ = 0.0108 + i00261. These values are in good agreement. The advantage of the RCFET method becomes obvious as the number of resonators used in a BPF increases. Arbitrarily sweeping parameters to find usable characteristic impedances for $K_{0,1}$ and $K_{3,4}$ to satisfy the impedance matrix derived solution would be tedious and inefficient. Additionally, while the impedance match

condition can be determined for low Q coils used implantable biomedical applications, the equations quickly complicate with increasing number of coils.

Table 4.4 Three resonator BPF design example

RCFET Input values		Calculated values	
L_1	6465 nH	$K_{0,1}$	6.49e5
L_2	4098 nH	$K_{1,2}$	3.32e8
L_3	400 nH	$K_{2,3}$	2.75e7
Q_1	10000	$K_{3,4}$	5.41e4
Q_2	10000	$K_{1,3}$	2.02e8
Q_3	10000	**1/2R**	**0.01**
f_0	4.0 MHz	$[Z]_{1,1}^{-1}$	**0.0108-0.0026i**
FBW	0.043		
R_s	50 Ω		
Z_L	50 Ω		

5.5.3 Coupling Coefficient Factors and Measurements

Defining the critical coupling coefficient to be used in the RCFET method requires knowing the range of coupling coefficients between the receive coil and the source or relay coil. Additionally, the general trends of coupling are important for design. The coupling coefficient can change with respect to receive coil location and orientation. To map the coupling coefficient trends with respect to location in the cage, the mutual inductances at various locations within coil 1 are measured with a 2-port setup in with the VNA (Figure 4.14). This method provides a faster technique to understand the general trend of coupling, but the measurements are less accurate than a 1-port measurement (213,214). These measurements are lower than the true coupling coefficient since the low Q receive coil is further loaded. After understanding the general trends, a more accurate range of coupling coefficients is later established through simulation in ADS and 1-port

measurements. Coil 1 and the receive coil were aligned in a parallel fashion. The XZ plane coupling map shows a saw tooth pattern for coupling. The greatest coupling occurs near the coil wrappings and the smallest coupling is half way between two consecutive coil turns (Figure 4.14a). The YZ plane has the same trend. The XY plane coupling map shows that the coupling is greater on the ends and dips toward the middle (Figure 4.14b). As the XY plane is moved along the Z axis, the same trend is observed. At Z = 6.5 cm and 13.5 cm, though, instead of dipping towards the center, the coupling increases. This shows that the worst coupling points are at the corners for 6.5 and 19.5 cm along the Z axis. Away from the external coil edges, the coupling in the majority of the space is homogeneous. As the receive coil orientation is rotated from parallel to perpendicular with respect to coil 1, the coupling coefficient decreases and drops to 0 at 90°. These general trends hold when the receive coil couples to any coil, source or relay. Understanding the general trends in coupling, the locations with the maximum and minimum coupling are measured with a 1-port technique. Simulation in ADS is then used to establish a more accurate coupling coefficient range (147). The range of $k_{1,3}$ is 0.0049 to 0.0064.

The optimal power transfer condition is different for every unique coupling coefficient. For a first generation technology, the goal of the powering system is to provide sufficient powering and not always optimal powering under every condition. The power required by a device described in chapter 2 is typically < 4 mW. Assuming a 60% rectifier efficiency, 6.67 mW of power delivered to the load is the targeted specification. Source power is designed for 500 mW, although higher levels can be used. The minimum

power transfer efficiency specification at a singular frequency for all coupling configurations is 1.33%.

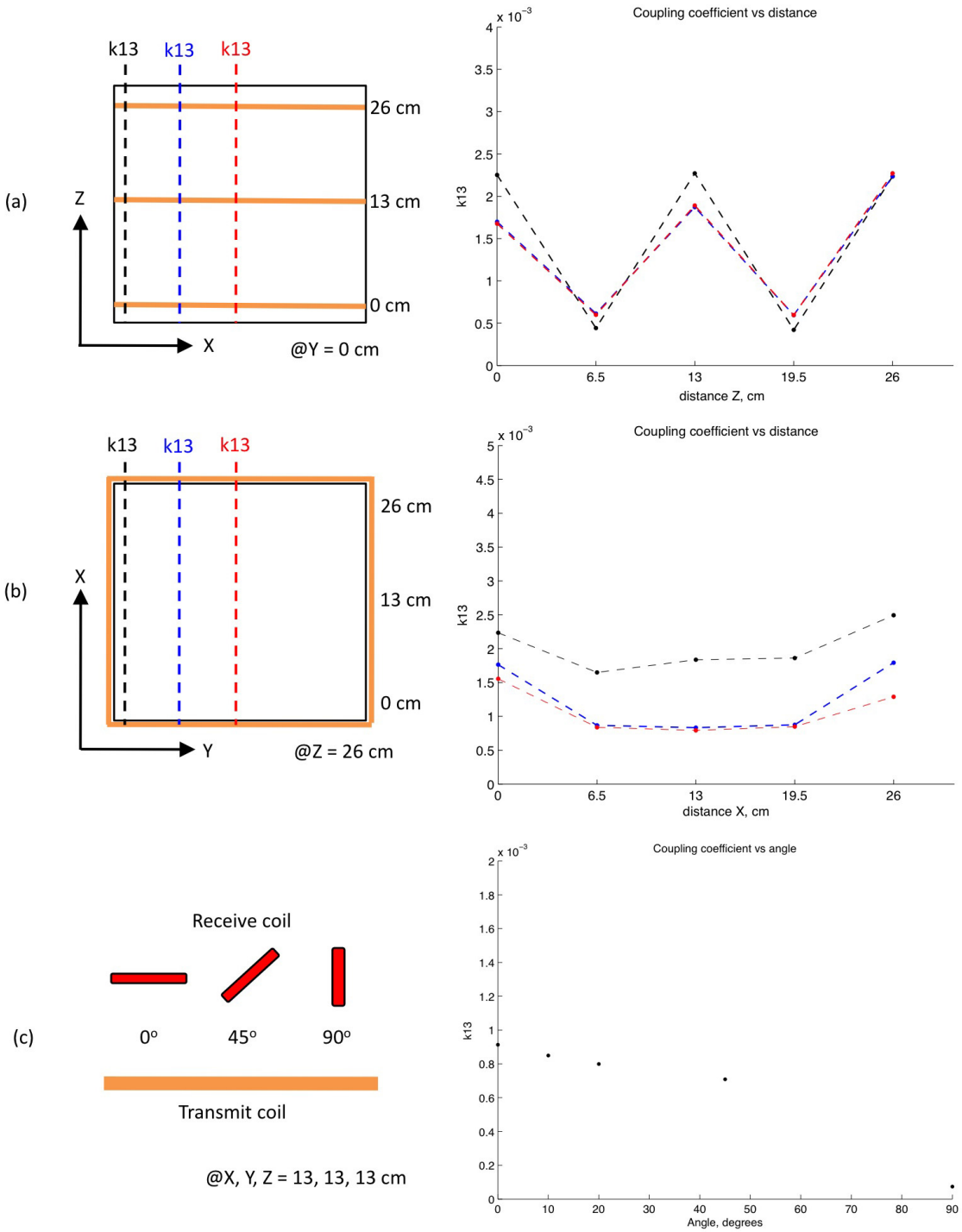

Figure 4.14 Coupling trends throughout the three axis cage. k13 is the coupling coefficient between the transmit and receive coils. a) Coupling in the XZ plane at Y = 0 cm. The receive coil is moved along the dotted lines in the Z direction. Colors of the dotted line in the schematic correspond to the colors in the plot. Coupling is greatest near the coil wrappings (0, 13, 26 cm). The coupling dips between the wrappings (6.5, 19.5 cm). These dips are the weakest coupling points when the receive coil is parallel to the transmit coil. The same trend is observed in the YZ plane. b) Coupling in the XY plane at Z = 26 cm. The receive coil is moved along the dotted lines in the X direction. The greatest coupling occurs at the ends (0 and 26 cm). The coupling dips toward the middle. The same trend is observed while moving the XY plane along the Z-axis. c) Coupling as a function of angle. As the receive coil is turned from parallel to perpendicular, the coupling drops. At 90°, the coupling is negligible.

The parameters used for optimization are shown in Table 4.5. The targeted critical coupling point between the receive and transmit coil is 0.005, which is near the coupling coefficient of most cage areas away from the edges. The implemented capacitor values were verified by measurement on the VNA.

Table 4.5 3-Axis RCFET Wireless Powering Cage Optimization Parameters

RCFET Input values		**Calculated values**	
L_1	4252 nH	C_{s1}	399.12 pF
L_{2a}	4400 nH	C_{p1}	5430.31 pF
L_{2b}	4325 nH	C_{s2}	6303.30 pF
L_3	346.9 nH	C_{p2}	16497.64 pF
Q_1	323.8		
Q_{2a}	262.5		
Q_{2b}	270.1		
Q_3	85	**Implemented values measured by VNA @ 4 MHz**	
f_0	4.0 MHz	C_{s1}	399.6 pF
FBW	0.043	C_{p1}	5.413 nF
R_s	50 Ω	C_{s2}	6.272 nF
Z_L	50 Ω	C_{p2}	16.972 nF
k_{12a}	0.0047		
k_{13} (target)	0.005		
$k_{2a,3}$	0.001		

The physical realization of the cage is shown in Figure 4.15. Receive coils and power measurement systems for a 50 Ω load and complex load are pictured in Figure 4.15c. The coil on the left of is matched for a 50 Ω load. The devices in the middle and on the right of Figure 4.15c are wireless power measurement boards used when transitioning to a non-50 Ω. Using a 2-port setup on the VNA, the power transfer measurements are made by connecting the $K_{0,1}$ input to port 1 and $K_{3,4}$ output to port 2. The power transfer simulation and measurements for a 50 Ω load are shown in Figure 4.16.

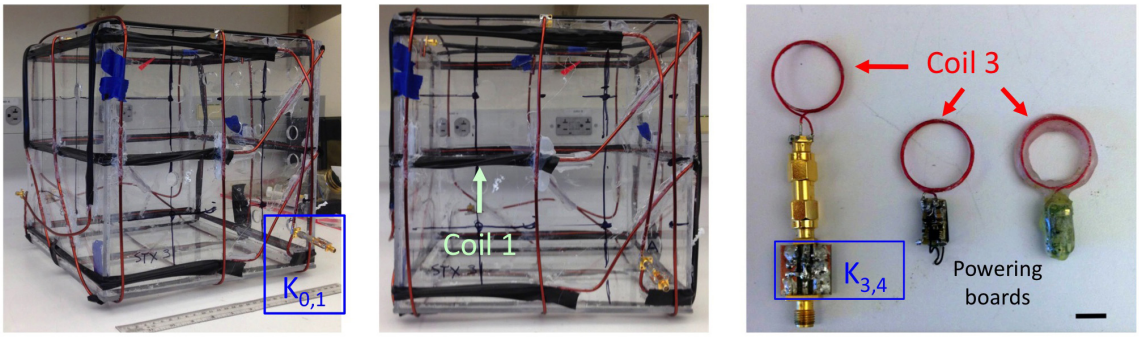

(a) (b) (c)

Figure 4.15 The three axis RCFET powering system. a) side angled view of cage. The external K inverter, K_{01}, is boxed in blue. Three perpendicular coils are seen. Each side of the bottom of the cage is 12 inches. The height is 11.5 inches. b) Side view of cage. The arrow points to coil 1. Coil 2 wraps vertically and perpendicular to coil 1. c) Receive coils and powering boards. Coil 3, the receive coil, is shown by the red arrows. $K_{3,4}$ for a 50 ohm load is boxed in blue. The devices on the left are unpackaged (middle) and packaged (right) versions of the wireless power measurement system. The AC voltage is rectified to DC and then measured with a MCU. The data is then wirelessly transmitted to a basestation. Sampling occurs at 2.5 kHz. The black bar is 5 mm.

Figure 4.16 displays power transfer in terms of S21. Measurements at a strong and weak coupling points corresponding to the general trends in Figure 4.14 are made. Additionally, a measurement is taken at the middle of the cage. All measurements are taken with the receive coil parallel to the transmit or relay coil.

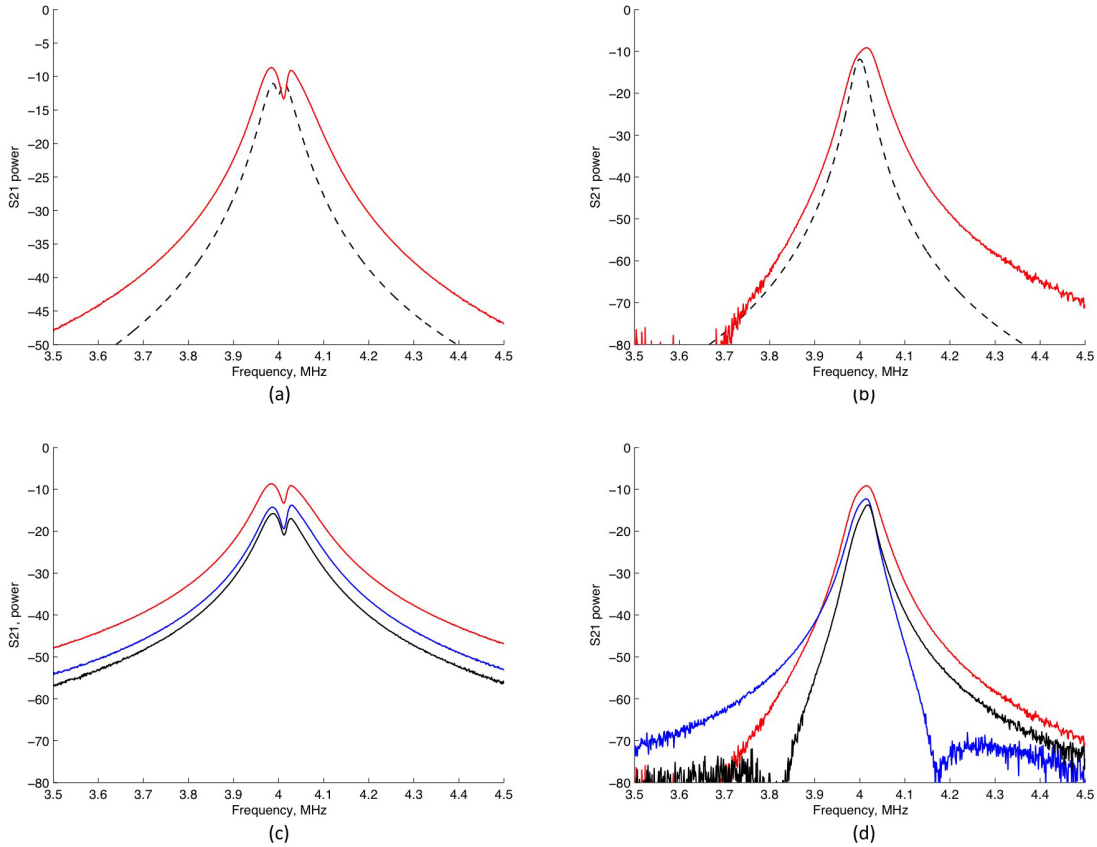

Figure 4.16 Two port measurements of the powering cage for a 50 Ω load. All measurements are taken with the receive coil parallel to the relay or transmit coil. a) Measurement taken with coupling at a maximum to the transmit coil (corner location, see Figure 5.14). Dotted line is the simulation case and red line is the measurement. b) Same as (a), but coupled to the relay coil. c) Measurement comparisons of the a strong coupling position (red), the middle of the cage (blue) and a weak coupling position (black) when coupled to the transmit coil. d) Same as (c), but coupled to the relay coil.

Figure 4.16a and Figure 4.16b show simulation (dotted black trace) S21 response and the measured S21 response (solid red trace) for the receive coil coupling to the transmit and relay coils, respectively. These measurements were made at the optimal coupling location (corner position next to a coil turn). Interestingly, the power transfer is greater across the

measured frequencies, but at 4 MHz, there is a negligible difference. In Figure 4.16c and Figure 4.16d, the coupling at a strong coupling location (red trace), the center of the cage (blue), and a weak coupling location (black trace) are shown for the receive coil coupling to the transmit a relay coil respectively. The maximum PTE of the measurements for a 50 Ω load range from 2.3 to 7%.

4.5.3 Preliminary *in vivo* Validation

Validating the cage with a device requires retuning the system for a complex load. A power management circuit is used to convert AC to DC, store energy, and regulate supply voltages (Figure 4.15c). A two-stage rectifier topology is used to perform AC to DC conversion and a low noise linear dropout regulator provides a 1.8 V supply voltage. The setup is similar to Figure 2.25, but there is only one device and an additional 700 Ω load at the regulator output. From previous design experience with a 1-axis cage and ADS simulation, the rectifier board impedance is known to be 0.78 + j106.9 Ω. Using RCFET simulations for the known rectifier load, the characteristic impedances K-inverter capacitor values are determined and mounted onto the power measurement boards. With a 500 mW input at 4.01 MHz, rectified voltage values range from 1.79- 3.32 V. Assuming 50% rectifier efficiency, this translates into a PTE range of 1.8-6.28% which is in good agreement with the 50 Ω load case.

Preliminary *in vivo* validation is performed in two similar cages and brief recording sessions. Future work will be to pursue validation with longer time periods. The packaged device in Figure 4.15c is implanted subcutaneously in the flank of a rat, and the rat is allowed to roam freely in the cage. The cage switches are operated in an

open-loop configuration and constantly toggled at 200 Hz (Table 4.3). The rectified voltage is reported and shown in Figure 4.17. The rat is visually observed and time points where the rat is moving or is stationary are indicated in red and blue, respectively. As the rat moves, it can be seen that the voltage fluctuates. Critically, the rectified voltage is maintained above the regulator voltage of 1.8V. When the animal is stationary, the rectified voltage can be seen to stable. At the beginning and end of the recording session shown, the animal is in different locations of the cage explaining the difference in rectified voltage.

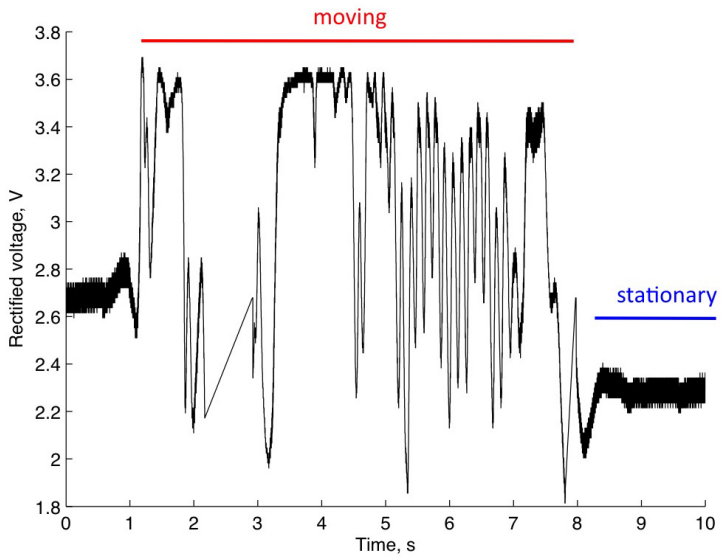

Figure 4.17 Wireless powering in an animal using the three axis RCFET cage. Rectified voltage at the input of the regulator is shown and continuously stays above 1.8 V (regulator voltage). Rectified voltage fluctuates more while the animal is moving than when it is stationary. Power output is 630 mW at 4.11 MHz.

The second data set uses the same device configuration as Figure 2.25. One rectifier board supplies power to two devices for 4 channels of biopotential acquisition. In this cage setup, the optical relay switches are operated in a closed-loop manner. A simple

control algorithm is implemented into the basestation. The basestation both receives data from the devices and toggles the relay coils. The basestation uses a timer that looks for data packets received. If a data packet is not received for 200 ms, indicating a lack of power, then the switching function is initiated. This is preferable to the open-loop case since the open loop switching frequency is in input range of acquisition devices. Noise from switching will be introduced and amplified. More complex control algorithms can be designed for smoother voltage regulation and less packet loss. The recording session is for 4.5 minutes, and the data of interest is the number of data points received. 673770 data points are expected in this time frame and 636940 data points were received indicating a 94.53% of successful data transmission. Additionally, the data suggests that the implanted devices did not restart and the lost packets were due to dropped packets and not powering. This data shows the three-axis RCFET powering cage can reliably deliver power to multiple devices with less than 1 W output power. Further *in vivo* validation with biopotential measurements is required.

4.6 Conclusion

The design methodology and bench top characterization of a three-axis RCFET cage is presented. For a 20 mm diameter receive coil, PTE from 1.8 – 6.28% are achieved. The powering volume is 11 in x 11 in x 11 in and is large enough to house adult rats. Preliminary *in vivo* results are shown, but further chronic work is needed to establish the suitability of the cage for chronic epilepsy and SUDEP experiments.

CHAPTER 5. CONCLUSION

Implantable medical devices are becoming more prominent, and DBS is entering an era of tremendous clinical investigation. Optimization of DBS to control diseases and disorders such as epilepsy, SUDEP, and urinary incontinence will require much laboratory research. Miniature wireless devices are thus poised to greatly enable neuroscience researchers. This dissertation presented a platform of wireless technologies that can be used for biopotential acquisition, electrical stimulation, optical stimulation in optogenetics, and freely behaving wireless powering. To the author's knowledge, Chapter 2 presents the first implantable, miniature closed-loop device for use in chronic epilepsy experiments. Measuring 7 x 14 x 3mm and weighing less than 0.7 g, it is a uniquely small COTS device that can be easily integrated with a wireless powering system and remain implantable. The core recording and stimulating technologies were validated *in vivo*, and it was shown that the device could acquire ECG, respiratory EMG, ECoG, LFP, and bladder pressure reliably. Additionally, the subsystems can be integrated with different combinations to arrive at the desired functionality. For instance, two devices with two channels of biopotential acquisition were connected to a single powering system and simultaneously acquired 4 channels of biopotentials. Chapter 3 presented a miniature, fiber-coupled, deep brain optical stimulator for use in optogenetics. This was one of the earliest demonstrations of wireless deep brain optical stimulation in freely behaving

animals. The device offers programmable stimulation parameters and consumes less than 23 μW during deep sleep operation. The MCU controls the stimulation parameters and as such, the optical module can be integrated with the technologies in Chapter 2 for closed-loop optical stimulation. The device weighs less than 2 g and demonstrated dose-dependent conditioned place preference (CPP) in transgenic mice. Chapter 4 presented the design and characterization of a three-axis RCFET wireless powering cage. This WPT system is unique in that it offers a volume (11 x 11 x11 in^3) of wireless power that can support housing of adult rats. PTE of 1.8-6.28% is achieved, and this can support power for 1 to 2 devices presented in chapter 3. Typically, only 1 W of power is needed and this is below comparable power transfer systems. Further *in vivo* validation is required, but preliminary results are promising. This work is novel in the breadth of technologies presented. Typically, focus is in optimizing a subsystem to achieve particular specifications. In this work, full system design, characterization and integration are demonstrated. To further advance this platform, future work should focus on increased channel counts for acquisition and modulation, integration of all of device technologies into a singular form factor, designing modular powering cages for large behavioral arenas and housing units, and further miniaturization of all implantable technologies.

A foundational premise of engineering is to use physics and technology to better the lives of individuals and societies. This work hopes to contribute to the betterment of the quality of lives of individuals affected by epilepsy, SUDEP, and urinary incontinence.

LIST OF REFERENCES

LIST OF REFERENCES

1. Hodgkin, A. L.; Huxley, A. F. A quantitative description of membrane current and its application to conduction and excitation in nerve. The Journal of Physiology 117(4):500-544; 1952.
2. Hodgkin, A. L.; Huxley, A. F. Measurement of current-voltage relations in the membrane of the giant axon of *Loligo*. The Journal of Physiology 116(4):424-448; 1952.
3. Hodgkin, A. L.; Huxley, A. F. Currents carried by sodium and potassium ions through the membrane of the giant axon of *Loligo*. The Journal of Physiology 116(4):449-472; 1952.
4. Hodgkin, A. L.; Huxley, A. F. The components of membrane conductance in the giant axon of *Loligo*. The Journal of Physiology 116(4):473-496; 1952.
5. Hodgkin, A. L.; Huxley, A. F. The dual effect of membrane potential on sodium conductance in the giant axon of *Loligo*. The Journal of Physiology 116(4):497-506; 1952.
6. Benabid, A. L.; Pollak, P.; Louveau, A.; Henry, S.; de Rougemont, J. Combined (Thalamotomy and Stimulation) Stereotactic Surgery of the VIM Thalamic Nucleus for Bilateral Parkinson Disease. Stereotactic and Functional Neurosurgery 50(1-6):344-346; 1987.
7. Crick, F. The impact of molecular biology on neuroscience. Philosophical transactions of the Royal Society of London. Series B, Biological sciences 354(1392):2021-2025; 1999.
8. Boyden, E. S.; Zhang, F.; Bamberg, E.; Nagel, G.; Deisseroth, K. Millisecond-timescale, genetically targeted optical control of neural activity. Nat Neurosci 8(9):1263-1268; 2005.
9. WHO. World Health Organization: epilepsy: epidemiology, aetiology and prognosis. . WHO Factsheet; 2001b.
10. Benabid, A. L.; Chabardes, S.; Mitrofanis, J.; Pollak, P. Deep brain stimulation of the subthalamic nucleus for the treatment of Parkinson's disease. The Lancet. Neurology 8(1):67-81; 2009.
11. Limousin, P.; Pollak, P.; Benazzouz, A.; Hoffmann, D.; Le Bas, J. F.; Broussolle, E.; Perret, J. E.; Benabid, A. L. Effect of parkinsonian signs and symptoms of bilateral subthalamic nucleus stimulation. Lancet 345(8942):91-95; 1995.
12. Okun, M. S.; Foote, K. D. Parkinson's disease DBS: what, when, who and why? The time has come to tailor DBS targets. Expert review of neurotherapeutics 10(12):1847-1857; 2010.

13. Fisher, R. S.; Velasco, A. L. Electrical brain stimulation for epilepsy. Nature reviews. Neurology 10(5):261-270; 2014.
14. Morrell, M. J. Responsive cortical stimulation for the treatment of medically intractable partial epilepsy. Neurology 77(13):1295-1304; 2011.
15. Fisher, R. S.; Salanova, V.; Witt, T.; Worth, R.; Henry, T.; Gross, R.; Oommen, K.; Osorio, I.; Nazzaro, J.; Labar, D. and others. Electrical stimulation of the anterior nucleus of thalamus for treatment of refractory epilepsy. Epilepsia 51(5):899-908; 2010.
16. Sprengers, M.; Vonck, K.; Carrette, E.; Marson, A. G.; Boon, P. Deep brain and cortical stimulation for epilepsy. The Cochrane database of systematic reviews 6:Cd008497; 2014.
17. Thakor, N. V. Translating the Brain-Machine Interface. Science Translational Medicine 5(210):210ps217; 2013.
18. Borton, D.; Micera, S.; Millan, J. R.; Courtine, G. Personalized Neuroprosthetics. Science Translational Medicine 5(210):210rv212; 2013.
19. Worrell, G. A.; Gardner, A. B.; Stead, S. M.; Hu, S.; Goerss, S.; Cascino, G. J.; Meyer, F. B.; Marsh, R.; Litt, B. High-frequency oscillations in human temporal lobe: simultaneous microwire and clinical macroelectrode recordings. Brain 131(4):928-937; 2008.
20. Viventi, J.; Kim, D.-H.; Vigeland, L.; Frechette, E. S.; Blanco, J. A.; Kim, Y.-S.; Avrin, A. E.; Tiruvadi, V. R.; Hwang, S.-W.; Vanleer, A. C. and others. Flexible, foldable, actively multiplexed, high-density electrode array for mapping brain activity in vivo. Nat Neurosci 14(12):1599-1605; 2011.
21. Schevon, C. A.; Weiss, S. A.; McKhann, G.; Goodman, R. R.; Yuste, R.; Emerson, R. G.; Trevelyan, A. J. Evidence of an inhibitory restraint of seizure activity in humans. Nat Commun 3:1060; 2012.
22. Rousche, P. J.; Normann, R. A. Chronic recording capability of the Utah Intracortical Electrode Array in cat sensory cortex. Journal of Neuroscience Methods 82(1):1-15; 1998.
23. Ward, M. P.; Rajdev, P.; Ellison, C.; Irazoqui, P. P. Toward a comparison of microelectrodes for acute and chronic recordings. Brain Research 1282(0):183-200; 2009.
24. Liu, X.; McCreery, D. B.; Carter, R. R.; Bullara, L. A.; Yuen, T. G. H.; Agnew, W. F. Stability of the interface between neural tissue and chronically implanted intracortical microelectrodes. IEEE Transactions on Rehabilitation Engineering 7(3):315-326; 1999.
25. Williams, J. C.; Rennaker, R. L.; Kipke, D. R. Long-term neural recording characteristics of wire microelectrode arrays implanted in cerebral cortex. Brain Research Protocols 4(3):303-313; 1999.
26. Polikov, V. S.; Tresco, P. A.; Reichert, W. M. Response of brain tissue to chronically implanted neural electrodes. Journal of Neuroscience Methods 148(1):1-18; 2005.
27. Nordhausen, C. T.; Rousche, P. J.; Normann, R. A. Optimizing recording capabilities of the Utah Intracortical Electrode Array. Brain Research 637(1):27-36; 1994.

28. Raghunathan, S.; Gupta, S. K.; Ward, M. P.; Worth, R. M.; Roy, K.; Irazoqui, P. P. The design and hardware implementation of a low-power real-time seizure detection algorithm. Journal of Neural Engineering 6(5):056005; 2009.
29. Raghunathan, S.; Jaitli, A.; Irazoqui, P. P. Multistage seizure detection techniques optimized for low-power hardware platforms. Epilepsy & Behavior 22, Supplement 1(0):S61-S68; 2011.
30. Mormann, F.; Andrzejak, R. G.; Elger, C. E.; Lehnertz, K. Seizure prediction: the long and winding road. Brain 130(Pt 2):314-333; 2007.
31. Osorio, I.; Frei, M. G.; Wilkinson, S. B. Real-time automated detection and quantitative analysis of seizures and short-term prediction of clinical onset. Epilepsia 39:615-627; 1998.
32. Jaroch, D. B.; Ward, M. P.; Chow, E. Y.; Rickus, J. L.; Irazoqui, P. P. Magnetic insertion system for flexible electrode implantation. J Neurosci Methods 183(2):213-222; 2009.
33. Green, R. A.; Lovell, N. H.; Wallace, G. G.; Poole-Warren, L. A. Conducting polymers for neural interfaces: Challenges in developing an effective long-term implant. Biomaterials 29(24,Äì25):3393-3399; 2008.
34. Lo, M. C.; Wang, S.; Singh, S.; Damodaran, V. B.; Kaplan, H. M.; Kohn, J.; Shreiber, D. I.; Zahn, J. D. Coating flexible probes with an ultra fast degrading polymer to aid in tissue insertion. Biomedical microdevices 17(2):34; 2015.
35. Mercanzini, A.; Reddy, S. T.; Velluto, D.; Colin, P.; Maillard, A.; Bensadoun, J. C.; Hubbell, J. A.; Renaud, P. Controlled release nanoparticle-embedded coatings reduce the tissue reaction to neuroprostheses. Journal of controlled release : official journal of the Controlled Release Society 145(3):196-202; 2010.
36. Moser, E.; Mathiesen, I.; Anderson, P. Association between brain temperature and dentate field potentials in exploring and swimming rats. Science 259:1324-1326; 1993.
37. Seese, T. M.; Harasaki, H.; Saidel, G. M.; Davies, C. R. Characterization of tissue morphology, angiogenesis, and temperature in the adaptive response of muscle tissue to chronic heating. Laboratory investigation; a journal of technical methods and pathology 78(12):1553-1562; 1998.
38. Huber, D.; Petreanu, L.; Ghitani, N.; Ranade, S.; Hromadka, T.; Mainen, Z.; Svoboda, K. Sparse optical microstimulation in barrel cortex drives learned behaviour in freely moving mice. Nature 451(7174):61-64; 2008.
39. Iwai, Y.; Honda, S.; Ozeki, H.; Hashimoto, M.; Hirase, H. A simple head-mountable LED device for chronic stimulation of optogenetic molecules in freely moving mice. Neuroscience Research 70(1):124-127; 2011.
40. Wentz, C. T.; et al. A wirelessly powered and controlled device for optical neural control of freely-behaving animals. Journal of Neural Engineering 8(4):046021; 2011.
41. Bernstein, J. G.; Han, X.; Henninger, M. A.; Ko, E. Y.; Qian, X.; Franzesi, G. T.; McConnell, J. P.; Stern, P.; Desimone, R.; Boyden, E. S. Prosthetic systems for therapeutic optical activation and silencing of genetically targeted neurons: SPIE; 2008.

42. Kim, T.-i.; McCall, J. G.; Jung, Y. H.; Huang, X.; Siuda, E. R.; Li, Y.; Song, J.; Song, Y. M.; Pao, H. A.; Kim, R.-H. and others. Injectable, Cellular-Scale Optoelectronics with Applications for Wireless Optogenetics. Science 340(6129):211-216; 2013.
43. Osorio, I.; Frei, M. G.; Wilkinson, S. B. Real-time automated detection and quantitative analysis of seizures and short-term prediction of clinical onset. Epilepsia 39(6):615-627; 1998.
44. Hjorth, B. An on-line transformation of EEG scalp potentials into orthogonal source derivations. Electroencephalography and clinical neurophysiology 39(5):526-530; 1975.
45. Hjorth, B. EEG analysis based on time domain properties. Electroencephalography and clinical neurophysiology 29(3):306-310; 1970.
46. Buzs√°ki, G. r.; Anastassiou, C. A.; Koch, C. The origin of extracellular fields and currents ,Äî EEG, ECoG, LFP and spikes. Nat Rev Neurosci 13(6):407-420; 2012.
47. Petsche, H.; Pockberger, H.; Rappelsberger, P. On the search for the sources of the electroencephalogram. Neuroscience 11(1):1-27; 1984.
48. Rasch, M. J.; Gretton, A.; Murayama, Y.; Maass, W.; Logothetis, N. K. Inferring Spike Trains From Local Field Potentials. Journal of Neurophysiology 99(3):1461-1476; 2008.
49. Navarrete-Opazo, A.; Mitchell, G. S. Recruitment and plasticity in diaphragm, intercostal, and abdominal muscles in unanesthetized rats. Journal of applied physiology (Bethesda, Md. : 1985) 117(2):180-188; 2014.
50. Chandler, D.; Bisasky, J.; Stanislaus, J. L.; Mohsenin, T. Real-time multi-channel seizure detection and analysis hardware. Biomedical Circuits and Systems Conference (BioCAS), 2011 IEEE: IEEE; 2011:41-44.
51. Verma, N.; Shoeb, A.; Bohorquez, J.; Dawson, J.; Guttag, J.; Chandrakasan, A. P. A Micro-Power EEG Acquisition SoC With Integrated Feature Extraction Processor for a Chronic Seizure Detection System. Solid-State Circuits, IEEE Journal of 45(4):804-816; 2010.
52. Salam, M. T.; Mirzaei, M.; Ly, M. S.; Dang Khoa, N.; Sawan, M. An Implantable Closedloop Asynchronous Drug Delivery System for the Treatment of Refractory Epilepsy. Neural Systems and Rehabilitation Engineering, IEEE Transactions on 20(4):432-442; 2012.
53. Pang, C. C.; Upton, A. R.; Shine, G.; Kamath, M. V. A comparison of algorithms for detection of spikes in the electroencephalogram. IEEE Trans Biomed Eng 50(4):521-526; 2003.
54. Raghunathan, S.; Gupta, S. K.; Markandeya, H. S.; Roy, K.; Irazoqui, P. P. A hardware-algorithm co-design approach to optimize seizure detection algorithms for implantable applications. J Neurosci Methods 193(1):106-117; 2010.
55. White, A. M.; Williams, P. A.; Ferraro, D. J.; Clark, S.; Kadam, S. D.; Dudek, F. E.; Staley, K. J. Efficient unsupervised algorithms for the detection of seizures in continuous EEG recordings from rats after brain injury. J Neurosci Methods 152(1-2):255-266; 2006.

56. Harrison, R. R.; Charles, C. A low-power low-noise CMOS amplifier for neural recording applications. Solid-State Circuits, IEEE Journal of 38(6):958-965; 2003.
57. Chen, W.-M.; Chiueh, H.; Chen, T.-J.; Ho, C.-L.; Jeng, C.; Ker, M.-D.; Lin, C.-Y.; Huang, Y.-C.; Chou, C.-W.; Fan, T.-Y. and others. A Fully Integrated 8-Channel Closed-Loop Neural-Prosthetic CMOS SoC for Real-Time Epileptic Seizure Control. Solid-State Circuits, IEEE Journal of 49(1):232-247; 2014.
58. Harrison, R. R. The Design of Integrated Circuits to Observe Brain Activity. Proceedings of the IEEE 96(7):1203-1216; 2008.
59. Harrison, R. R.; Kier, R. J.; Chestek, C. A.; Gilja, V.; Nuyujukian, P.; Ryu, S.; Greger, B.; Solzbacher, F.; Shenoy, K. V. Wireless neural recording with single low-power integrated circuit. IEEE transactions on neural systems and rehabilitation engineering : a publication of the IEEE Engineering in Medicine and Biology Society 17(4):322-329; 2009.
60. Chestek, C. A.; Gilja, V.; Nuyujukian, P.; Kier, R. J.; Solzbacher, F.; Ryu, S. I.; Harrison, R. R.; Shenoy, K. V. HermesC: low-power wireless neural recording system for freely moving primates. IEEE transactions on neural systems and rehabilitation engineering : a publication of the IEEE Engineering in Medicine and Biology Society 17(4):330-338; 2009.
61. Harrison, R. R.; Watkins, P. T.; Kier, R. J.; Lovejoy, R. O.; Black, D. J.; Greger, B.; Solzbacher, F. A Low-Power Integrated Circuit for a Wireless 100-Electrode Neural Recording System. Solid-State Circuits, IEEE Journal of 42(1):123-133; 2007.
62. Fan, D.; Rich, D.; Holtzman, T.; Ruther, P.; Dalley, J. W.; Lopez, A.; Rossi, M. A.; Barter, J. W.; Salas-Meza, D.; Herwik, S. and others. A Wireless Multi-Channel Recording System for Freely Behaving Mice and Rats. PLoS ONE 6(7):e22033; 2011.
63. Szuts, T. A.; Fadeyev, V.; Kachiguine, S.; Sher, A.; Grivich, M. V.; Agrochao, M.; Hottowy, P.; Dabrowski, W.; Lubenov, E. V.; Siapas, A. G. and others. A wireless multi-channel neural amplifier for freely moving animals. Nat Neurosci 14(2):263-269; 2011.
64. Systems, M. T. Implantable Telemetry Systems. 2015.
65. International, D. S. Implantable Telemetry. 2015.
66. Liang, S.-F.; Liao, Y.-C.; Shaw, F.-Z.; Chang, D.-W.; Young, C.-P.; Chiueh, H. Closed-loop seizure control on epileptic rat models. Journal of Neural Engineering 8(4):045001; 2011.
67. Ball, D.; Kliese, R.; Windels, F.; Nolan, C.; Stratton, P.; Sah, P.; Wiles, J. Rodent Scope: A User-Configurable Digital Wireless Telemetry System for Freely Behaving Animals. PLoS ONE 9(2):e89949; 2014.
68. Jobst, B. C.; Darcey, T. M.; Thadani, V. M.; Roberts, D. W. Brain stimulation for the treatment of epilepsy. Epilepsia 51 Suppl 3:88-92; 2010.
69. Merrill, D. R.; Bikson, M.; Jefferys, J. G. Electrical stimulation of excitable tissue: design of efficacious and safe protocols. J Neurosci Methods 141(2):171-198; 2005.

70. Wyckhuys, T.; Raedt, R.; Vonck, K.; Wadman, W.; Boon, P. Comparison of hippocampal Deep Brain Stimulation with high (130Hz) and low frequency (5Hz) on afterdischarges in kindled rats. Epilepsy Res 88(2-3):239-246; 2010.
71. Mirski, M. A.; Rossell, L. A.; Terry, J. B.; Fisher, R. S. Anticonvulsant effect of anterior thalamic high frequency electrical stimulation in the rat. Epilepsy research 28(2):89-100; 1997.
72. Rashid, S.; Pho, G.; Czigler, M.; Werz, M. A.; Durand, D. M. Low frequency stimulation of ventral hippocampal commissures reduces seizures in a rat model of chronic temporal lobe epilepsy. Epilepsia 53(1):147-156; 2012.
73. Lado, F. A. Chronic bilateral stimulation of the anterior thalamus of kainate-treated rats increases seizure frequency. Epilepsia 47(1):27-32; 2006.
74. Covolan, L.; de Almeida, A. C.; Amorim, B.; Cavarsan, C.; Miranda, M. F.; Aarao, M. C.; Madureira, A. P.; Rodrigues, A. M.; Nobrega, J. N.; Mello, L. E. and others. Effects of anterior thalamic nucleus deep brain stimulation in chronic epileptic rats. PLoS One 9(6):e97618; 2014.
75. Jiruska, P.; Powell, A. D.; Deans, J. K.; Jefferys, J. G. Effects of direct brain stimulation depend on seizure dynamics. Epilepsia 51 Suppl 3:93-97; 2010.
76. Rajdev, P.; Ward, M.; Irazoqui, P. Effect of stimulus parameters in the treatment of seizures by electrical stimulation in the kainate animal model. Int J Neural Syst 21(2):151-162; 2011.
77. Mangubat, E. Z.; Kellogg, R. G.; Harris, T. J., Jr.; Rossi, M. A. On-demand pulsatile intracerebral delivery of carisbamate with closed-loop direct neurostimulation therapy in an electrically induced self-sustained focal-onset epilepsy rat model. J Neurosurg:1-10; 2015.
78. Ewing, S. G.; Lipski, W. J.; Grace, A. A.; Winter, C. An inexpensive, charge-balanced rodent deep brain stimulation device: A step-by-step guide to its procurement and construction. Journal of Neuroscience Methods 219(2):324-330; 2013.
79. Forni, C.; Mainard, O.; Melon, C.; Goguenheim, D.; Kerkerian-Le Goff, L.; Salin, P. Portable microstimulator for chronic deep brain stimulation in freely moving rats. J Neurosci Methods 209(1):50-57; 2012.
80. Ewing, S. G.; Porr, B.; Riddell, J.; Winter, C.; Grace, A. A. SaBer DBS: a fully programmable, rechargeable, bilateral, charge-balanced preclinical microstimulator for long-term neural stimulation. J Neurosci Methods 213(2):228-235; 2013.
81. de Haas, R.; Struikmans, R.; van der Plasse, G.; van Kerkhof, L.; Brakkee, J. H.; Kas, M. J. H.; Westenberg, H. G. M. Wireless implantable micro-stimulation device for high frequency bilateral deep brain stimulation in freely moving mice. Journal of Neuroscience Methods 209(1):113-119; 2012.
82. Millard, R. E.; Shepherd, R. K. A fully implantable stimulator for use in small laboratory animals. Journal of neuroscience methods 166(2):168-177; 2007.
83. Liu, H. Y.; Jin, J.; Tang, J. S.; Sun, W. X.; Jia, H.; Yang, X. P.; Cui, J. M.; Wang, C. G. Chronic deep brain stimulation in the rat nucleus accumbens and its effect on morphine reinforcement. Addiction biology 13(1):40-46; 2008.

84. Harnack, D.; Meissner, W.; Paulat, R.; Hilgenfeld, H.; Muller, W. D.; Winter, C.; Morgenstern, R.; Kupsch, A. Continuous high-frequency stimulation in freely moving rats: development of an implantable microstimulation system. J Neurosci Methods 167(2):278-291; 2008.
85. Krook-Magnuson, E.; Armstrong, C.; Oijala, M.; Soltesz, I. On-demand optogenetic control of spontaneous seizures in temporal lobe epilepsy. Nat Commun 4:1376; 2013.
86. Bamann, C.; Nagel, G.; Bamberg, E. Microbial rhodopsins in the spotlight. Current Opinion in Neurobiology 20(5):610-616; 2010.
87. Nagel, G.; Szellas, T.; Huhn, W.; Kateriya, S.; Adeishvili, N.; Berthold, P.; Ollig, D.; Hegemann, P.; Bamberg, E. Channelrhodopsin-2, a directly light-gated cation-selective membrane channel. Proceedings of the National Academy of Sciences 100(24):13940-13945; 2003.
88. Nagel, G.; Ollig, D.; Fuhrmann, M.; Kateriya, S.; Musti, A. M.; Bamberg, E.; Hegemann, P. Channelrhodopsin-1: A Light-Gated Proton Channel in Green Algae. Science 296(5577):2395-2398; 2002.
89. Zhang, F.; Wang, L.-P.; Boyden, E. S.; Deisseroth, K. Channelrhodopsin-2 and optical control of excitable cells. Nat Meth 3(10):785-792; 2006.
90. Nagel, G.; Brauner, M.; Liewald, J. F.; Adeishvili, N.; Bamberg, E.; Gottschalk, A. Light Activation of Channelrhodopsin-2 in Excitable Cells of Caenorhabditis elegans Triggers Rapid Behavioral Responses. Current biology : CB 15(24):2279-2284; 2005.
91. Han, X.; Boyden, E. S. Multiple-Color Optical Activation, Silencing, and Desynchronization of Neural Activity, with Single-Spike Temporal Resolution. PLoS ONE 2(3):e299; 2007.
92. Gradinaru, V.; Thompson, K.; Deisseroth, K. eNpHR: a Natronomonas halorhodopsin enhanced for optogenetic applications. Brain Cell Biology 36(1):129-139; 2008.
93. Han, X.; Chow, B. Y.; Zhou, H.; Klapoetke, N. C.; Chuong, A.; Rajimehr, R.; Yang, A.; Baratta, M. V.; Winkle, J.; Desimone, R. and others. A high-light sensitivity optical neural silencer: development, and application to optogenetic control of nonhuman primate cortex. Frontiers in Systems Neuroscience 5; 2011.
94. Knopfel, T.; Lin, M. Z.; Levskaya, A.; Tian, L.; Lin, J. Y.; Boyden, E. S. Toward the Second Generation of Optogenetic Tools. The Journal of Neuroscience 30(45):14998-15004; 2010.
95. Gradinaru, V.; Zhang, F.; Ramakrishnan, C.; Mattis, J.; Prakash, R.; Diester, I.; Goshen, I.; Thompson, K. R.; Deisseroth, K. Molecular and Cellular Approaches for Diversifying and Extending Optogenetics. Cell 141(1):154-165; 2010.
96. Yizhar, O.; Fenno, L. E.; Davidson, T. J.; Mogri, M.; Deisseroth, K. Optogenetics in Neural Systems. Neuron 71(1):9-34; 2011.

97. Alivisatos, A. P.; Andrews Am Fau - Boyden, E. S.; Boyden Es Fau - Chun, M.; Chun M Fau - Church, G. M.; Church Gm Fau - Deisseroth, K.; Deisseroth K Fau - Donoghue, J. P.; Donoghue Jp Fau - Fraser, S. E.; Fraser Se Fau - Lippincott-Schwartz, J.; Lippincott-Schwartz J Fau - Looger, L. L.; Looger Ll Fau - Masmanidis, S. and others. Nanotools for neuroscience and brain activity mapping. (1936-086X (Electronic)).
98. Zhang, F.; Gradinaru, V.; Adamantidis, A. R.; Durand, R.; Airan, R. D.; de Lecea, L.; Deisseroth, K. Optogenetic interrogation of neural circuits: technology for probing mammalian brain structures. Nat. Protocols 5(3):439-456; 2010.
99. Campagnola, L.; Wang, H.; Zylka, M. J. Fiber-coupled light-emitting diode for localized photostimulation of neurons expressing channelrhodopsin-2. Journal of Neuroscience Methods 169(1):27-33; 2008.
100. Tuchin, V. V. Light scattering study of tissues. Physics-Uspekhi 40(5):495; 1997.
101. Albeanu, D. F.; Soucy, E.; Sato, T. F.; Meister, M.; Murthy, V. N. LED Arrays as Cost Effective and Efficient Light Sources for Widefield Microscopy. PLoS ONE 3(5):e2146; 2008.
102. Veledar, O.; et al. Simple techniques for generating nanosecond blue light pulses from light emitting diodes. Measurement Science and Technology 18(1):131; 2007.
103. Murat, H. s.; Smet, H. D.; Cuypers, D. Compact LED projector with tapered light pipes for moderate light output applications. Displays 27(3):117-123; 2006.
104. Cardin, J. A.; Carlen, M.; Meletis, K.; Knoblich, U.; Zhang, F.; Deisseroth, K.; Tsai, L.-H.; Moore, C. I. Targeted optogenetic stimulation and recording of neurons in vivo using cell-type-specific expression of Channelrhodopsin-2. Nat. Protocols 5(2):247-254; 2010.
105. Golan, L.; et al. Design and characteristics of holographic neural photo-stimulation systems. Journal of Neural Engineering 6(6):066004; 2009.
106. CREE. XThin LEDs. 2011.
107. Aravanis, A. M.; et al. An optical neural interface: in vivo control of rodent motor cortex with integrated fiberoptic and optogenetic technology. Journal of Neural Engineering 4(3):S143; 2007.
108. Prahl, S. A.; Keijzer, M.; Jacques, S. L.; Welch, A. J. A Monte Carlo model of light propagation in tissue. Dosimetry of Laser Radiation in Medicine Biology IS 5:102-111; 1989.
109. Deisseroth, K. Predicted irradiance values: model based on direct measurements in mammalian brain tissue. 2011.
110. Paralikar, K.; Peng, C.; Yizhar, O.; Fenno, L. E.; Santa, W.; Nielsen, C.; Dinsmoor, D.; Hocken, B.; Munns, G. O.; Giftakis, J. and others. An Implantable Optical Stimulation Delivery System for Actuating an Excitable Biosubstrate. Solid-State Circuits, IEEE Journal of 46(1):321-332; 2011.
111. Hashimoto, M.; Hata, A.; Miyata, T.; Hirase, H. Programmable wireless light-emitting diode stimulator for chronic stimulation of optogenetic molecules in freely moving mice. NEUROW 1(1):011002-011002; 2014.

112. Tsai, H.; Zhang, F.; Adamantidis, A.; Stuber, G.; Bonci, A.; de Lecea, L.; Deisseroth, K. Phasic firing in dopaminergic neurons is sufficient for behavioral conditioning. Science 324(5930):1080-1084; 2009.
113. Boulnois, J.-L. Photophysical processes in recent medical laser developments: A review. Lasers in Medical Science 1(1):47-66; 1986.
114. Peng, Q.; et al. Lasers in medicine. Reports on Progress in Physics 71(5):056701; 2008.
115. Paz, J. T.; Davidson, T. J.; Frechette, E. S.; Delord, B.; Parada, I.; Peng, K.; Deisseroth, K.; Huguenard, J. R. Closed-loop optogenetic control of thalamus as a tool for interrupting seizures after cortical injury. Nat Neurosci 16(1):64-70; 2013.
116. Brown, W. C. The History of Power Transmission by Radio Waves. Microwave Theory and Techniques, IEEE Transactions on 32(9):1230-1242; 1984.
117. Commission, F. C. Part 15--Radio Freqeuncy Devices. In: FCC, ed.; 2014.
118. Lenaerts, B.; Puers, R. Biological Tissue Interaction. Omnidirectional Inductive Powering for Biomedical Implants: Springer Netherlands; 2009:139-150.
119. Schwan, H. P.; Foster, K. R. RF-field interactions with biological systems: Electrical properties and biophysical mechanisms. Proceedings of the IEEE 68(1):104-113; 1980.
120. Bercich, R. A.; Duffy, D. R.; Irazoqui, P. P. Far-field RF powering of implantable devices: safety considerations. IEEE transactions on bio-medical engineering 60(8):2107-2112; 2013.
121. Sanghoek, K.; Ho, J. S.; Poon, A. S. Y. Wireless Power Transfer to Miniature Implants: Transmitter Optimization. Antennas and Propagation, IEEE Transactions on 60(10):4838-4845; 2012.
122. Ho, J. S.; Yeh, A. J.; Neofytou, E.; Kim, S.; Tanabe, Y.; Patlolla, B.; Beygui, R. E.; Poon, A. S. Wireless power transfer to deep-tissue microimplants. Proc Natl Acad Sci U S A 111(22):7974-7979; 2014.
123. Ricketts, D. S.; Chabalko, M. J.; Hillenius, A. Experimental demonstration of the equivalence of inductive and strongly coupled magnetic resonance wireless power transfer. Applied Physics Letters 102(5):053904; 2013.
124. Ozeki, T.; Chinzei, T.; Abe, Y.; Saito, I.; Isoyama, T.; Mochizuki, S.; Ishimaru, M.; Takiura, K.; Baba, A.; Toyama, T. and others. Functions for detecting malposition of transcutaneous energy transmission coils. ASAIO journal (American Society for Artificial Internal Organs : 1992) 49(4):469-474; 2003.
125. Donaldson, N. D.; Perkins, T. A. Analysis of resonant coupled coils in the design of radio frequency transcutaneous links. Med Biol Eng Comput 21(5):612-627; 1983.
126. El-Banayosy, A.; Arusoglu, L.; Kizner, L.; Morshuis, M.; Tenderich, G.; Pae, W. E., Jr.; Korfer, R. Preliminary experience with the LionHeart left ventricular assist device in patients with end-stage heart failure. The Annals of thoracic surgery 75(5):1469-1475; 2003.
127. Mizannojehdehi, A.; Shams, M.; Mussivand, T. Design and Analysis of A Class-E Frequency-Controlled Transcutaneous Energy Transfer System. Electronics, Circuits and Systems, 2006. ICECS '06. 13th IEEE International Conference on; 2006:21-24.

128. Qiuting, H.; Oberle, M. A 0.5-mW passive telemetry IC for biomedical applications. Solid-State Circuits, IEEE Journal of 33(7):937-946; 1998.
129. Chevalerias, O.; O'Donnell, T.; Power, D.; O'Donovan, N.; Duffy, G.; Grant, G.; O'Mathuna, S. C. Inductive telemetry of multiple sensor modules. Pervasive Computing, IEEE 4(1):46-52; 2005.
130. DeHennis, A. D.; Wise, K. D. A wireless microsystem for the remote sensing of pressure, temperature, and relative humidity. Microelectromechanical Systems, Journal of 14(1):12-22; 2005.
131. Harrison, R. R. Designing Efficient Inductive Power Links for Implantable Devices. Circuits and Systems, 2007. ISCAS 2007. IEEE International Symposium on; 2007:2080-2083.
132. Uei-Ming, J.; McMenamin, P.; Kiani, M.; Manns, J. R.; Ghovanloo, M. EnerCage: A Smart Experimental Arena With Scalable Architecture for Behavioral Experiments. Biomedical Engineering, IEEE Transactions on 61(1):139-148; 2014.
133. Yakovlev, A.; Sanghoek, K.; Poon, A. Implantable biomedical devices: Wireless powering and communication. Communications Magazine, IEEE 50(4):152-159; 2012.
134. Yeh, A. J.; Ho, J. S.; Tanabe, Y.; Neofytou, E.; Beygui, R. E.; Poon, A. S. Y. Wirelessly powering miniature implants for optogenetic stimulation. Applied Physics Letters 103(16):163701; 2013.
135. Popovic, Z. Cut the Cord: Low-Power Far-Field Wireless Powering. Microwave Magazine, IEEE 14(2):55-62; 2013.
136. Kurs, A.; Karalis, A.; Moffatt, R.; Joannopoulos, J. D.; Fisher, P.; Soljačić, M. Wireless Power Transfer via Strongly Coupled Magnetic Resonances. Science 317(5834):83-86; 2007.
137. Wei, X.; Wang, Z.; Dai, H. A Critical Review of Wireless Power Transfer via Strongly Coupled Magnetic Resonances. Energies 7(7):4316-4341; 2014.
138. Cannon, B. L.; Hoburg, J. F.; Stancil, D. D.; Goldstein, S. C. Magnetic Resonant Coupling As a Potential Means for Wireless Power Transfer to Multiple Small Receivers. Power Electronics, IEEE Transactions on 24(7):1819-1825; 2009.
139. Waters, B. H.; Sample, A. P.; Bonde, P.; Smith, J. R. Powering a Ventricular Assist Device (VAD) With the Free-Range Resonant Electrical Energy Delivery (FREE-D) System. Proceedings of the IEEE 100(1):138-149; 2012.
140. Waters, B. H.; Smith, J. R.; Bonde, P. Innovative Free-range Resonant Electrical Energy Delivery system (FREE-D System) for a ventricular assist device using wireless power. ASAIO journal (American Society for Artificial Internal Organs : 1992) 60(1):31-37; 2014.
141. Qi, X.; Hao, W.; Zhaolong, G.; Zhi-Hong, M.; Jiping, H.; Mingui, S. A Novel Mat-Based System for Position-Varying Wireless Power Transfer to Biomedical Implants. Magnetics, IEEE Transactions on 49(8):4774-4779; 2013.
142. Awai, I. Design theory of wireless power transfer system based on magnetically coupled resonators. Wireless Information Technology and Systems (ICWITS), 2010 IEEE International Conference on; 2010:1-4.

143. Awai, I.; Komori, T. A Simple and versatile design method of resonator-coupled wireless power transfer system. Communications, Circuits and Systems (ICCCAS), 2010 International Conference on; 2010:616-620.
144. Juseop, L.; Yong-Seok, L.; Woo-Jin, Y.; Seung-Ok, L. Wireless Power Transfer System Adaptive to Change in Coil Separation. Antennas and Propagation, IEEE Transactions on 62(2):889-897; 2014.
145. Juseop, L.; Yongseok, L.; Hyunseok, A.; Jae-Du, Y.; Seung-Ok, L. Impedance-Matched Wireless Power Transfer Systems Using an Arbitrary Number of Coils With Flexible Coil Positioning. Antennas and Wireless Propagation Letters, IEEE 13:1207-1210; 2014.
146. Koh Kim, E.; Beh Teck, C.; Imura, T.; Hori, Y. Novel band-pass filter model for multi-receiver wireless power transfer via magnetic resonance coupling and power division. Wireless and Microwave Technology Conference (WAMICON), 2012 IEEE 13th Annual; 2012:1-6.
147. Mei, H.; Ha, D.; Kim, Y.; Chappell, W. J.; Irazoqui, P. Resonantly Coupled Filter Energy Transfer: Model, Analysis, and Tuning. Purdue University; 2015.
148. French, J. A. Refractory Epilepsy: Clinical Overview. Epilepsia 48:3-7; 2007.
149. Guidelines for Epidemiologic Studies on Epilepsy. Epilepsia 34(4):592-596; 1993.
150. Banerjee, P. N.; Filippi, D.; Allen Hauser, W. The descriptive epidemiology of epilepsy,ÄîA review. Epilepsy Research 85(1):31-45; 2009.
151. Epilepsy, C. Epilepsy Facts. 2011.
152. McNamara, J. O.; Huang, Y. Z.; Leonard, A. S. Molecular Signaling Mechanisms Underlying Epileptogenesis. Sci. STKE 2006(356):re12-; 2006.
153. Albowitz, B.; Kuhnt, U. Spread of epileptiform potentials in the neocortical slice: recordings with voltage-sensitive dyes. Brain Research 631(2):329-333; 1993.
154. Fisher, R.; Salanova, V.; Witt, T.; Worth, R.; Henry, T.; Gross, R.; Oommen, K.; Osorio, I.; Nazzaro, J.; Labar, D. and others. Electrical stimulation of the anterior nucleus of thalamus for treatment of refractory epilepsy. Epilepsia 51(5):899-908; 2010.
155. Englot, D. J.; Chang, E. F.; Auguste, K. I. Vagus nerve stimulation for epilepsy: a meta-analysis of efficacy and predictors of response. Journal of Neurosurgery 115(6):1248-1255; 2011.
156. Morrell, M. J. Responsive cortical stimulation for the treatment of medically intractable partial epilepsy. Neurology 77; 2011.
157. McCreery, D. B.; Yuen, T. G. H.; Agnew, W. F.; Bullara, L. A. A characterization of the effects on neuronal excitability due to prolonged microstimulation with chronically implanted microelectrodes. IEEE Transactions on Biomedical Engineering 44(10):931-939; 1997.
158. Ficker, D. M.; So, E. L.; Shen, W. K.; Annegers, J. F.; O'Brien, P. C.; Cascino, G. D.; Belau, P. G. Population-based study of the incidence of sudden unexplained death in epilepsy. Neurology 51(5):1270-1274; 1998.
159. Nashef, L.; So, E. L.; Ryvlin, P.; Tomson, T. Unifying the definitions of sudden unexpected death in epilepsy. Epilepsia 53(2):227-233; 2012.

160. So, E. L. What is known about the mechanisms underlying SUDEP? Epilepsia 49 Suppl 9:93-98; 2008.
161. Surges, R.; Sander, J. W. Sudden unexpected death in epilepsy: mechanisms, prevalence, and prevention. Current opinion in neurology 25(2):201-207; 2012.
162. Massey, C. A.; Sowers, L. P.; Dlouhy, B. J.; Richerson, G. B. Mechanisms of sudden unexpected death in epilepsy: the pathway to prevention. Nat Rev Neurol 10(5):271-282; 2014.
163. Nei, M.; Ho, R. T.; Abou-Khalil, B. W.; Drislane, F. W.; Liporace, J.; Romeo, A.; Sperling, M. R. EEG and ECG in sudden unexplained death in epilepsy. Epilepsia 45(4):338-345; 2004.
164. Zijlmans, M.; Flanagan, D.; Gotman, J. Heart rate changes and ECG abnormalities during epileptic seizures: prevalence and definition of an objective clinical sign. Epilepsia 43(8):847-854; 2002.
165. Nashef, L.; Walker, F.; Allen, P.; Sander, J. W.; Shorvon, S. D.; Fish, D. R. Apnoea and bradycardia during epileptic seizures: relation to sudden death in epilepsy. Journal of neurology, neurosurgery, and psychiatry 60(3):297-300; 1996.
166. Venit, E. L.; Shepard, B. D.; Seyfried, T. N. Oxygenation prevents sudden death in seizure-prone mice. Epilepsia 45(8):993-996; 2004.
167. Kalume, F.; Westenbroek, R. E.; Cheah, C. S.; Yu, F. H.; Oakley, J. C.; Scheuer, T.; Catterall, W. A. Sudden unexpected death in a mouse model of Dravet syndrome. The Journal of Clinical Investigation 123(4):1798-1808; 2013.
168. Schachter, S. C. Therapeutic effects of vagus nerve stimulation in epilepsy and implications for sudden unexpected death in epilepsy. Clinical autonomic research : official journal of the Clinical Autonomic Research Society 16(1):29-32; 2006.
169. Langan, Y.; Nashef, L.; Sander, J. W. Case-control study of SUDEP. Neurology 64(7):1131-1133; 2005.
170. Lathers, C. M.; Schraeder, P. L. Review of autonomic dysfunction, cardiac arrhythmias, and epileptogenic activity. Journal of clinical pharmacology 27(5):346-356; 1987.
171. Wulsin, L. R.; Horn, P. S.; Perry, J. L.; Massaro, J.; D'Agostino, R. Autonomic Imbalance as a Predictor of Metabolic Risks, Cardiovascular Disease, Diabetes, and Mortality Autonomic Imbalance Predicts CVD, DM, Mortality. The Journal of clinical endocrinology and metabolism:jc20144123; 2015.
172. Wu, J. M.; Vaughan, C. P.; Goode, P. S.; Redden, D. T.; Burgio, K. L.; Richter, H. E.; Markland, A. D. Prevalence and trends of symptomatic pelvic floor disorders in U.S. women. Obstetrics and gynecology 123(1):141-148; 2014.
173. Shamliyan, T. A.; Wyman, J. F.; Ping, R.; Wilt, T. J.; Kane, R. L. Male Urinary Incontinence: Prevalence, Risk Factors, and Preventive Interventions. Reviews in Urology 11(3):145-165; 2009.
174. Green, A. L.; Stone, E.; Sitsapesan, H.; Turney, B. W.; Coote, J. H.; Aziz, T. Z.; Hyam, J. A.; Lovick, T. A. Switching off micturition using deep brain stimulation at midbrain sites. Annals of neurology 72(1):144-147; 2012.
175. Webster, J. , 4th ed: John Wiley & Sons, Inc.; 2010.

176. Moro, E.; Esselink, R. J. A.; Xie, J.; Hommel, M.; Benabid, A. L.; Pollak, P. The impact on Parkinson's disease of electrical parameter settings in STN stimulation. Neurology 59(5):706-713; 2002.
177. Ward, M. Peripheral Nerve Interface Applications: Vagal Nerve Stimulation. In: Jaeger, D.; Jung, R., eds. Encyclopedia of Computational Neuroscience: Springer New York; 2014:1-4.
178. Yazicioglu, R. F.; van Hoff, C.; Puers, R. Biopotential Readout Circuits for Portable Acquisition Systems, 1 ed: Springer Netherlands; 2009.
179. Merletti, R.; Farina, D. Analysis of intramuscular electromyogram signals; 2009.
180. Thakor, N. V.; Webster, J. G. Ground-free ECG recording with two electrodes. IEEE transactions on bio-medical engineering 27(12):699-704; 1980.
181. Stacey, W. C.; Kellis, S.; Patel, P. R.; Greger, B.; Butson, C. R. Signal distortion from microelectrodes in clinical EEG acquisition systems. Journal of neural engineering 9(5):056007-056007; 2012.
182. Prasad, A.; Sanchez, J. C. Quantifying long-term microelectrode array functionality using chronic in vivo impedance testing. J Neural Eng 9(2):026028; 2012.
183. Geddes, L. A.; Baker, L. E.; McGoodwin, M. The relationship between electrode area and amplifier input impedance in recording muscle action potentials. Med. & biol. Engng. 5(6):561-569; 1967.
184. Instruments, T. Micro-Power, Zero-Drift, Rail-to-Rail Out Instrumentation Amplifier. Texas Instruments Incorporated; 2008.
185. Pallás-Areny, R.; Webster, J. G. Analog Signal Processing: Wiley; 1999.
186. Huhta, J. C.; Webster, J. G. 60-Hz Interference in Electrocardiography. Biomedical Engineering, IEEE Transactions on BME-20(2):91-101; 1973.
187. Geddes, L. A.; Baker, L. E. Principles of Applied Biomedical Instrumentation, Third ed: Wiley; 1989.
188. Kitchin, C.; Counts, L.; Gerstenhaber, M. Reducing rfi rectification errors in in-amp circuits.
189. Ott, H. W.; Ott, H. W. Noise reduction techniques in electronic systems: Wiley New York; 1988.
190. Liu, X.; Demosthenous, A.; Donaldson, N. An integrated implantable stimulator that is fail-safe without off-chip blocking-capacitors. Biomedical Circuits and Systems, IEEE Transactions on 2(3):231-244; 2008.
191. Liu, X.; Demosthenous, A.; Donaldson, N. Five valuable functions of blocking capacitors in stimulators. Biomed Techn (Suppl 1):322-324; 2008.
192. Sit, J.-J.; Sarpeshkar, R. A low-power blocking-capacitor-free charge-balanced electrode-stimulator chip with less than 6 nA DC error for 1-mA full-scale stimulation. Biomedical Circuits and Systems, IEEE Transactions on 1(3):172-183; 2007.
193. Butson, C. R.; Maks, C. B.; McIntyre, C. C. Sources and effects of electrode impedance during deep brain stimulation. Clinical neurophysiology : official journal of the International Federation of Clinical Neurophysiology 117(2):447-454; 2006.

194. Semiconductor, N. nRF51822 Product Specification v3.1. In: Semiconductor, N., ed.; 2015.
195. Maggi, C. A.; Meli, A. Suitability of urethane anesthesia for physiopharmacological investigations in various systems. Part 2: Cardiovascular system. Experientia 42(3):292-297; 1986.
196. Field, K. J.; White, W. J.; Lang, C. M. Anaesthetic effects of chloral hydrate, pentobarbitone and urethane in adult male rats. Laboratory animals 27(3):258-269; 1993.
197. Megirian, D.; Pollard, M.; Sherrey, J. The labile respiratory activity of ribcage muscles of the rat during sleep. The Journal of physiology 389(1):99-110; 1987.
198. Entz, L.; Toth, E.; Keller, C. J.; Bickel, S.; Groppe, D. M.; Fabo, D.; Kozak, L. R.; Eross, L.; Ulbert, I.; Mehta, A. D. Evoked effective connectivity of the human neocortex. Human brain mapping 35(12):5736-5753; 2014.
199. Dalgleish, T. The emotional brain. Nat Rev Neurosci 5(7):583-589; 2004.
200. Lee, S.; Williams, P.; Braine, C.; Lin, D. T.; John, S.; Irazoqui, P. A Miniature, Fiber-Coupled, Wireless, Deep-Brain Optogenetic Stimulator. IEEE transactions on neural systems and rehabilitation engineering : a publication of the IEEE Engineering in Medicine and Biology Society; 2015. © 2015 IEEE. Reprinted, with permission.
201. Gradinaru, V.; Mogri, M.; Thompson, K. R.; Henderson, J. M.; Deisseroth, K. Optical Deconstruction of Parkinsonian Neural Circuitry. Science 324(5925):354-359; 2009.
202. Deisseroth, K.; Feng, G.; Majewska, A. K.; Miesenb√∂ck, G.; Ting, A.; Schnitzer, M. J. Next-Generation Optical Technologies for Illuminating Genetically Targeted Brain Circuits. The Journal of Neuroscience 26(41):10380-10386; 2006.
203. Famm, K.; Litt, B.; Tracey, K. J.; Boyden, E. S.; Slaoui, M. Drug discovery: A jump-start for electroceuticals. Nature 496(7444):159-161; 2013.
204. Jego, S.; Glasgow, S. D.; Herrera, C. G.; Ekstrand, M.; Reed, S. J.; Boyce, R.; Friedman, J.; Burdakov, D.; Adamantidis, A. R. Optogenetic identification of a rapid eye movement sleep modulatory circuit in the hypothalamus. Nat Neurosci 16(11):1637-1643; 2013.
205. Hudson, M. C. Calculation of the Maximum Optical Coupling Efficiency into Multimode Optical Waveguides. Applied Optics 13(5):1029-1033; 1974.
206. Cunningham, C. L.; Gremel, C. M.; Groblewski, P. A. Drug-induced conditioned place preference and aversion in mice. Nat. Protocols 1(4):1662-1670; 2006.
207. Chow, E. Y.; Chin-Lung, Y.; Yuehui, O.; Chlebowski, A. L.; Irazoqui, P. P.; Chappell, W. J. Wireless Powering and the Study of RF Propagation Through Ocular Tissue for Development of Implantable Sensors. Antennas and Propagation, IEEE Transactions on 59(6):2379-2387; 2011.
208. Ferguson, B. S.; Hoggarth, D. A.; Maliniak, D.; Ploense, K.; White, R. J.; Woodward, N.; Hsieh, K.; Bonham, A. J.; Eisenstein, M.; Kippin, T. E. and others. Real-Time, Aptamer-Based Tracking of Circulating Therapeutic Agents in Living Animals. Science Translational Medicine 5(213):213ra165; 2013.
209. Friis, H. T. A Note on a Simple Transmission Formula. Proceedings of the IRE 34(5):254-256; 1946.

210. Paxinos, G.; Franklin, K. B. The Mouse Brain in Stereotaxic Coordinates, Second ed. San Diego: Elsevier Science; 2003.
211. Chetkovich, D. M.; Bunn, R. C.; Kuo, S.-H.; Kawasaki, Y.; Kohwi, M.; Bredt, D. S. Postsynaptic Targeting of Alternative Postsynaptic Density-95 Isoforms by Distinct Mechanisms. The Journal of Neuroscience 22(15):6415-6425; 2002.
212. Sample, A. P.; Meyer, D. A.; Smith, J. R. Analysis, experimental results, and range adaptation of magnetically coupled resonators for wireless power transfer. IEEE Transactions on Industrial Electronics 58(2):544-554; 2011.
213. Matthaei, G. L.; Young, L.; Jones, E. M. T. Microwave filters, impedance-matching networks, and coupling structures: McGraw-Hill; 1964.
214. Cameron, R. J.; Mansour, R.; Kudsia, C. M. Microwave Filters for Communication Systems: Fundamentals, Design and Applications: Wiley; 2007.
215. Awai, I.; Ishida, T. Design of resonator-coupled wireless power transfer system by use of BPF theory. Journal of Electromagnetic Engineering And Science 10(4):237-243; 2010.
216. Bosshard, R.; Muhlethaler, J.; Kolar, J.; Stevanovic, I. Optimized magnetic design for inductive power transfer coils. Applied Power Electronics Conference and Exposition (APEC), 2013 Twenty-Eighth Annual IEEE: IEEE; 2013:1812-1819.
217. Vandevoorde, G.; Puers, R. Wireless energy transfer for stand-alone systems: a comparison between low and high power applicability. Sensors and Actuators A: Physical 92(1):305-311; 2001.
218. Ko, W. H.; Liang, S. P.; Fung, C. D. Design of radio-frequency powered coils for implant instruments. Medical and Biological Engineering and Computing 15(6):634-640; 1977.
219. Jow, U.-M.; Ghovanloo, M. Design and optimization of printed spiral coils for efficient transcutaneous inductive power transmission. Biomedical Circuits and Systems, IEEE Transactions on 1(3):193-202; 2007.
220. Cameron, R. J. Advanced Filter Synthesis. Microwave Magazine, IEEE 12(6):42-61; 2011.
221. National Research Council Committee for the Update of the Guide for the, C.; Use of Laboratory, A. The National Academies Collection: Reports funded by National Institutes of Health. Guide for the Care and Use of Laboratory Animals. Washington (DC): National Academies Press (US) National Academy of Sciences; 2011.

VITA

VITA

Steven T. Lee
PhD Candidate
Weldon School of Biomedical Engineering
Purdue University
Medical Scientist Training Program
Indiana University School of Medicine, Purdue University

Education

Purdue University, West Lafayette, IN
Doctorate of Philosophy, Weldon School of Biomedical Engineering — May 2015

Indiana University School of Medicine (IUSM), Indianapolis, IN
Medical Degree — Pursuing

Purdue University, West Lafayette, IN — May 2008

Research Interest

Epilepsy affects 1% of the world's population and one-third of the patients are refractory to current anti-epileptic drugs. Electrical neuromodulation techniques—vagus nerve stimulation (VNS) and deep brain stimulation (DBS)—offer invasive, but promising paradigms to decrease seizure rates. In particular, closed-loop, responsive DBS at critical brain pathways can be an effective method to abolish seizures milliseconds after detection; however, the algorithms, electrode placement, and stimulation waveforms must be optimized to target specific populations of neurons. Optogenetics offers increasing spatial and molecular resolution to modulate and discover brain microcircuits by delivering opsins that are sensitive to specific wavelengths of light to selective neurons. The promise of optogenetics could be realized by "turning off" large populations of diseased neurons with optical stimulation shortly after detecting a seizure. While engineering of devices can improve their efficacies, the agglomeration of neurobiology, disease pathology, and physiological mechanisms of electrical and optical stimulation should drive the new generation of implantable devices. My interests lie in this vast and largely unexplored horizon. Specifically, I am interested in full system architectures of devices, low power control algorithms, and pairing traditional transistor based tools with molecular tools. Additionally, I am interested in cost-effective design solutions for resource poor populations.

Poster Presentations

1. Jefferys, J, Ashby-Lumsden, A, Lovick, T, Qing, K, **Lee, ST**, Irazoqui, PP. "Cardiac Consequences of Repeated Brief Seizures in Chronic Experimental Temporal Lobe Epilepsy. American Epilepsy Society Annual Meeting, Seattle, WA. December 5-9, 2014.

2. **Lee, ST**, Williams, PA, Qing, K, Lin, DT, John, SWM, Irazoqui, PP. "Custom ASICs with integrated Cortex-M0 MCU platform for closed-loop optical stimulation," American Epilepsy Society Annual Meeting, San Diego, CA. December 1-3, 2013.

3. **Lee, ST**, Williams, PA, Lin, DT, John, SWM, Irazoqui, PP. "Modular Cortex-M0 MCU Platform for Wireless, Controlled Deep Brain LED-Fiber Coupled Optical stimulation in Optogenetics," IEEE Engineering in Medicine & Biology Society Neural Engineering Conference, San Diego, CA. November 6 –8, 2013.

4. **Lee, ST**, Williams, PA, Lin, DT, John, SWM, Irazoqui, PP. "Towards a wireless, closed-loop optogenetic stimulator for seizure modulation," The 6th Annual International Workshop on Seizure Prediction, San Diego, CA. November 5 - 7, 2013.

5. **Lee, ST,** Krook-Magnuson, E, Abdel-Latief, O, Armstrong, C, Soltesz, I, Irazoqui, P P. "LED platform for wireless optical stimulation," American Epilepsy Society Annual Meeting, Baltimore, MD. December 2-6, 2011.

6. Mei, H, Jaroch, D, Ward, MP, Qing, K, **Lee, ST**, Albors, G, Irazoqui, PP. Magnetically Inserted Thin Flexible Microelectrodes. American Epilepsy Society Annual Meeting, Baltimore, MD. December 2-6, 2011.

7. **Lee, ST**, Zeng, B, Turkcan, A, Lawley, M. Using Capacity Adjustment to Reduce Patient No-shows. Quality and Systems Engineering Conference, The Mayo Clinic, Rochester, MN. September, 2008.

Conference Presentations

1. **Lee, ST**. "Towards a wireless, closed-loop optogenetic stimulator for seizure modulation," The 6th Annual International Workshop on Seizure Prediction, San Diego, CA. November 5 - 7, 2013.

Skill sets

- Altium Designer—printed circuit board design and testing
- Matlab programming
- Labview programming
- Embedded systems – firmware programming
- Bandpass filter radiofrequency powering
- Rodent surgery
- Electrical stimulation paradigms
- Optical stimulation paradigms

Research Experience

Center for Implantable Devices, Major advisor: Professor Pedro Irazoqui
Weldon School of Biomedical Engineering
Purdue University, West Lafayette, IN July 2010-May 2015

- Designed an implantable, wireless closed-loop electrical DBS research device
- Designed a skull mounted, deep brain optical stimulator for use in optogenetics
- Designed an omnidirectional RF wireless powering system for implantable devices
- Validated all designs *in vivo*

Department of Pharmacology, Professor John Jefferys' Lab
University of Oxford, Oxford, England
Visiting Researcher June 2014-Nov, 2014

- Implanted devices designed at Purdue to study SUDEP
- Performed acute study to identify DBS brain targets in epilepsy model

The Jackson Laboratory, Dr. Simon John's Lab
Bar Harbor, Maine
Visiting Researcher June 2012-Dec, 2012

- Performed chronic optical DBS study in transgenic mice
- Demonstrated optical dose-dependent conditioning in mice with wireless device

Weldon School of Biomedical Engineering
Purdue University, West Lafayette, IN Summer 2009
MSTP rotation with Dr. Chang Lu

- Investigated oil compounds to optimize the separation of cell culture medium into single droplets in a soft-lithography microfluidic device
- The device was intended to separate single cells into single droplets for techniques such as single cell electroporation

Weldon School of Biomedical Engineering
Purdue University, West Lafayette, IN Summer 2008
MSTP rotation with Dr. Mark Lawley

- Investigated scheduling algorithms to optimize the amount of extra clinic hours doctors should provide to maximize profits and minimize loss of revenue due to patient no-shows

Biomedical Engineering Summer Internship Program
National Institutes of Health Summer 2007

- 1 of 16 biomedical engineering students selected from the nation
- Used tandem mass spectrometers to identify and quantify the movement of proteins in response to vasopressin in rat renal cells
- Developed signal processing quality control of elution profiles developed from coupled high performance liquid chromatography and mass spectrometry

Indiana University School of Medicine, Indianapolis, IN Summer 2006
Research Intern in the Wells Center – Dr. Wade Clapp Laboratory

- Conducted several experiments *in vitro* to determine effects of multi-tyrosine receptor kinase inhibitor, Sutent, on $Nf1^{+/-}$ murine-mast cell function
- Cultured murine mast cells and fibroblasts
- Presented findings to fellow interns, medical students, physicians, and physician scientists

Weldon School of Biomedical Engineering
Purdue University, West Lafayette, IN
Dr. Eric Nauman Lab – Undergraduate researcher Jan 2005 – May 2007

- Investigated dielectric properties of adult bone marrow stem cells *in vitro*
- Wrote LabVIEW program for solenoid fixture
- Modeled applied direct currents and magnetic fields to cell culturing device
- Designed iron core Helmholtz solenoid fixture with flexibility to culture cells

Work Experience

Stryker Instruments, Kalamazoo, MI
Test Lab Summer Coop Summer 2005

- Performed over 20 tests
- Redesigned, built, and evaluated a specialized test fixture
- Designed a test fixture to assist measurements of tensile force
- Received excellent evaluation

Leadership Activities

Biomedical Engineering Graduate Student Association (BMEGSA) May 2011-May2014

Big 10 BME Graduate Student Speaker Exchange Program Coordinator

- Spearheaded the speaker exchange program between Big 10 universities

Engineering World Health (EWH) – Purdue Chapter August 2006 – May 2008

President

- Lead a group of students to establish the Purdue Chapter
- Organized interior and exterior renovations at the Trinity Nursing Center for Infant Health
- Received $1500 grant from the Office of Engagement to develop an education center for the Trinity Nursing Center for Infant Health
- Developed and led a Sunday mentoring program in which college students worked with elementary students to learn about engineering

International Experiences

Attended the Confucius Institute of Indianapolis Summer Camp
Guangzhou, China May 2009

- Attended Sun Yat-set University (SYSU) for language courses and participated in the medical program to experience traditional Chinese medicine and the Chinese health care system

Attended Pop-Wuj Language School in Xela, Guatemala May 2008

- Attended daily Spanish training sessions for several hours per day
- Worked in their low-cost medical clinic weekly
- Attended medical mission trips to sparse Mayan communities
- Assisted in building brick stoves external to the homes for Mayan communities

Attended China Maymester 2007, "Introduction to Intercultural Teamwork" May 2007

- Traveled to Shanghai, Ningbo, Beijing, and Harbin and interacted with Chinese undergraduate students. We also explored cultural differences and how partnerships between our countries would work.

Service and Outreach Activities

Biomedical Engineering Graduate Student Association July 2010-May 2015

- Volunteered at outreach activities at middle schools
- Purdue Spring Fest volunteer to discuss biomedical engineering to the public

Indiana University Student Outreach Clinic, Indianapolis, IN—medical-student run clinic for the underserved Jan 2009 – May 2010

- Volunteered every few weeks. Performed triage, patient medical and social histories, and patient physical exam
- Wrote protocols to assist patients in navigating the medical system in Indianapolis

Music Program at Riley's Children Hospital, Indianapolis, IN Jan 2009 – May 2010

- Formed a violin trio and a violin-guitar duet to perform music every week in the atrium
- Performed the "Day of Music" celebration over the 2009 winter holiday as the H1N1 emergency restricted outside musicians from visiting Riley Hospital
- Requested to perform for the Great Lake Region of the American Music Therapy Association in March, 2010

Timmy Foundation – Purdue Chapter Aug 2006 – May 2008

- Ecuador Mission Trip - served 1000 people in need over Spring Break
- Worked primarily in the pharmacy and triage
- Assisted in fundraising and donation collection events for Ecuador
- Served as Director of Community Engagement

Honors/Awards/Fellowships

Fearnot-Laufman-Greatbatch Award 2012

University Fellowship—Indiana University-Purdue University Indianapolis 2008-2009

- 1-year graduate fellowship that funded tuition, stipend, and an $800 travel allowance

GA Ross Award – Outstanding Graduating Man at Purdue University 2008

Phi Beta Kappa Honor Society 2008

Tau Beta Pi – Engineering Honor Society 2008

Phi Kappa Phi Honor Society 2007

PUBLICATIONS

PUBLICATIONS

1. **Lee ST,** Williams PA, Braine CE, Lin DT, John SWM, and Irazoqui, PP. A miniature, fiber-coupled, wireless, deep-brain optogenetic stimulator. *Trans. Neur. Sys. Rehab. Engineering.* (in press).

2. Nagaraj V, **Lee ST**, Krook-Magnuson E, Soltesz I, Benquet P, Irazoqui PP, Netoff T. *"Future of Seizure Prediction and Intervention: Closing the loop."* Journal of Clinical Neurophysiology. (in press)

3. **Lee ST***, Bercich RA*, Pederson D, Wang Z, Mei H, Qing K, Albors GA, Zhang H, Irazoqui PP. "*The Bionode: an Implantable Closed-Loop Research Platform."* 2015. Manuscript in preparation.

4. **Lee ST***, Mei H, Irazoqui PP. *"A Three-Axis Wireless Power Transfer System for Chronic Experiments."* 2015. Manuscript in preparation.